NORTHWESTERN UNIVERSITY

Fundamentals and Applications of Electrically-assisted Microrolling

A DISSERTATION

SUBMITTED TO THE GRADUATE SCHOOL
IN PARTIAL FULFILLMENT OF THE REQUIREMENTS

for the degree

DOCTOR OF PHILOSOPHY

Field of Mechanical Engineering

By

Man-Kwan Ng

EVANSTON, ILLINOIS

Aug 2017

ABSTRACT

In this presented study, rolling in micro scale level, termed as microrolling, has been advanced and extended its application to surface texturing and roll bonding. Meanwhile, continuous direct current (DC) is introduced to the processes to establish two new microrolling processes: the Electrically-assisted Roll Bonding (EARB) and the Electrically-assisted Microrolling-based Texturing (EAμRT). The continuous DC serves as a heating mean with a rapid effect over the conventional furnace heating method for material softening. The Joule heating effect, which is induced by electric current passage, softens the material resulting in flow stress reduction to ease material deformation. The effect of electric current on easing deformation is shown in both the EARB and EAμRT processes.

The EARB process is applied to the production of laminated metal composite (LMC) sheets, Al/Al and Al/Cu in this study. Beyond easing the deformation of the metal sheets for bonding, improvement is found in the bond strength. The local heating effect at the interface contributes to the overall bond strength enhancement of the bonded LMC. In order to further prove the existence of local heating at bonding interface and its influences on joining effect as well as to understand the behavior of Joule heating effect at the interface with the consideration of bonding surface topography, an analytical has been developed for local and macro interface temperatures prediction. Modeling results show that the local temperature can be so high to reach the recrystallization temperature and even the melting point of aluminum. Because the hot spots, i.e. local regions have higher temperatures than surroundings, is in a small area compared to the interface, their temperature is not necessarily to be captured by the macro interface temperature;

a hot spot with a few hundred degree Celsius can be found in an interface with a temperature below 100°C.

Besides roll bonding process enhancement, electric current is also utilized for surface microtexturing. EAμRT applied with 100A continuous DC is used for the texturing of micro grooves on aluminum (AA3003) and titanium (Ti-6Al-4V). By the result comparison between two materials, the significance of local heating in the process can be observed. Depending on the material, the significance of softening effect varies. Materials with higher electrical resistivities usually result in a more significant heating effect. With the application of electric current, deeper micro grooves are produced on both Al and Ti. To predict the micro groove depth in EAμRT, an analytical model with the consideration of roll wear has been developed. Additionally, investigation on the effect of surface texture on the surface hydrophobicity improvement is conducted as a case study of surface texture application.

ACKNOWLEDGEMENTS

The author would like to thank her research advisor, Professor Jian Cao, for the guidance and advice in her search during her Ph.D. study. Under the influence of Prof. Cao, she has a deeper insight into science and research. She has also learned the attitude of being a researcher from Prof. Cao. Thanks are also given to the author's Ph.D. committee members: Professor Kornel Ehmann of Northwestern University, Professor Robert Gao of Case Western Reserve University, and Dr. Ed Smith of Deringer-Ney Inc. They provided a lot of valuable and useful advice on the author's work. Special thanks are also given to Professor Zhaoyan Fan of Oregon State University, Professor Yoosuf Picard of Carnegie Mellon University, Dr. Marzyeh Moradi and Xiyue Zhou for their contribution to the author's research. Additionally, the author is also very thankful to Professor Kuniaki Dohda of Northwestern University for his advice on her search. Prof. Dohda is the one who initiates the author to pursue her dream on research and gives her a lot of helpful opinion on her career development.

Acknowledgment is also extended to Deringer-Ney Inc. and the Metal Industries Research and Development Center in Taiwan for the tool fabrication supports; Professor Jane Wang for providing the device for contact angle test, and; the Materials Characterization and Imaging Facility at Northwestern University for the microstructure measurement support.

The author also greatly appreciates the research fund support from the National Science Foundation. The presented research would not be conducted successfully with the support from the National Science Foundation.

Last but not least, the author also likes to say thank you to all her colleagues in the Advanced Manufacturing Process Laboratory at Northwestern University. Members in the laboratory

offered the author a lot of physical and spiritual supports so that her research could be conducted smoothly.

CONTENTS

LIST OF TABLES

LIST OF FIGURES

Chapter 1

Introduction

Electrically-assisted manufacturing (EAM) is a hybrid manufacturing process, which utilizing electric current to assist the manufacturing of metal components. The term of electrically-assisted forming (EAF) is used when an electric current is applied to a forming process. In this study, electric current is particularly applied in microrolling process for surface texturing – electrically-assisted microrolling-based texturing (EAμRT), and rolling bonding – Electrically-assisted roll bonding (EARB). Prior to a deeper discussion on EAμRT and EARB, a brief introduction and the state-of-the-art of the technologies are given in this chapter.

1.1 Background, Challenges and Objectives

Manufacturing is one of the important industrial sectors in the United States and even in the world. Bureau of Economic Analysis data shows that manufacturing gave the largest contribution to the gross output of United States in 2014, as shown in Figure 1.1[1]. According to the 2016 Global Manufacturing Competitiveness Index released by Council on Competitiveness and Deloitte, United States occupies the second place in the most competitive economy while China takes the first place[2]. It is also expected that the United States will become the most competitive manufacturing economy in the world by 2020[2]. There is no doubt that manufacturing plays an important role in the United States economy. In order to sustain the economy growth in the United States and remain in a beneficial position in the world economy, manufacturing

technologies should be advanced for cost reduction, production rate improvement, and competitive product quality.

Among the manufacturing sector, industries of automobile, aerospace, steel, and electronics contribute a large portion of the share in the manufacturing sector. The annual sale of vehicles is forecast to have 13% of increment from 2013 to 2018 [3]and commercial aerospace revenues are expected to grow faster than military through 2020[4]. Development of sheet metal forming technology and related manufacturing technique is desired in the future production of vehicles and airplanes to meet the growing market demands. Additionally, in order to improve the performance of vehicles and airplanes, such as a lighter body for fuel saving but stronger body against collisions, stronger but lighter materials are introduced. Titanium and its alloys are lighter but stronger metals used in automotive industry. They can be found in wheels, suspension springs, exhaust systems and pumper supports. The prominent performance of titanium, meanwhile, gives challenges in the production of its components because it is too strong to be formed effectively and efficiently. To overcome the challenges, the existing manufacturing method of hard materials, not limited to titanium, is necessary to be advanced. Furthermore, composite materials are promising in the replacement of traditional materials for a better mechanical property, a lighter weight, and the cost reduction by replacing part of the materials with the cheaper ones. Among various kinds of composite materials, laminated metal composites (LMCs) have promising applications in aerospace, automobile and defense industries due to their improved material properties over single layer sheet metals and alloys[5], lighter weight[5], improved corrosion resistance[5], higher fracture toughness[6] and better damping capacity[7]. However, the production of LMCs with an extended area, meanwhile with sufficiently

high resulting bond strength, is challenging. An effective manufacturing method for LMC production is pressingly desired.

For a better picture, some of the needs and challenges in manufacturing and their possible solutions are summarized in Table 1.1. In other to have a profound understanding of a process for its further improvement, its fundamental science behind, such as process mechanism and process characteristics, should be investigated and understood. Therefore, there are both scientific and application objectives are set in this study.

Application Objectives:

(1) To improve the production effectiveness of laminated metal composites by ***Electrically-assisted roll bonding (EARB)***

(2) To develop a low-cost and high-yield-rate process for surface texturing on hard materials, such as Titanium and its alloys by ***electrically-assisted microrolling-based textuirng (EAμRT)***

In overall, this study provides alternative solutions for: (1) hard material processing; (2) improvement in specific material properties by forming; and (3) production of laminated metal composites. Particularly for (2), the surface property is selected as a property to be improved because there is a raising interest in the production of multifunctional surfaces. Textures on surfaces provide promising effects on tribological improvements[8–11], drag reduction[12], tool wear reduction[10], cell attachment improvement on medical implants[13], biofuel production[14], and anti-bacterial growth[13]. For example, piston ring with textures on its surface reduces friction so that the fuel consumption can be improved[11,15]. Textures on surfaces find its values on different applications. However, there is a lack of both time- and cost-efficient method for the mass production of multifunctional surfaces. To impart or improve surface property of a material,

texturing by forming is utilizing in this study. Combining with the challenging brought by the hard material process, texturing on hard materials raises the difficulty in the process. In order to provide a solution to (1) and (2), an electrically-assisted microrolling-based texturing (EAμRT) is developed for surface texturing. For (3), because the need for laminated metal composites (LMCs) is rising, an effective method for a mass production of LMC with reinforced interface bond strength is desired. In order to meet the need, an electrically-assisted roll bonding (EARB) is developed in this study. For both EAμRT and EARB are developed based on a conventional forming method – Flat Rolling. Rolling is a common metal forming process in which rolls are used to roll, compress and form a workpiece into a desired shape in between two rotating rolls sandwiching the workpiece. Depending on the shape and form of the rolled part, rolling is classified into different types, such as flat rolling, roll forming, ring rolling, and thread rolling. Flat rolling is a common process to reduce the thickness of a metal sheet. It has the advantages of rolling sheets with flat and extended area and infinite length. Therefore, it is a promising high-yield process for flat sheet surface texturing and laminate metal composite production. For the rolling process either forming sheets with ultra-thin thicknesses or creating features in a micro-scaled level, a term of "microrolling" is particularly used to emphasize the scale level of the process.

Scientific Objective:

(1) To analyze the significance of local heating effect via the investigations of the EARB and EAμRT processes.

Localized heating effect may be observed in an electrically-assisted forming process. It is caused due to either a non-uniform current density, or non-uniform material properties or the combined effect of formers. To appropriately utilize electric current in the process for an improved

production in terms of material properties and quality, the effect and the significance of local heating should be understood. Additionally, the investigation on the local heating effect may also give an insight in the future study in electroplasticity. For example, it may raise a question: is the athermal effect actually attributed to the effect of micro/nano-scaled local heating, in which the local temperatures can be observed by a macro temperature. In most of the reported study, the process temperatures were measured by two conventional methods: (1) thermocouples, and (2) infrared camera. The former one can only give a point measurement and the later one only allows surface temperature measurement. Both methods cannot give the local thermal information. Unfortunately, there is no feasible device available to high spatial resolution temperature measurement over a large surface area inside the material core, instead of the surface, during electrically-assisted forming process. To achieve the scientific objective in this study, a 3D analytical transition interfacial Joule heating model is developed for a localized heating effect investigation.

Table 1.1 Summary of some of needs in manufacturing and their corresponding challenges and possible solutions

Need	Challenges	Possible Solution
1. Hard materials processing methods	• High forming/cutting load • Tool wears	• Processing parameter and condition adjustments
2. Materials with specific property improvement for better product performance	• Highly application-orientated • Geometry restriction to processing method and production time	• Post-processing after production • Processing process advancement
3. Composite material production method	• Long production time	• Processing process advancement
4. New materials with improved mechanical properties	• Long development time • High cost	• Utilization of modeling techniques for material design

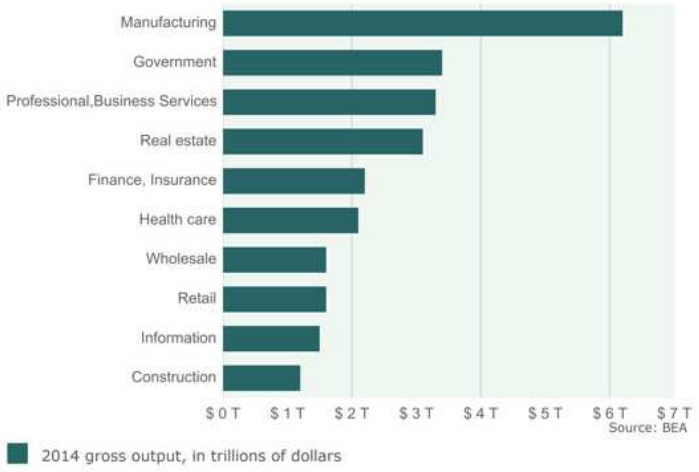

Figure 1.1 Gross output by sectors in 2014[1]

1.2 State-of-the-Art

1.2.1 Electroplasticity

Electroplasticity is a term used to define a phenomenon of material *plasticity* under the effect of *electricity* including direct current (DC), alternative current (AC), continuous current, and high/low intensive pulsed current. Its effects are generally classified into: the thermal effect and the athermal effect. The introduction of electricity to the forming process was first demonstrated by Thomson Electric Welding Company [16,17] and Dewey Corporation [16,17] in the 1890s. The heating caused by electric current passage was then termed as the Joule heating effect (or thermal effect) [18–21]. The athermal effect is referred to the effect dissociate with the heating effect and was first reported by Troitskii and Likhtman [22] of the previous Soviet Union on zinc single crystals. It was reported that there were interactions between the dislocations and the moving electrons during electric current passage in the metal, causing flow stress reduction as well as formability improvement [22]. Later, it was explained that the drift electrons initiated by electric current can exert an electron wind force on dislocations that encourages plastic flow [23]. These

discoveries initiated research on how electric loads influence material properties for various metallic systems on different topics. Conrad studied the influences of electric current on both metals and ceramics [24]. He reported that, in the case of metal, the thermal effect induced by electric current reduced the flow stress of metals. Perkins et al. also conducted similar investigation on various metals, such as aluminum, titanium, brass, and stainless steel. Experiments proved that besides flow stress reduction, different metals have different sensitivities toward current density [25]. Magargee et al. later performed an intensity analysis on the current density sensitivity on different metals and concluded that there are threshold current densities for different metals in order to have significant flow stress reductions [26]. The amount of threshold current density depends on the electric resistivity of metals. Metals with higher electric resistivity need higher threshold current densities. Furthermore, electron wind effect was believed to be a cause of flow stress reduction, which resulted from the momentum transfer when the electrons collide with atoms [19,24,27,28], the order of predicted threshold current density, J_0, to have a significant stress reduction is much higher than experimental data[19,24,27,28]; Therefore, the conclusion on the existence of athermal effect is still controversial.

Researchers also extended the research from using a continuous DC to a pulsed DC. Electropulsing is a term used to specifically describe the process applying pulsed current. Both the study conducted by Troitskii et al. and Conrad reported that pulsed current also gave an effect of flow stress reduction. These findings initiated a series of investigation on electropulsing at different deformation rates [29], current densities [25,30,31], current frequency and duration [32–34] in the case of electropulsing, etc. Summarizing those studies, it has been found that electropulsing promotes dislocation motion [35–39], improves deformability of alloys with unfavorable orientation relationships [40], gives better surface finishing [41], accelerates nucleation, atom diffusion and grain

growth [33,39,42–55], enhances recrystallization and grain refinement[36,44,47,49,52,53,55–62], induces damage healing [56,62,63], increases yield stress and ductility [27,37,39,47,51,54,57,64] as well improves corrosion resistance [48,65]. Although experiments reveal different phenomena caused by electric current, the mechanisms and driving forces for the "production" of these phenomena are still unclear. Although Troitskii and Likhtman [22] explained the athermal effect induced by electric current passage was attributed to the electron wind effect, Conrad gave an analysis result that the electron wind was insignificant to deformation [24]. Instead of the athermal effect, he believes the thermal effect was the dominated factor for the flow stress reduction [66]. Results of the isothermal tests conducted by Perkins et al. experimentally support the study of Conrad that the impact of the athermal effect was insignificant to initiate flow stress reduction[25]. Although studies from both Conrad and Perkin pointed that the thermal effect was the main contribution to the deformation enhancement, they did not deny the existence of the athermal effect. However, in the contrary, Magargee et al. had an opposite view on the existence of the athermal effect. He used forced air cooling to eliminate the thermal effect experimentally and found no noticeable drops in stress when continuous DC was applied[67]. Furthermore, the athermal effect was reported having an effect on dislocation behaviors[37,68]. Zhu et al. explained that electopulsing accelerated the movement of vacancies and dislocation annihilation resulting in formability improvement [37]. However, Kang et al. ran an in-situ electron microscopic observation on the dislocation of a single crystal copper at an electric current density of 100 A/mm^2 and observe no dislocation occurred during the process[69]. Moreover, the athermal effect was also used to explain the observation of microstructural changes [34,52,65,70–72], however, the effect can only noticeable in the pulsed current form and certain frequency range depending on the materials[34,70,73]. Researchers suggested that electropulsing strengthened the athermal effect while minimized the thermal effect

to maintain relatively low temperature[44,49,70,74–76]. The current densities of the investigations involved athermal effect varied between a few hundreds to a few thousands A/mm^2. Because the pulse durations were short, the measured temperatures were relative low, which usually in a range between 200°C and 700°C depending on the material, applied pulsed current density, and pulsed duration. However, there is a question: *Does the measured temperature is precise enough to conclude the thermal effect is removed completely?* Thermal couples and infrared (IR) cameras are usually used in the in-situ temperature measurement. However, there are limitations in these measurement methods: (1) they only give a macro temperature but do not have a high enough resolution to capture local heating temperature, and (2) they are only able to capture the surface temperature but not the core temperature. Heat generates once current passes the material. When the current density is high, such as a few hundreds A/mm^2, the local heating can be remarkable although heat may loss quickly. Therefore, a thermal effect is not eliminated even the pulse duration is short and the heating effect can be localized. Fan et al. studied the influence of grain size and grain boundaries in the electrically-assisted forming and observed local grain boundary melting. The boundary melting was attributed to the higher electrical resistivities at grain boundaries[77]. Both the study from Li et al. and Fe at al. proved that grain boundaries had higher electrical resistivities[78,79]. Li et al. conducted an electrically-assisted tensile test on Ti-6Al-4V alloy with different grain sizes and found the finer grain sizes resulting in higher Joule heating temperature[80]. Wang et al. also reported a similar result of higher temperature in finer grain sizes in AZ31 magnesium alloy[81]. These reported literature give an insight of the existence of local temperature. The measured temperatures in most study were the macro temperature, which missing local temperature information in the material. Furthermore, Wang et al. also experimentally revealed that there were differences between the workpiece core and surface

temperatures due to heat loss from the surface to air[81]. The rate of heat loss also depended on the geometry sizes of the workpieces. These studies give the evidence of the existences of local heating and workpiece surface-core temperature difference. Furthermore, Song et al., Zhou at. al and Yu et al. reported that micro-cracks were healed by electropulsing and they all explained the healing effect was attribute to the thermal compression due to the high pulse current density[62,82,83]. The high current density induced thermal expansion at the cracks. The thermal expansion produced a compressive force to close the cracks resulting in crack healing. The observation from these studies provided an additional piece of evidence in local heating existence.

The existence of athermal effect in electroplasticity is still skeptical because the local heating effect exists even the macro temperature is low. To reveal the truth, a question of "*Does a macro temperature reflect local temperature variations?*" is raised. The answer to this question will be given in Part 2 via the study in EARB. An analytical model based on an EARB process is developed in Chapter 3. After the affirmation of the independency of local heating temperature to the macro temperature, a second question is raised: "*Does the localized heating affect the forming process significantly?*" To find the answer, both experimental and analytical investigations via EAμRT are conducted in Part 3. An analytical model for micro channel depth prediction in EAμRT is developed in Chapter 5.

1.2.2 Hybrid Process: Electrically-assisted Manufacturing

Time is money. Speeding up production rate increases the chance of survival of a company in the competitive market. However, speed up of the production rate is always challenging because the processing/manufacturing time always is constrained by, for example, material properties, desired product quality, processing environment settings, and processing procedures. Examples

are given in Table 1.2. From these examples, additional processes are always required for the production, for example, heating for material softening prior to forming, surface finishing for smooth surface production, surface cleaning for coating. Besides additional processing time, preparations for the additional processes inevitably lengthen the total processing time. As a result, the overall production time is extended. One way to shorten the total production time is to perform multiple processes simultaneously. *Hybrid process* is a term used to describe a process that integrating two or more processes into a single step process. *Electrically-assisted manufacturing (EAM) laser-assisted manufacturing (LAM)* and *vibration-assisted manufacturing (VAM)* are examples of hybrid processes. LAM and VAM are applied in various processes which EAM (aka conductive-heat assisted) are commonly applied in the conventional forming process, as shown in Table 1.3[84]. EAM also found an application in the cutting process[85].

EAM and LAM usually assist the process with thermal effect[84]. They skip the pre-heating process and integrate it into the subsequent process into a single step process. For VAM, high frequency is applied to the process. The applied frequency can be either low as 1-10Hz [86] or high to reach ultrasonic level[85,87–91]. The VAM processes offer the benefits of surface quality and precision improvement[87,92], burr suppression[93,94], tool wear reduction[85,88,92], forming force reduction[92,94], acoustic softening and hardening[95] as well as feature geometry improvement[94]. These hybrid process strategies are applied on different processes for different purposes. The strategy of hybrid processes and examples are summarized in Table 1.4.

As mentioned in the previous section, the aim of this study is to provide alternative methods with an improved process performance for forming and texturing of hard metals as well as production laminated metal composite. With the consideration that thermal effect is an important factor for

the process improvement in the targeted processes and the less energy intensity to the laser-assisted process, the electrically-assisted strategy is selected for the process improvement.

Table 1.2 Type of factor limiting the production time and given examples.

Type of factor	Example
Material properties	• Glass should be heated up until melting before forming. • Metals with high yield strengths are required thermal softening for easier forming.
Desired product quality	• Surface finishing is required for the production of mirror surfaced parts. • Heat treatment is necessary for material hardening of a machined/ formed component. • Coating is required for the products with desired surface properties.
Processing environment settings	• Furnace needs to be preheated to a desired temperature. • Air should be evacuated completely for a vacuum processing environment.
Processing procedure	• Masking is usually required for chemical etching process. • Surface cleaning should be done before coating process.

Table 1.3 Hybrid processes and the combinations[84].

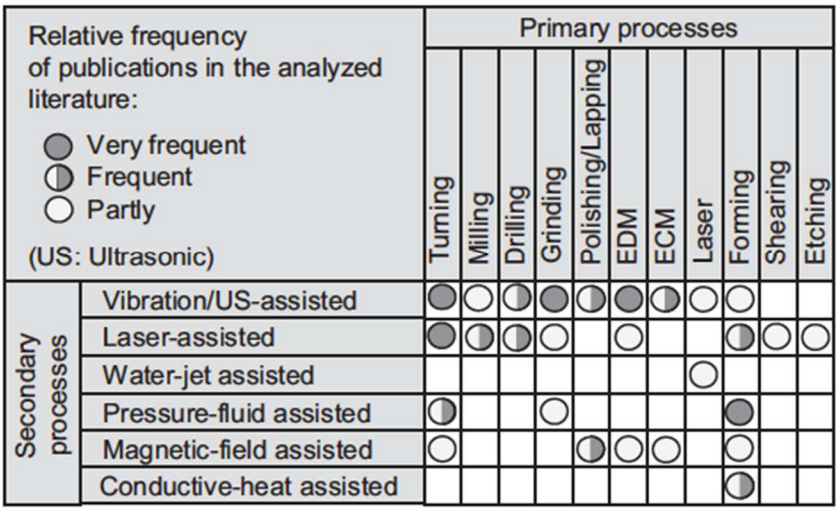

Table 1.4 Strategy of hybrid process and examples

Strategy of hybrid process	Applied process
Electrically-assisted	Forming Texturing Surface finishing Welding Cutting
Laser-assisted	Solid-state welding Machining
Vibration-assisted	Forming Machining grinding

In electrically-assisted Manufacturing (EAM), the advantages of rapid and localized heating effect of electric current make electric current an alternative heating source for metal warm or hot forming processes. Conventionally heating the workpieces in a furnace usually takes hours, depending on the workpiece size, to reach desired temperatures. However, the Joule heating of electric current can shorten the heating process to seconds while localizing the heating region, thus preventing unnecessary energy wastes. Consequently, electric current is introduced to the forming processes to perform warm and hot forming. Nguyen-Tran et.al gave a review on EAM and summarized the EAM process in Figure 1.2[96]. Since there are potential markets in textured surface and laminate metal composite productions, intensive studies of electric current effect in rolling and metal joining using roll bonding are conducted in this presented work. In this presented work, the scope of study focuses on the application of electric current, DC in this case, and its effects on the manufacturing production. The profound effects of electric current on material-wise are beyond the interest of this study.

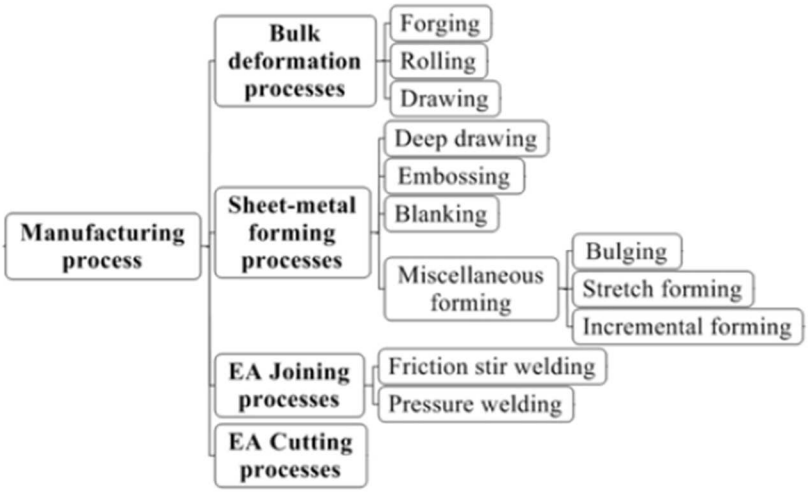

Figure 1.2 Summary of EAM process[96]

In this present study, microrolling enhanced by electric current – electrically-assisted rolling, is advanced for surface texturing and roll bonding. For conventional sheet/flat rolling, i.e. sole for sheet thickness reduction purpose, electric current was applied for easing material deformation. Continuous electric resistance heating was adapted in hot rolling for alloys with poor workability, as shown in Figure 1.3[97]. The fed-in stainless steel sheet was pre-heated by electric current just before entering the roll gap. It just took about 60 *s* to heat Ti-6V-4Al to 970 *K*. The temperature rise rate varies with materials. Besides heating the workpiece at the entrance of the rolling zone, the workpiece could also be heated across the rolling zone by connecting both ends at the entrance and exit of the rolling zone to the power supply, performing electrically-assisted rolling (EAR), as shown in Figure 1.4[98]. EAR was used to produce TiNi shape memory alloy (Figure 1.5) [53]. It showed a reduction in roll force and an improvement in thickness reduction. There was a maximum of 21.6% thickness reduction in a single pass and a total of 74% thickness reduction after seven passes. Furthermore, research was conducted to investigate the roll separating force and material structure of AZ31 Mg alloy under the effect of pulsed current [99]. In this study, no cooling was applied to the process and the Joule heating is in effect. The results

showed that the frequency of electric current did not exercise any influences on the roll separating force reduction in EA rolling. Pulsed currents were also utilized to roll TiNi alloy and Mg-9Al-1Zn alloy [50,64].

From the reported investigation in EAR, electric current was set flowing in the workpiece in the rolling direction. The workpieces were heated partially, which was usually a short distance between before entry and exit of the roll gap. The rapid heating effect induced by electric current passage enables the heating of materials to a few hundred degree Celsius within a few seconds and localizing the heating zone by controlling the current flow path. To maximize the localized heating effect, in this present study, electric current is set flowing from a roll to another via the workpiece as shown in Figure 1.6. This setting limits the heating only at the contact region between rolls and workpiece. As the heating depends on the current density, which is affected by the contact area, both the roll diameter and workpiece thickness reduction affect the heating effect.

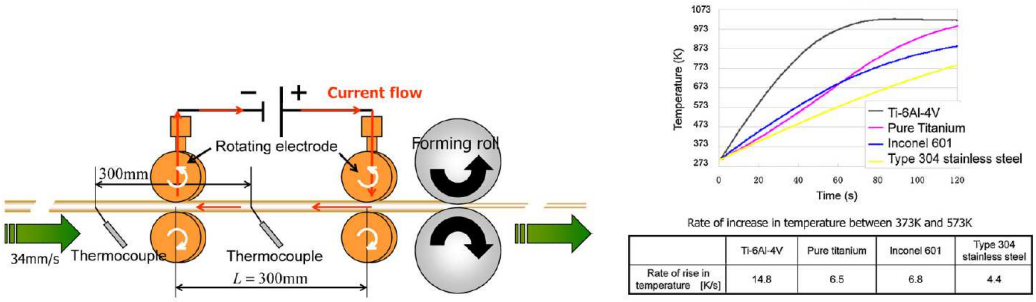

(a) (b)

Figure 1.3 (a) Experimental setup for continuous heating, (b) rate of increase in temperature[97].

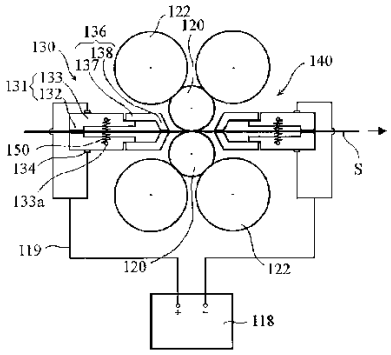

Figure 1.4 Schematic diagram of rolling device[98]

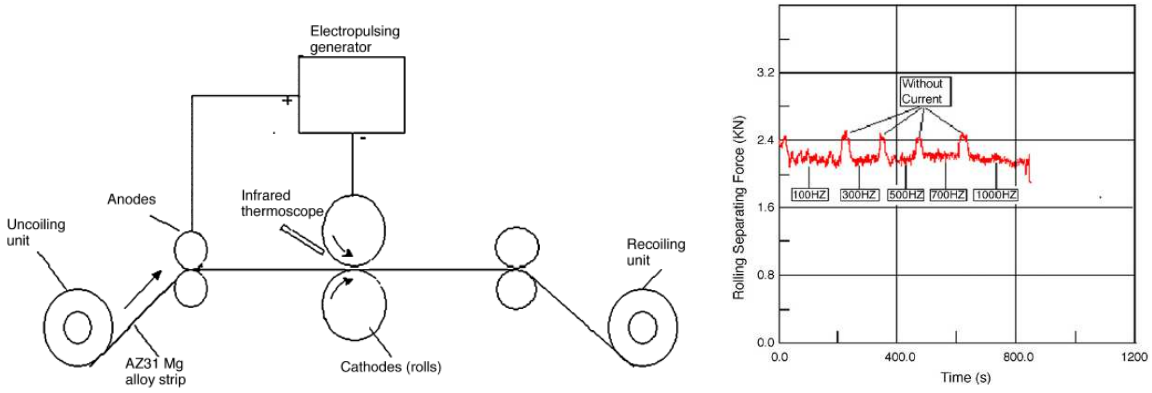

(a) (b)

Figure 1.5 (a) Schematic view of electroplastic rolling process, (a) The diagram of rolling separated force when the parameters of electropulsing varied[53]

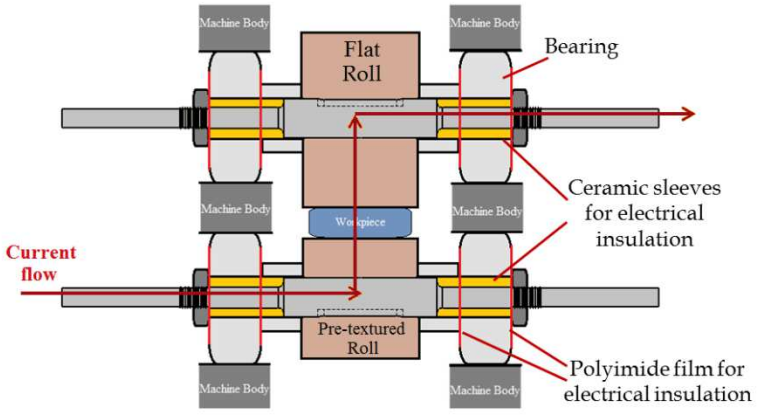

Figure 1.6 Illustration of current flow in this study

1.2.3 Microrolling for Joining Metal and Roll Bonding

Laminated metal composites (LMCs) have received considerable attention from aerospace, appliance, automobile, and defense industries because of their improved material properties over single layer sheet metals and alloys, including lower weight[5], improved corrosion resistance[5], higher fracture toughness[6], and better damping capacity[7]. One LMC application example is the replacement of copper alloy sheets with Al/Cu clad sheets. Al/Cu clad sheets have comparable electrical and thermal conductivities to copper alloys while providing about 40% and 60% reductions in weight and cost, respectively[128]. The application of Al/Cu composites has been extended to the production of armored cables, air cooling fins, TV set yoke coils and bus-bar conductor joints. Due to the strengthened properties, laminated metal bars have recently emerged in building construction[129]. As the application of LMCs increases for different industries, there is an increasing demand for developing more cost- and time-effective techniques for LMC production.

To manufacture LMCs, metal layers need to be joined. This can be accomplished by adhesive bonding, mechanical fastening, fusion welding, or joining by deformation. In the production of LMCs, permanently joined large surface areas are required, rendering fusion welding and mechanical fastening unsuitable for joining metal layers. Adhesive bonding can be applied over a large area; however, bond strength is limited by the properties of the adhesive. The sensitivity of adhesives to surface finish[130] and the environment, such as temperature and humidity, further affects their performance, resulting in variation of the bond strength. Joining by material deformation can transcend the limitations of the above joining techniques as reviewed by Mori et al[131].

Joining by deformation can generally be classified into two categories: mechanical and metallurgical. The difference is that mechanical joining by deformation, for instance, self-pierce riveting and mechanical clinching, deforms the components to be joined to create "obstacles" or "interlocks" that facilitate joining. In metallurgical joining by deformation, joining occurs by generating new metallic bonds at the metal layer interfaces through deformation. This technique is basically subdivided into four groups: cold welding, friction welding, friction stir welding, and resistance welding[131]. In friction- and resistance-based joining, relative motion at the interface between the metal surfaces is applied. The relative motion removes surface material generating a new surface. The applied compression force causes large deformations so that new metal surfaces at the interface are compressed and merged by forming new metallic bonds. During the process, high temperature is generated at the interface. Cold welding also involves new surface generation and metallic bond formation. However, no material is removed from the surfaces. It is a joining process purely caused by plastic deformation via different forming processes. Depending on the forming process selected, cold welding can be applied over large joining area.

Conventional Roll bonding (CRB), as one of the cold welding processes, enables joining over large areas and is an effective process for LMC production. It joins metal by large plastic deformation, i.e., high thickness reduction. Depending on the materials to be joined, the threshold thickness reduction varies. For example, at least 40% and 60% of thickness reductions are required for copper to aluminum and iron, respectively[132]. Moreover, the thickness reduction percentage also plays an important role in bond strength improvement. Larger thickness reduction leads to strong bond strength[132].

In order to enhance bond strength of the produced LMCs and reduce the rolling force due to the high percentage of thickness reduction, single-pass CRB has been advanced by either repeating

the process multiple times or carrying out the process at elevated temperatures. The stronger bond strength of LMCs can be achieved by roll bonding metal stacks with a larger thickness reduction percentage. However, the high rolling force required for high thickness reduction percentage always raises challenges to the production process, such as high machine load, roll wears. In order to achieve a larger thickness reduction for stronger bond strength of the LMCs, accumulative roll bonding (ARB) is applied for the production[133–137]. ARB is a multiple pass roll bonding process. Metal stacks are rolled repeatedly until reaching the desired thickness reduction percentage. Because ARB is a kind of severe plastic deformation process, it also brings a grain refinement and microstructure alternation functions to the deformed materials additional to bonding purpose [133,138–141]. Besides ARB, CRB process is carried out at an elevated temperature for roll force reduction and bond strength reinforcement. One of the advantages brought by the elevated temperature is material softening. Depending on the temperature, the process can be classified into warm and hot forming process. It is a warm forming process if the process temperature is below the recrystallization temperature of the workpiece materials, otherwise, it is a hot forming process. Applying elevated temperature for material softening in a process, which is usually done by placing workpiece in a furnace, is a very common measure adopted in the industry in order to reduce metal deformation force. Other than material softening, CRB at elevated temperature also helps in bond strength improvement and threshold thickness reduction for bonding[142–144]. The duration of heating also impacts the bond strength[143].

Knowing that carrying roll bonding at elevated temperature has the advantages of rolling force reduction for high thickness reduction and bond strength improvement, this study aims in advanced CRB with an unconventional heating measure in order to accelerate the process by shortening the pre-heating time of workpieces. In this study, electric current is introduced to the

CRB and advanced to process to be an electrically-assisted roll bonding (EARB) process. Compared to conventional heating with a furnace, electric current induced Joule heating effect is localized and rapid. Heating can be controlled and concentrated at the regions where the current passes. The regions can be heated up to few hundreds degree Celsius within a few seconds, depending on the current density. In this study, EARB the aluminum and copper ultra-thin sheets are bonded by EARB. Investigation on effects of Joule heating will be conducted and examined experimentally. Furthermore, in order to understand the Joule heating behavior at the bonded sheets interface, an analytical model is developed for the prediction of local and macro interface temperatures basing on real being-bonded sheet topography.

1.2.4 Surface Texturing

Depending on the application needs, textures are fabricated on different materials, such as metals, ceramics, glass, and polymers. For texturing of a metal surface, it can be accessible by difference texturing techniques, such as chemical engraving[100], photochemical machining[101,102], focused ion beam milling[103], laser ablation[104–108], micro abrasive machining[109,110], embossing[111–114], microforming[115,116], etching[117–119], micromachining[120,121], casting[122], grinding[123], and chemical/electrochemical deposition[124,125]. Different texturing methods result in different texture size. The ranges of texture size of some texturing methods are shown in Figure 1.7. Depending on the texture size requirement and workpiece geometry, different texturing techniques are applied. For example, grinding was used for the texturing on a wheel[123]. In this presented work, the forming method is used in surface texturing. Forming has the merit of suitable for mass production in a relatively shorter time and less energy intensive than most of the texturing method. It is especially suitable for the mass production of textured surfaces.

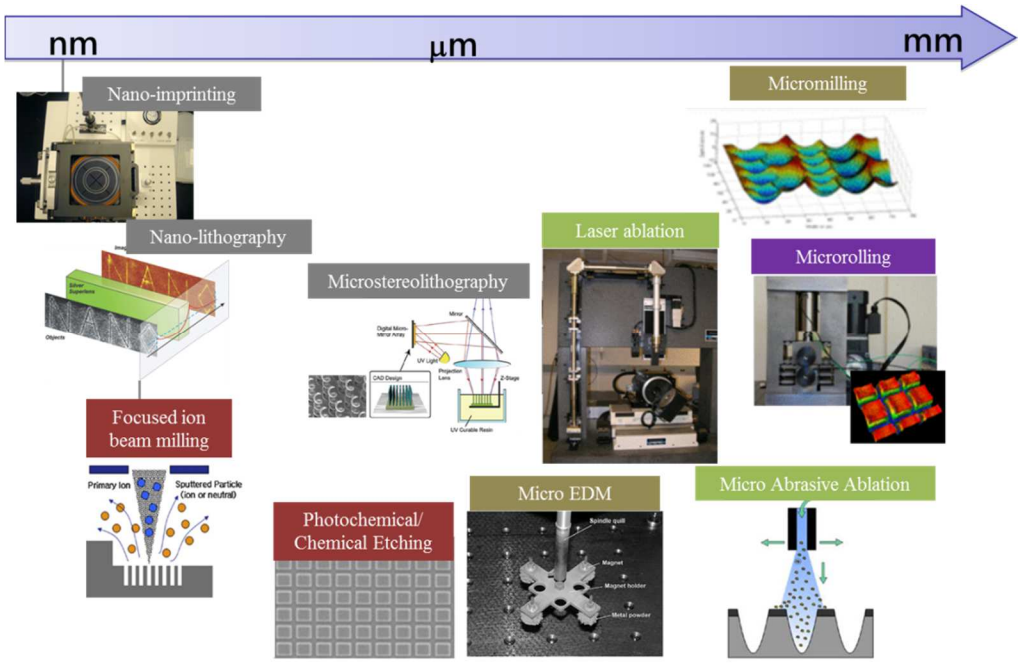

Figure 1.7 Texture size ranges of some texturing process

Owing to the potentials for mass production, different forming-based texturing techniques have emerged in the productions of micro surface textures on either cylindrical surfaces or planar surfaces. Ike and Plancak created circular cavities with a diameter of 175μm, depth of 28μm and wall angle of approximately 70° on 2mm A1050-H24 sheets by coining (Figure1.8) [126]. In other reported study, microgrooves, another texture geometry, was textured on SUS303 and A6061 shafts surface, instead of a planar surface, by rolling the shaft between two flat pre-textured dies (Figure1.9) [116]. Depending on the textures on dies, either spline patterned or dimple patterned textures could be imprinted. A maximum texture depth of 5 µm was produced, in which textures were uniformly formed on the shaft. Research on texturing on ultra-thin metal foil was also conducted. Micro channels were transferred to 3μm thick copper foil and 2.5μm thick AISI 304 stainless steel foil by pressing (Figure1.10) [127]. Channels with a width of 12 μm and depth of 9 μm were produced on copper foil. Due to the high strength of 304 stainless steel, only a

maximum channel depth of 2.3 μm and 3.5 μm with a corresponding width of 12μm and 15 μm, respectively, were produced. Besides the channel depth, the thinning effect of the foil was also studied in the reported study. The thinning behavior was related to the channel dimension and channel spacing. The images of the product can be seen in Figure 1.11.

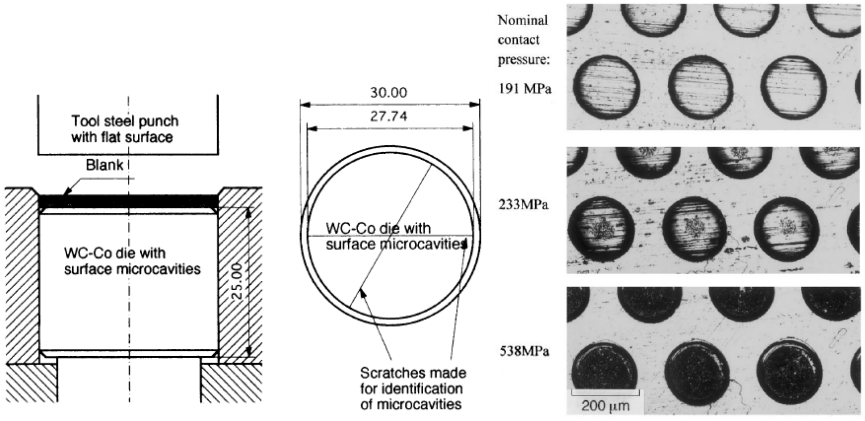

(a) (b)

Figure 1.8 (a) Setup of coining tools in a die set (*mm*), (b) top view of the formed surface microprojections[126]

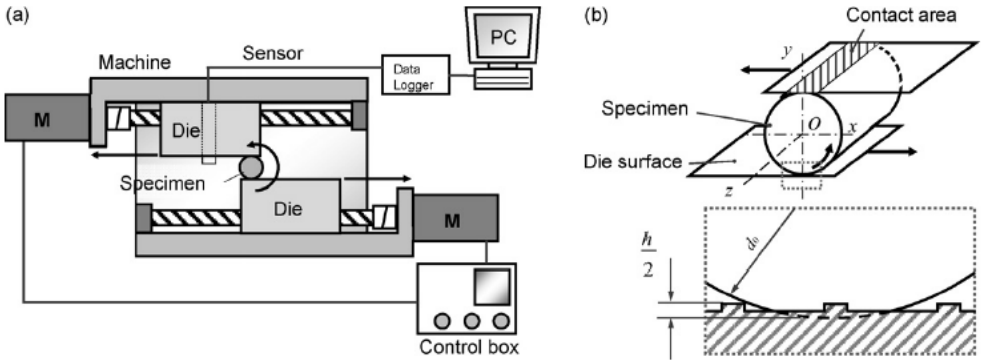

Figure 1.9 Experimental apparatus for form rolling microgrooves on a cylindrical specimen[116]

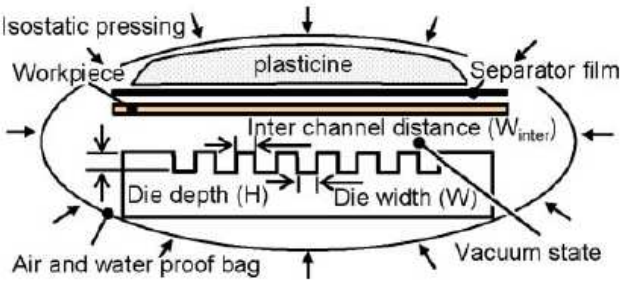

Figure 1.10 Schematic of micro channel forming process[127]

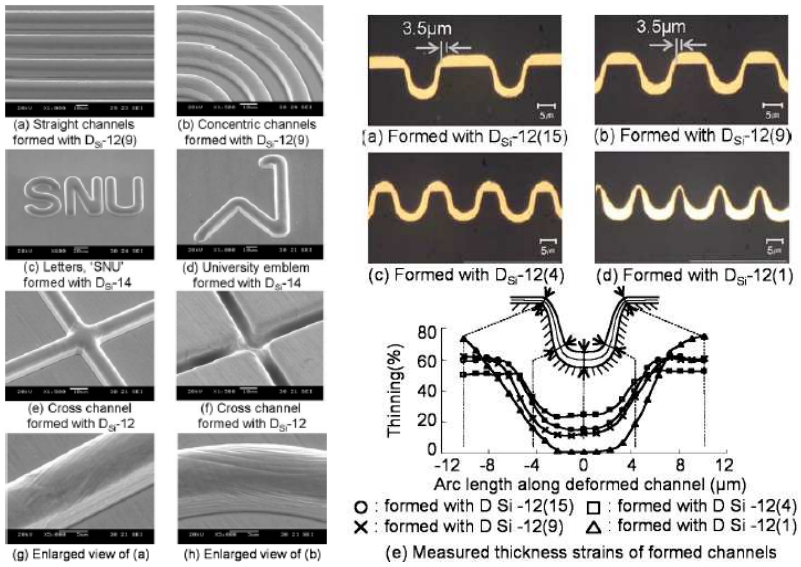

Figure 1.11 Produced texture images: (Left) Channels made on copper foil with Si wafer die, (Right) Sections and thickness strains of channels made on copper foil with Si wafer die[127]

In this study, microrolling, a kind of forming process particularly for micro-scale level, is utilized for texturing. (Micro)rolling has a good reputation of high production rate and is suitable for mass production. Integrating texturing to rolling enables the texturing on sheet material with infinite length during thinning process, which is the merit of rolling-based texturing that outperforming other forming-based texturing processes. Microrolling-based texturing allows

thinning and texturing to be performed at the same time so that the overall process time can be shortened. The texture geometry is transferred from the rolls to workpiece surfaces. Microrolling-based texturing and electrically-assisted forming-based texturing is going to be reviewed in Chapter 4, in which investigations are conducted particularly on electrically-assisted microrolling-based texturing.

Chapter 2

Electrically-assisted Rolling Bonding

Roll bonding is a solid-state welding process joining sheet metals by plastic deformation during a rolling process. In this chapter, a desktop microrolling system is introduced. Then, the conventional roll bonding process is advanced by electric current, which acts as a heating mean, and the advanced process is termed as "electrically-assisted roll bonding (EARB)". EARB was applied for the production of laminated metal composites. In this study, Al/Al and Al/Cu composite sheets were produced. Comparisons on the rolling force and peeling force were made between the conventional roll bonding process and electrically-assisted roll bonding process.

2.1 Literature Review

Electrically-assisted roll bonding (EARB) is an advanced process based on roll bonding. Conventional roll bonding (CRB) is a kind of solid-state welding performed by the conventional rolling process. It metallurgically joins metals, usually in sheet form, by large plastic deformation and new metallic bond formation of the subjected metals. Layers of sheet metals, their surfaces are usually cleaned to remove contaminants as well as brushed to remove oxide and produce micro cracks, are fed into a roll gap of a rolling machine. When they pass through the roll gap, they are compressed by rolls. The metal underneath the contact surface (virgin metal) is squeezed to break the micro cracks on the surface and extruded from the cracks to the surface. The extruded virgin metal joins and bonds with contacting virgin metal by forming new

metallic bonds. This mechanism is called "Film Theory" [145]. Roll bonding has the advantages over wet weldings, such as arc welding and spot welding, that enables the joining of metals over a large surface area and adhesive bonding of insensitivity of surface finish [130] and environments, such as humidity and temperature. Together with the merits brought by rolling, for example, continuous production of infinite product length, roll bonding is a promising process for joining metals with a large joining area. This metal joining method has its importance particularly in the production of laminate metal composite (LMC) – a metallic composite material, and its application has been widely spread into different industries, such as aerospace, automobile defense, appliance, and construction. Industries have been attracted by the advantage of improved material properties over a single layer of sheet metals brought by LMC, including, lower weight [5,128], better corrosion resistance [5,146], better damping capacity [7], improved fracture toughness [6] and enhanced fatigue live [147]. Replacing part of expensive materials with a less expensive one to reduce overall material costs [128]. The benefits of LMCs has motivated the investigation of LMCs produced by roll bonding [143,148–158] as well as the process [159–163].

There are multiple factors affecting the roll bonding process and its products in terms of bond strength and microstructure. Bay et al. joined different sheet metal pairs by roll bonding and studied the factors affecting bond strength[145]. Bambach et al[164] presented a numerical framework to simulate the bonding process. It was reported that bond strength depended on the amount of surface expansion or thickness reduction. A threshold value of surface expansion shall be exceeded to achieve successful cold welding of different metal pairs[132]. Besides thickness reduction, bonding force and bond quality are determined by the rolling conditions, e.g., rolling speed and temperature, shape factor in rolling as well as surface conditions.

Conventionally rolling temperature is increased by elevating the workpiece temperature in a furnace. As compared to furnace heating, heating by an electric current is rapid with a localized heating effect. Electrically-assisted microrolling was used to heat and soften metals for enhancing surface texturing[165]. Additionally, an annealing process is often applied after roll bonding to further enhance the bond quality, in which the annealing temperature is one key factor[166]. Quadir et al.[167]and Movahedi et al.[168] studied Al/Al and Al/Zn bonds, respectively. Both studies have shown that increasing the annealing temperature increases bond strength and decreases the required threshold in thickness reduction for bonding.

Xu et al. conducted electrically-assisted solid-state pressure welding to increase the bond strength at the same thickness reduction level as without current applied[169]. However, the reported pressure welding is a kind of static state bonding and differs from electrically-assisted roll bonding in this study, which is in a dynamic state. Leveraging the advantages of the electric current in material softening and in-process annealing, EARB is conducted and its capability and bonding mechanisms are investigated. Additionally, the bond strength of roll bonded LMCs is experimentally evaluated.

2.2 Microrolling System

2.2.1 Microrolling Mill

The conventional roll bonding (RB) and electrically-assisted roll bonding (EARB) was performed with a desktop microrolling mill (DμRM), as shown in Figure 2.1. The mill body is a one-body structure consisted of two main parts: a main body and flexural bearing housings (FBHs) with flexural hinges. The entire mill body was cut directly from a high strength steel block by wire EDM. The flexural hinges connect the flexural bearing housings to the main

frame, and allow vertical displacements of the housings in micrometer range for roll gap adjustment. The one-body structure provides high structural stiffness and compactness to the machine. There are two pairs of FBHs: a pair of upper housings and a pair of lower housings. They accommodate both ends of the upper and lower roll shafts with tapered roller bearings for high radial loads during the rolling process.

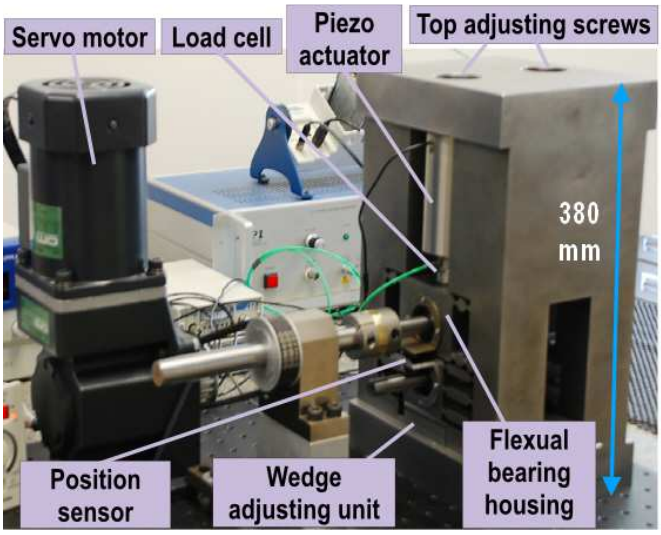

Figure 2.1 A desktop microrolling mill

The DμRM is equipped with a pair of piezo actuators, capacitive displacement sensors and loadcells at the two ends of the roll shaft. The piezo actuators are utilized for assisting roll gap adjustment and roll movement constraint. There is a wedge adjusting unit under the lower FBHs, as shown in Figure 2.2, for coarse roll gap adjustment. It is adjusted by the screw at the back of the mill. The screw pushes “Block A” inwards and the displacement of “Block A” levels up “Block B”, resulting in an upward movement of lower FBHs. Then, the upper FBHs are pushed by a pair of piezo actuators placed separately on their tops for fine adjustment. The piezo actuator has a travel range of 80 μm and a resolution of 0.8 nm. It offers a maximum blocking

force of 30 kN so that it is able to resist the upward movement of FBHs caused by the reaction force exerted by a workpiece during the rolling process. A pair of capacitive displacement sensors is attached separately on the upper FBHs at each roll shaft ends. The sensor has a measurement range and a resolution of ± 2 mm and 10 nm, respectively. By knowing the displacements of the upper and lower FBHs moving toward each other, a set roll gap size can be calculated with a known initial roll gap which is 400 μm without any adjustments. Note that it is assumed that the displacements of both upper and lower rolls are consistent with their corresponding FBHs. The displacement sensor also enables a real-time roll gap monitoring during the process. A pair of loadcells, with 5 kN/μm rigidity and 30 kN load capacity, are installed and sandwiched between the piezo actuator and upper FBH top at both ends of the upper roll shafts separately for real-time rolling force measurement.

For electrically-assisted microrolling, electric current was set flowing from one roll to the other via the workpiece sandwiched between them, as shown in Figure 1.6. One end of each shaft was connected to the electrode of a high current power supply with a slipring. The slipring is capable to the current size up to 250A and it was cooled by forced air cooling during the process to ensure its function delivery. The high current power supply is able to deliver continuous DC up to 300A.

Table 2.1 Dimensions of roll textures

Texture section	Left	Middle	Right
Tooth top width (μm)	60	15	50
Tooth height (μm)	50	30	110
Spacing (μm)	100	80	200

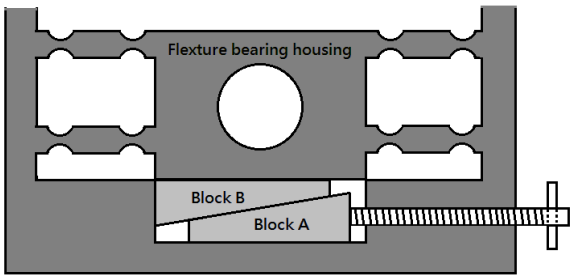

Figure 2.2 A wedge unit for coarse roll gap adjustment

2.2.2 Embedded Rolling Pressure Sensing

In the rolling force measurement, force measurement device installation locations influence the degree of accuracy subjected to the forming scale and process. For the DμRM used in this study, force sensors are installed on the tops of roll shaft bearing housings. The shortcoming is that the sensor readings may consist of the force against machine component stiffness resulting in obtaining a reading larger than the actual value. Overcoming the deficiency and limitation of conventional force sensors, an embedded capacitive pressure sensor was used for in-situ spatial rolling pressure measurement. The embedded capacitive pressure sensor is developed under the collaboration with Prof. Robert X. Gao of the University of Connecticut[170]. A sensing rod with electrodes, as illustrated in Figure 2.3, is inserted in a roll 1 or 2 mm underneath its surface along the roll axial direction. During rolling, elastic deformation of roll surface due to the reaction force exerted by the workpiece closes the gap between the internal wall of the sensing and the electrodes on the sensing rod. The changes in gap distance vary the capacitance of the capacitive sensor. With a finite element model which developed prior to sensor installation, corresponding pressures can be calculated according to the roll deformation. The embedded sensor can be applied in the rolling process either with or without electric current introduction.

The installation location of the sensor enables the measurement taking place right at the rolling zone and eliminates the errors caused by the stiffness of the machine and components. Instead of a general rolling force, the embedded sensor gives a local rolling pressure along the workpiece width direction. There are two generations of the embedded sensor. The sensors and their circuit boards are shown in Figure 2.4. The 1st generation sensor has a wider copper electrode width of 7mm while it is 2 mm in the 2nd generation. There are 4 electrodes on the sensing rod in both generations; however, the sensing coverage lengths are 30 mm and 10 mm in the 1st and 2nd generations, respectively. In other words, the 2nd generation sensor has a higher resolution than the 1st generation. For the 1st generation sensor, pressure measurement covers the entire three texture-sections of the pre-textured roll was measured while measurement was only taken at the middle section with the 2nd generation sensor. Additionally, the 2nd generation sensor is equipped with wireless data transmission which greatly benefits the ease of sensor installation and eliminates the risk of data wires being twisted during the process. The embedded capacitive pressure sensors were installed to the DμRM for μRT and EAμRT. Note that only one sensor was installed for tests. Separated tests were conducted with different sensor generations. The embedded sensing system was used in the microrolling-based texturing.

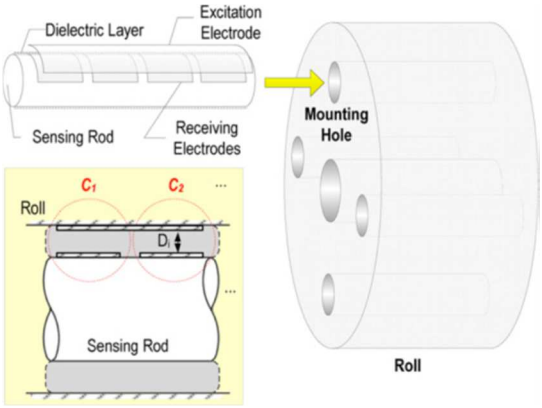

Figure 2.3 The schematic of an embedded capacitive pressure sensor

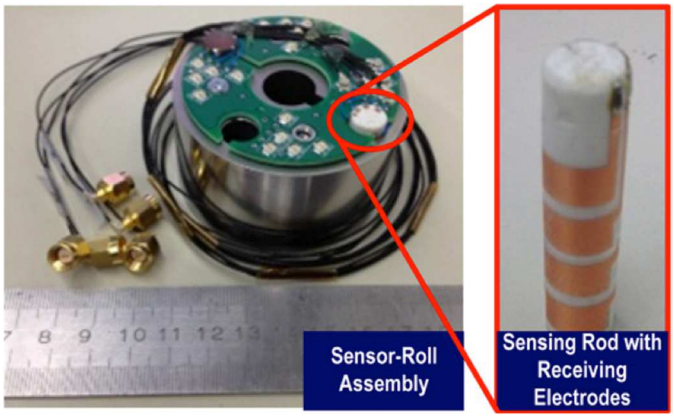

(a)

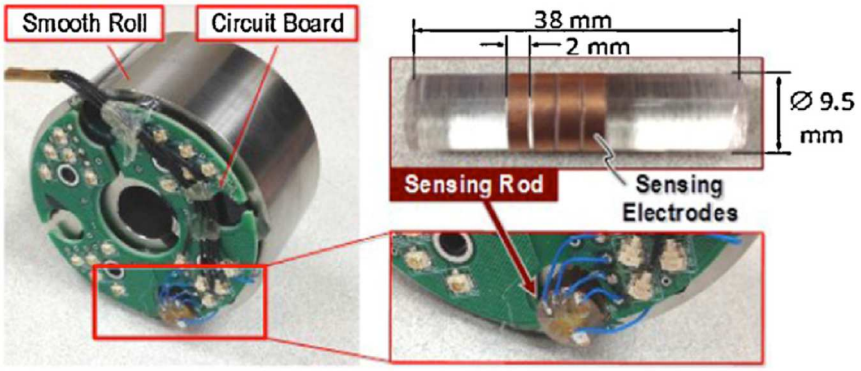

(a)

Figure 2.4 The embedded capacitive pressure sensors and their circuit boards attached to smooth roll: (a) 1st generation, and (b) 2nd generation

2.3 Roll Bonding of Al/Al and Al/Cu Metal Laminates

In this section, Al/Al and Al/Cu metal laminates were produced by conventional roll bonding (CRB) and electrically-assisted roll bonding (EARB). Both the rolling force and the strength of laminated produced by CRB and EARB were studied.

2.3.1 Roll Bonding Process Mechanism: The Film Theory

The bonding mechanism in conventional roll bonding can be explained by the Film Theory[145]. For a successful joining of metals, there are prerequisite conditions for the bonding surfaces. To allow efficient bonding, the surfaces should be cleaned and brushed. Cleaning procedure aims to

remove any grease and contaminants on the surface and brushing is done for the removal or thinning of the oxide layer and surface micro cracks generation. Note that complete removal of the oxide layer is not necessary. The film theory explained that, under compression during roll bonding, the metal underneath a surface is compressed to break the micro-cracks on the surface. The broken micro-cracks act as exits allowing metal underneath to be extruded out onto the surface. The metal underneath is termed as fresh metal or virgin metal. Once the extruded virgin metal from a surface meets those from the opposite surface, a metallic bond is formed between meeting virgin metals, and therefore, metals join. Because extrusion of virgin metal from underneath surfaces is required for successful bonding, a high percentage of thickness reduction is required. Depending on the metal pair, the threshold thickness reduction for bonding varies[132]. Larger thickness reduction creates a stronger bond. Additionally, process conditions, such as temperature and rolling speed, also exercise influence on the bond strength[142–144].

2.3.2 Electrically-assisted Roll Bonding

Roll bonding joins metals by plastic deformation. A threshold thickness reduction should be met in order to join metals and it varies with different metal pairs. Further increase of thickness reduction helps in bond strength improvement. Unfortunately, the threshold thickness reduction is usually high. For example, at least 40% of reduction is required to bond aluminum to aluminum[132]. It is generally challenging to deform metal sheets with a high thickness reduction, especially for hard metals. Therefore, a strategy easing metal deformation is desired to roll bond metals and further improve the bond strength. Softening metals by heating is an accessible way to ease deformation. Instead of the time-consuming furnace heating, Joule heating induced by electric current can be utilized to perform metal heating. As mentioned in Chapter 1, Joule heating has an advantage of rapid localized heating enabling metal flow stress reduction.

Advancement on roll bonding process with electric current to an electrically-assisted roll bonding (EARB) process allows metal softening easing deformation for reaching to, or even above, the threshold reduction for bonding. Furthermore, besides improving bond strength by larger thickness reduction, elevating the interface temperature also offers a bond strengthening effect [142–144]. The Joule heating in EARB extends its application to bond strength improvement other than deformation assistant.

2.3.3 Experimental Setup for Roll Bonding and Peeling Test

A microrolling system described in Section 2.2 was used for both the CRB and EARB processes; however, the pre-textured roll was replaced by a smooth roll. The smooth roll has a diameter of 27.58 mm and was made of D2 tool steel and heat treated to HCR 60 hardness. For EARB, electrical current was set flowing from one roll crossing the workpiece to the other roll. Current sizes of 50 A and 150 A were applied in separated cases in EARB.

Aluminum alloy sheets, i.e. alloys 1100, 1145 and 1235, were roll bonded with either the same alloy or 110 copper alloy sheets. All sheets have a thickness of 127 μm and 5 mm width. In order to prevent the narrow Al and Cu sheets from slippage during the rolling process, sheets were sandwiched between a folded stainless steel sheet as illustrated in Figure 4.1. The stainless steel "clip" also increased the total stack thickness to achieve high thickness reduction in a limited minimum roll gap size. Since the folded stainless steel clip has a stronger material mechanical property that both Al and Cu sheets, the compressive force during rolling was transmitted to the Al and Cu sheet resulting in deformation and roll bond of Al and Cu sheets. Prior to the roll bonding process, the Al and Cu surfaces being bonded were cleaned with acetone to remove greases, followed immediately by manual wire brushing for 20 to 30 seconds. During wire brushing, the brush was moved back and forth along the length direction of the sheet, i.e., the

rolling direction. For the convenience in the clamping procedure in the subsequent peeling test, approximately 10 mm length at the end of the sheets were not brushed so that these regions would not be bonded and left "tails" for clamping in the peeling test. The tails are the regions uncovered by the folded stainless steel sheet in Figure 2.5. The wire brushing procedure removed the oxide on the surface and created micro-cracks benefiting underneath virgin metal extrusion during the roll bonding process. The effect of brushing time on the brushed aluminum surface roughness is shown in Figure 2.6. Three tests were conducted for each time case and 4 random locations on the brushed sheet were taken for roughness measurement with a 3D optical surface profiler, Zygo NewView^{TM} 7000 Series White Light Interferometer (WLI). The results ensure that the brushing time (20 to 30 seconds) in the bond surface preparation did not lead to a significant impact on the surface quality between roll bonding tests generally. After cleaning and brushing the surfaces, the treated surfaces were faced and overlapped on each other, then sandwiched with a folded stainless steel sheet. The metal stacks were sent to perform CRB and EARB immediately. At the beginning of each roll bonding process, rolls were reset to their initial positions.

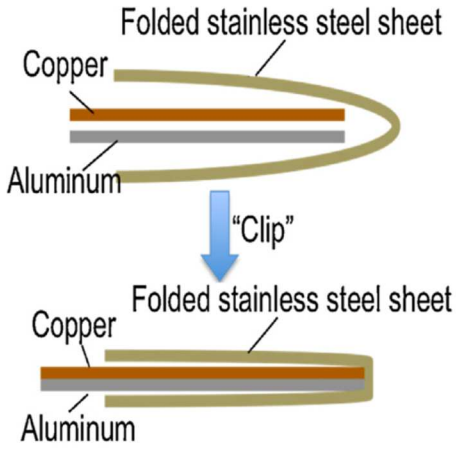

Figure 2.5 Workpiece layout for the roll bonding process

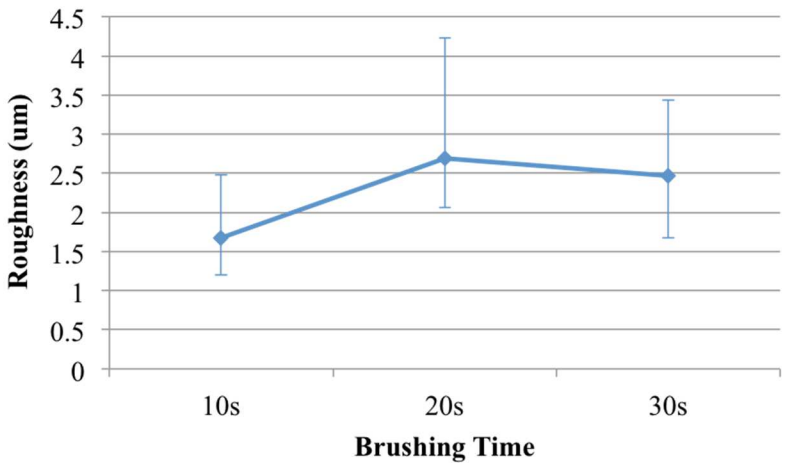

Figure 2.6 The effect of brushing time on brushed aluminum surface roughness

After roll bonding, bonded laminated composite sheets were undertaken with peeling tests for bond strength evaluations. The peeling tests were performed by a micro uniaxial tensile machine (SEMTest 1824 LM, MTI Instruments/Fullam Inc.) as shown in Figure 2.7. The machine was equipped with a loadcell with a 100N capacity and a resolution of 0.01N. A motor was used to drive the motion of a clamp and the total peeling length was measured by a linear displacement transducer with a resolution of 1 μm. The tails of the bonded specimen were clamped in the machine as illustrated in Figure 2.8. The clamped tails were then pulled apart at a pulling rate of 0.11 mm/s and the peeling force was recorded during the entire peeling test.

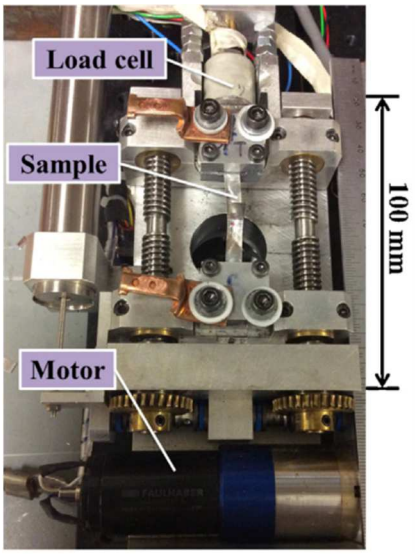

Figure 2.7 A micro uniaxial tensile machine loaded with a roll bonded sheet

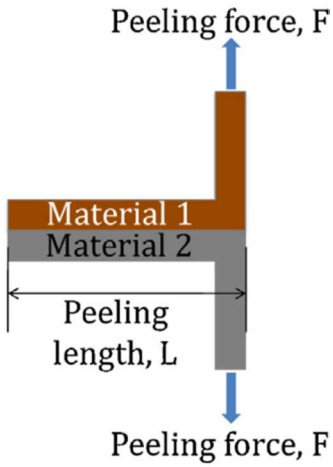

Figure 2.8 An illustration of peeling test

2.3.4 Results and Discussion

To ensure metals were bonded successfully, the interfaces of roll bonded metal laminates were observed with an optical microscope. Figure 2.9 shows the optical microscopic images of interface cross-sections of laminates bonded under different process parameters. The absence of

voids evidences that the metal stacks were joined successfully. There are no visible interfaces in Al/Al laminates because Al sheets were bonded together.

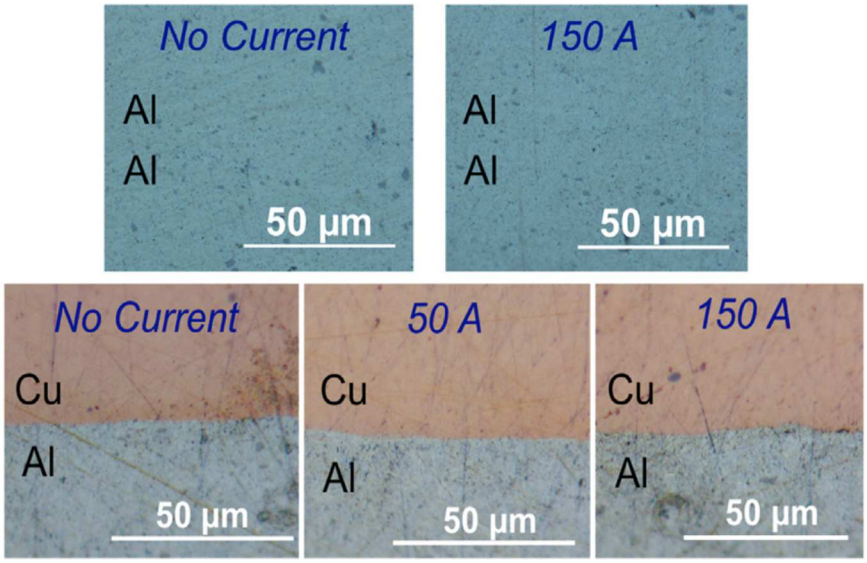

Figure 2.9 Optical microscopic image of bonded laminates

During the roll bonding process, rolling forces were measured by load cells. Two load cells were placed on two ends of the roll shaft (See Section 2.2 for machine details). Roll force was obtained by summation of both load cell measurements. The average roll force in the production of laminates in the entire process is shown in Figure 2.10. In the EARB, current sizes of 50A and 150A were applied. In the production of Al/Al in Figure 2.10(a), rolling force increases with thickness reduction percentage in both CRB and EARB because of the increase of flow stress with larger strain. Figure 2.11 shows the true strain-stress curve of the tested aluminum from ASM data. In EARB, it is expected that the Joule heating effect softens materials resulting in rolling force reduction. However, the amount of softening depends on the significance of Joule heating determined by the current size. Note that heat also is generated on the stainless steel

"clip". Due to the high electrical resistivity of the stainless steel, the heating effect in the clip is more prominent. The heating of the workpiece is the combined effect of self-generated Joule heating and heat conduction from the clip. In EARB of Al/Al, there are no significant rolling force reductions in 50A EARB for 50% and 60% thickness reductions. This is because the applied current size did not generate significant Joule heating for material softening. Assuming no heat loss, it can be seen in Figure 2.12(b) that the generated Joule heating temperature (Eqn. 2.9) is less than 50°C when a current of 50A is applied, resulting in no observation of lower rolling force. However, when the current is high enough, such as 150A, the current densities in both 50% and 60% reduction are much higher than that in 50A case as shown in Figure 2.12(a). As a result, a remarkable temperature in the range of 300°C - 350°C is generated according to Figure 2.12(b). Note that the melting point of aluminum is 660°C. Similar results are found in Al/Cu laminate production in Figure 2.10(b). Additionally, because the roll-workpiece contact geometry is non-linear with respect to the thickness reduction, as expressed in Eqn. 2.1, it leads to the non-linearity of calculated current density and Joule heating temperature rise against thickness reduction percentage.

$$A = wl = wR\cos^{-1}\left(1 - \frac{\Delta h}{R}\right) \qquad \text{(Eqn. 2.1)}$$

where w is the workpiece width, l is the arc length of the roll contacting to the workpiece. R and Δh are the roll radius and workpiece thickness reduction, respectively.

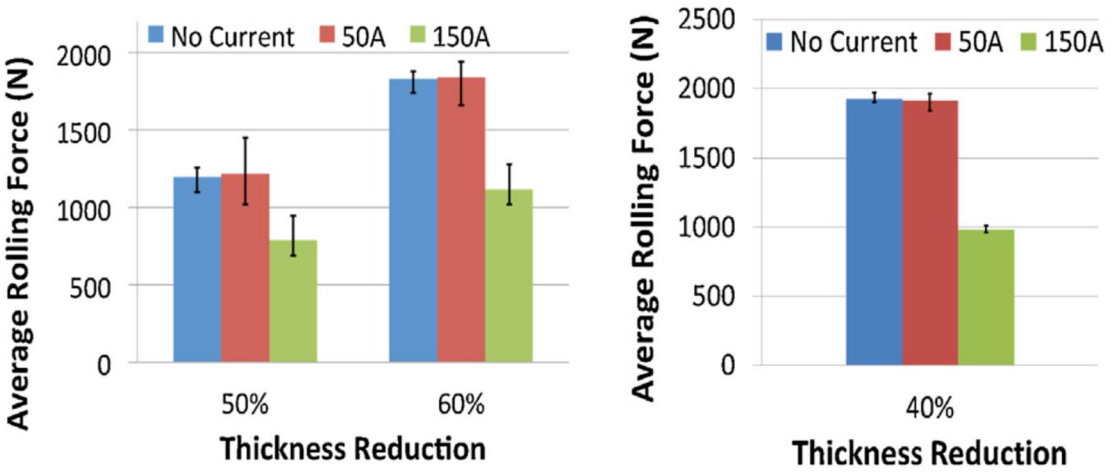

(a) Al/Al laminate (b) Al/Cu laminate

Figure 2.10 Rolling force in laminate production by roll bonding

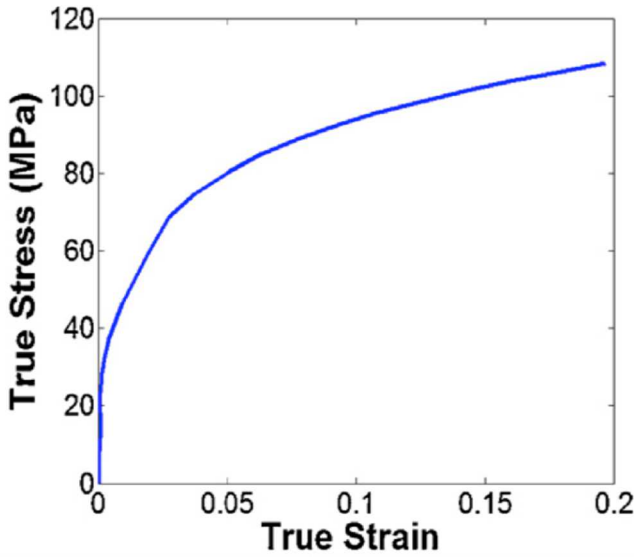

Figure 2.11 True strain-stress curve of tested aluminum

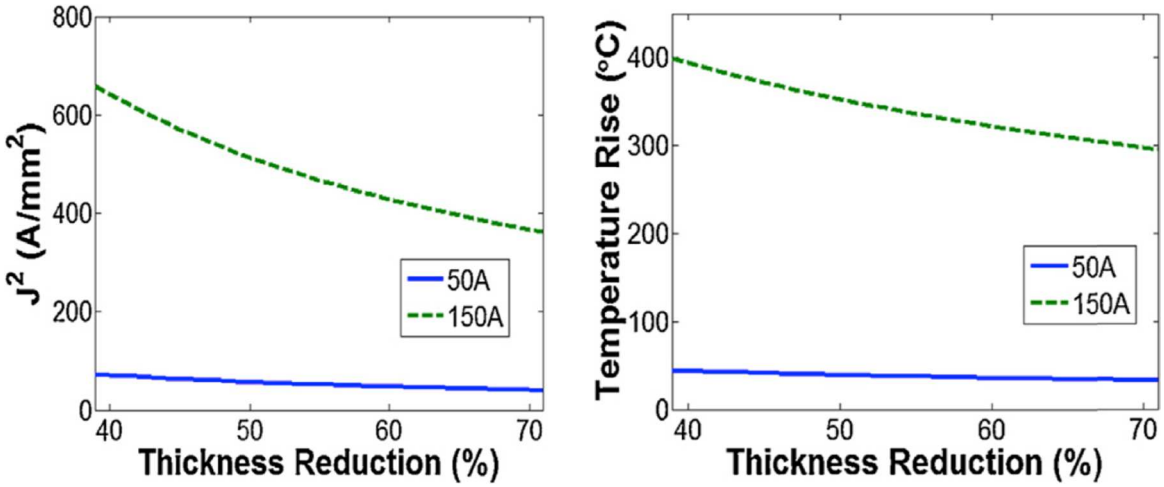

(a) (b)

Figure 2.12 (a) Estimation of current density and (b) calculated adiabatic Joule heating temperature rise on Al/Al laminate in different thickness reductions.

After the production of metal laminates, the laminates were peeled for bond strength evaluation. The average peeling force results are shown in Figure 2.13. A larger peeling force reflects more strongly in the bonding. From Figure 2.13(a), the peeling force increases in a larger thickness reduction percentage. The stronger bond in larger thickness reduction can be explained by the film theory established by Bay[145]. According to the theory, fresh metal, also called virgin metal, underneath the metal surface is extruded to the metal surface due to compression by rolls. The compressed virgin metal breaks the surface oxide layer and surface cracks, which is generated by brushing, and exits to the surface. The extruded virgin metal joins other virgin metal by forming metallic bonds. When thickness reduction increases, more virgin metal is extruded and forms more metallic bonds. Therefore, the increased bond strength results in the need for a larger peeling force required. Furthermore, the Joule heating effect induced by electric current passage also demonstrated in the bond strength improvement and the improvement depends on the applied current size. Generally, bond strength increases with increasing applied current size

within the interested current size range, except in the case of Al/Al laminate with 60% thickness reduction. The effects of Joule heating can be clearly observed in the result of Al/Al laminate with 50% reduction in Figure 2.13(a). Although the Al/Cu laminate results in Figure 2.13(b) do not give a distinguished difference in the peeling force and current size relationship as Al/Al 50% given in Figure 2.13(a), it still reveals the bond strength improvement brought by the electric current. Furthermore, by comparing the Al/Al laminate results between CRB and 50A EARB at 50% reduction, an interesting finding, that Joule heating may not be the only effect brought by the application of electric current, is unveiled. According to Figure 2.12, the Joule heating effect in 50A EARB is trivial and causes the demotion of EARB to a CRB process resulting in comparable rolling forces between these two cases, as shown in Figure 2.10(a). It is expected that both CRB and 50A EARB produced laminates should have a similar peeling force in the peeling test. However, interestingly, the feeling force of laminate produced by 50A EARB is higher than that of CRB produced Al/Al laminate in Figure 2.13(a). Similar results are also found in Al/Cu laminates (Figs, 2.10(b) and 2.13(b)). This proves that the electric current enhances bond formation in addition to Joule heating effect. Besides the thermal Joule heating effect, the additional reasons causing bond strengthen under electric load are still under investigation.

In the case of 60% Al/Al laminate, it is understandable that the 50A EARB was demoted to CRB due to negligible heating and led to similar rolling forces to that of CRB in Figure 2.10(a). As explained previously, there may be an unknown athermal effect causing bond strength under electric load. Therefore, bond strength improvement in 50A EARB at 60% thickness reduction is expectedly higher than CRB at the same reduction. However, it is abnormally high and even exceeds the value given in 150A EARB case according to Figure 2.13(a). The abnormally high

peeling force can be explained by the delayed rolling speed due to high thickness reduction. Rolling speed is one of the determining factors for bond strength. Slower rolling speed helps in the production of a stronger bond. The experimental measurement showed that the rolling speed was slowed down from 0.7 mm/s to 0.6 mm/s at 60% reduction without notable heating and softening. Besides, the slower process lengthens the process time under the electric load effect, both thermal and athermal effects, for bond improvement. Consequently, both the slower rolling speed and lengthened process time cause unexpectedly high peeling force in 50A EARB of Al/Al laminate with 60% thickness reduction.

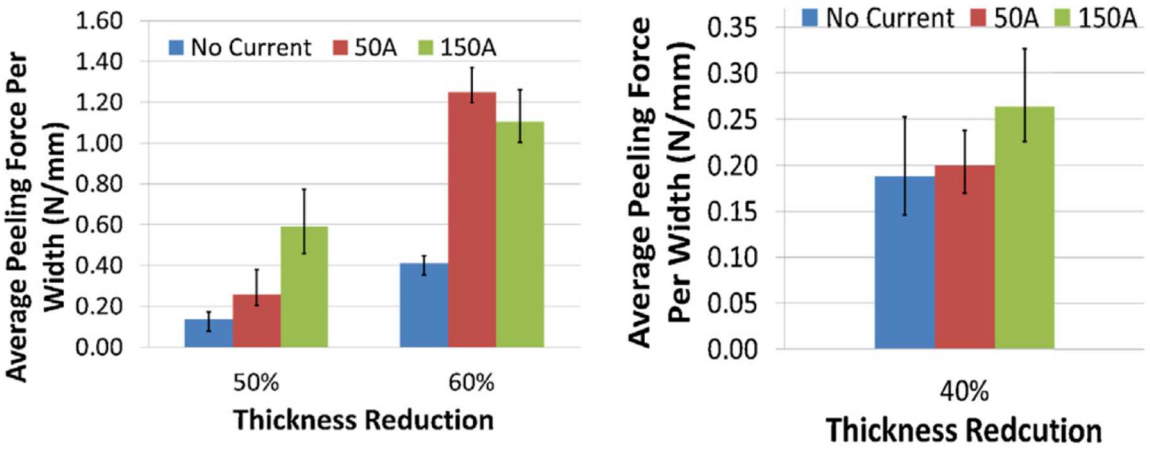

(a) Al/Al laminate (b) Al/Cu laminate

Figure 2.13 Peeling force in laminate production by roll bonding

2.4 Conclusion

Electrically-assisted roll bonding (EARB) has been utilized for the production of composite metal laminates. Ultra-thin Al and Cu sheets with a thickness of 0.127 μm were roll bonded for Al/Al and Al/Cu laminates. Compared to conventional roll bonding (CRB), EARB has a thermal effect, known as the Joule heating, for material softening. The degree of softening depends on the applied current size. Sufficient current size produces significant Joule heating for material

softening resulting in roll force reduction. The elevated temperature at the laminate interface due to Joule heating also improves the bond strength leading to larger peeling force required to separate laminates apart. Furthermore, improvement in bond strength was also found in the EARB with insufficiently high current size, i.e., trivial Joule heating effect. The results give the insight that athermal effect brought by the electric current may also have an impact on bond formation enhancement. Further investigation on the athermal effect of electric current on EARB is required in the future study.

Chapter 3

Interface Temperature Modeling in Electrically-assisted Roll Bonding

Electrically-assisted roll bonding (EARB) has been successfully demonstrated in the production of Al/Al and Al/Cu composite laminates in Chapter 2. To further investigate the role of Joule heating in EARB, an analytical model is developed in this chapter. Firstly, it reviews the previous experimental results and microstructure observation on EARB bonded sheets conducted by our team. Then, it describes the modeling methodology and construction followed by modeling results. Next, investigation and evaluation are conducted on the results. This chapter develops a model for local interface temperature simulation and provides an insight into the interface temperature immediately before EARB. The model is not only limited to the application to EARB, it can also be applied to any interface temperature calculations involving Joule heating induced by electric current passage across an interface of two approaching surfaces.

3.1 Literature Review

EARB was developed in order to advance the conventional roll bonding process for improving laminate metal composite (LMC) bond strength [171]. EARB enhances roll bonding with elevated processing temperature by the introduction of electrical current to the process. Electric current is applied and flowing across a metal interface. The Joule heating effect caused by the current

passage brings both a metal softening effect for deformation force reduction and an elevated temperature for bond strength improvement [171]. To further understand the bonding mechanism in EARB as well as the contribution of Joule heating in the process, knowledge of interface temperature is critical. However, there are challenges to interface temperature measurement: (1) the deformation zone and the joining zone are enclosed so that non-contact temperature measurement methods are restricted; (2) insertion of measurement probes into the interface interrupts the material joining process; (3) electric current potentially causes damages or interference on the measurement device; and (4) local interface temperature is too difficult to be captured by measurement devices. Some types of sensors can be embedded into a roll for pressure measurement in rolling [165,172] and temperature measurement in cutting [173]. However, the embedded type thermal sensors can only provide indirect temperature measurement through heat transfer from the sheet to roll but not a direct measurement at the interface.

Microstructure observation can be an alternative approach to uncover temperature history during the EARB process, however, it is not sufficient to understand how Joule heating affects the process. It does not forecast how the surface topography of the bonding surface varies the Joule heating effect. Therefore, in order to have an insight into both the macro and local interface temperature, which are currently restricted by physical measurement, modeling is an essential and promising tool to simulate the effect as well as to estimate the interface temperature. However, there is no literature reporting interface Joule heating temperature prediction with the consideration of interface topography. This chapter develops a modeling method with the consideration of topography of contacting/joining surfaces to simulate the Joule heating effect in the interface and predict both the macro and local interface.

In this chapter, first, a review of the previous experimental results and microstructure observation of EARB bonded sheets conducted by our team will be given. Then, modeling methodology and construction are described and followed by modeling results. Investigation and evaluation will be presented on the results. Next, additional sets of simulations will be performed and compared in the "Discussions" section for a further model and result evaluations. In this chapter, a model for local interface temperature simulation will be developed and an insight on the interface temperature immediately before EARB will be provided. The model is not only limited to the application on EARB, it can also be applied to any interface temperature calculations involving Joule heating induced by electric current passage across an interface of two approaching surfaces.

3.2 Experimental Result Review and Microstructure Observation

Commercially pure aluminum and copper sheets with thicknesses of 127 μm were roll bonded by EARB and then peeled for bond strength evaluations in Chapter 2. Results show that EARB reduced rolling force, meanwhile, improved bond strength. Moreover, non-uniform peeling force profiles were found in EARB bonded sheets, as shown in Figure 3.1. It is suspected that the non-uniform peeling force profile was due to localized heating enhancing bonding regionally. Furthermore, microstructures of bonded sheet interfaces were observed. Nanocrystallized microstructures were found in some regions, as shown in Figure 3.2. Those nanostructures were good indications that regions had temperatures higher than the crystallization temperature, or even, the melting point. Note that the microstructure was obtained from a single pass EARB instead of an accumulative roll bonding (ARB) – a multi-pass roll bonding process, which may produce nanostructures in the bonded sheets due to severe plastic deformation [137,151,174–176].

Additionally, the localized interface is also suspected to be high enough to weld the material so that the bond is so strong that fracture occurs instead of peeling during the peeling test, as shown in Figure 3.3. In order to evaluate the possibility of high local interface temperature occurring in EARB and causing regional melting or recrystallization of materials, a model is developed to estimate both macro and local interface temperatures.

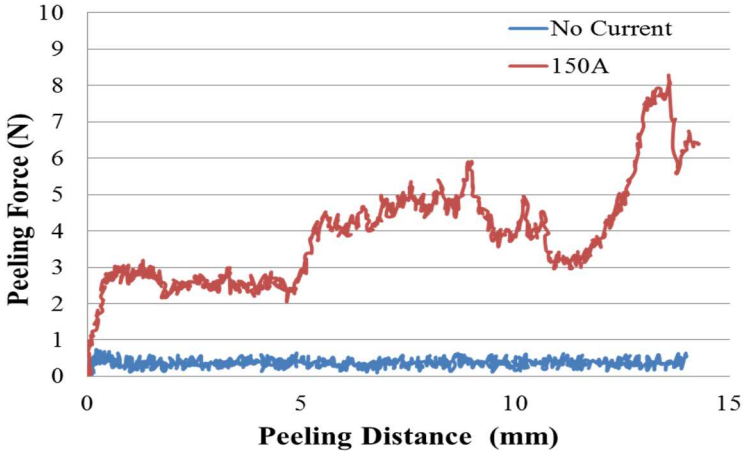

Figure 3.1 Peeling force profiles of Al/Al sheets bonded by conventional roll bonding and electrically-assisted roll bonding with 150A DC current

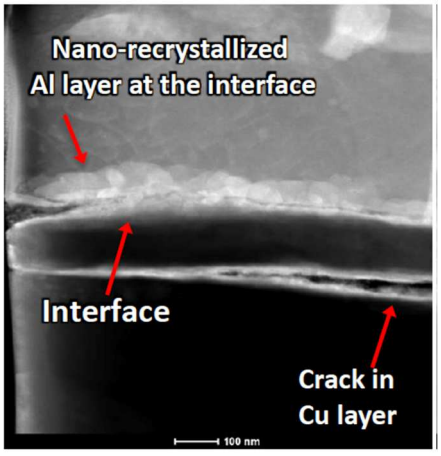

Figure 3.2 TEM image of an Al/Cu sheet interface

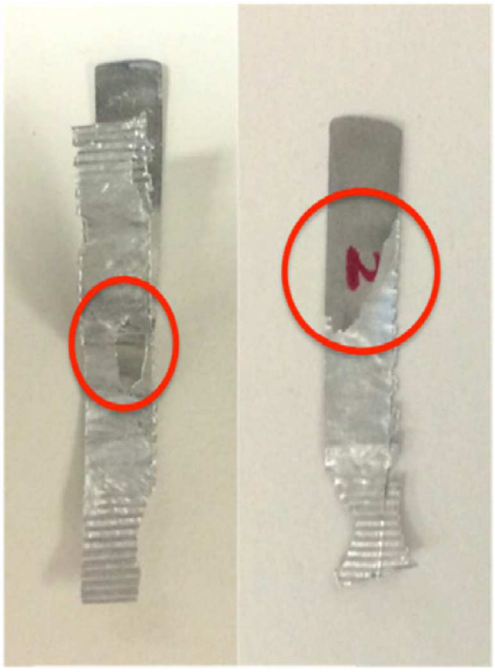

Fig 3.3 Examples of fractured electrically-assisted roll bonded samples during peeling tests

.

3.3 Modeling Concept and Methodology

In this section, the model construction concept and methodology is introduced and explained. The definition of some terms in the model is given and explained as well.

Assumptions for the Physical Effects of the Model

1. The effects of oxide layers on metal surfaces are neglected.
2. There is no deformation of the contact surfaces. Therefore, the topography of the surfaces does not change during the entire simulation.
3. Electric charges flow across the contact boundary of two surfaces. No charges are flowing along the boundary.
4. The Joule heating effect on the roll is negligible.
5. Energy loss is assumed solely due to thermal conduction to the roll body

1. Interface Layer Definition

In this study, the Joule heating effect on EARB of Al/Cu is investigated. The interface layer is defined based on the surface topography. Figure 3.4 illustrates the contact of two surfaces with their individual surface topography. The thickness of the interface layer is the vertical distance between the lowest points on each surface. Please note that these two points are not necessarily coincident vertically. The thickness of the interface is used to determine the local material properties.

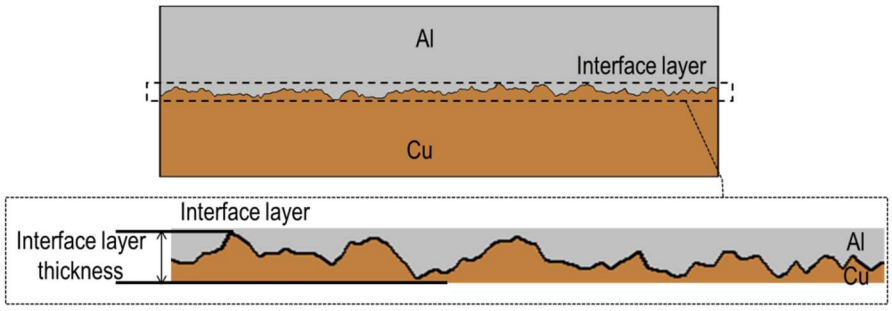

Figure 3.4 Illustration of an interface layer and its thickness

2. Material Properties

There are two types of material properties in the model: macro material properties and local material properties. The macro properties determine the current flowing onset and the energy loss due to conduction to a roll body. Because the sheet thickness is thin, about 0.127 mm per sheet, and there are two sheets in total, the macro properties are treated as a composite sheet with 1:1 Al/Cu volume ratio, as shown in Eqn. 3.1.

$$\chi_{macro} = 0.5\chi_1 + 0.5\chi_2 \qquad \text{(Eqn. 3.1)}$$

where χ can be any material properties, such as density, thermal conductivity, electrical resistivity, and specific heat capacity. χ_{macro} refers to a material property in macro-scale; χ_1 and χ_2 are material properties of two different materials.

Local material properties are determined by local fraction ratios at the interface layer. The interface layer is divided into elements based on the surface topography, as illustrated in Figure 3.5. Please note that the term "elements" in this chapter refers to the element at the interface only because the model is focused on the interface layer. Each element represents a local region at the interface. All the elements have the same element height defined by the interface layer thickness. The "touching level/height" of surfaces of each element varies over the interface based on the surface topography. With the touching level, the volume ratio of materials in each element can be obtained, as described in Figure 3.6. The reference level is defined as the lowest point of the lower surface. Note that the touching level and the element height, i.e., interface thickness, varies with surface displacement since the surfaces are moving toward each other. Therefore, volume ratios are updated in each step, resulting in element material properties changes in each step. The volume ratios are used to calculate material properties of each element, i.e., the local interfacial material properties, by Eqn. 3.2.

$$\chi_{local} = \nu_1\chi_1 + \nu_2\chi_2 \qquad \text{(Eqn. 3. 2)}$$

where ν_1 and ν_2 are the volume fractions of materials 1 and 2. The non-uniform material properties over the interface induce non-uniform Joule heating effect in the interface layer, and the non-uniform local resistivity varies in current distribution across the interface. Consequently, localized heating occurs and hot spots, i.e., regions where the temperatures are noticeable higher than other regions, may be found.

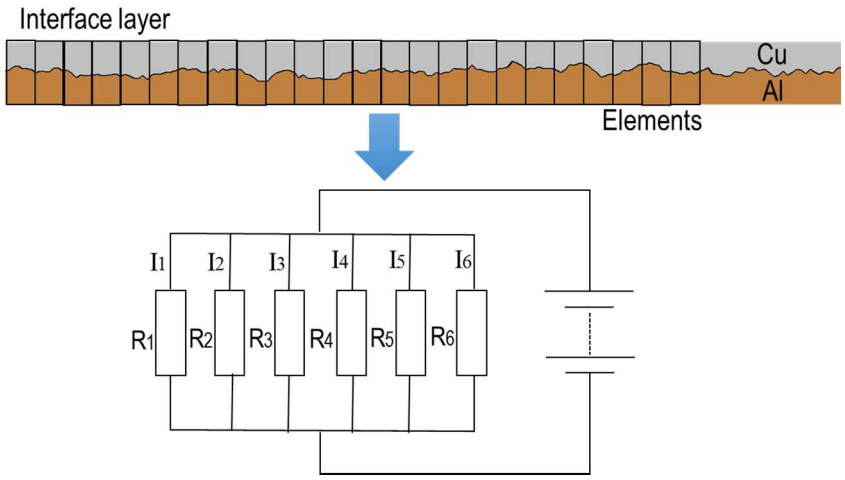

Figure 3.5 Illustration of elements in the interface and their resistance system

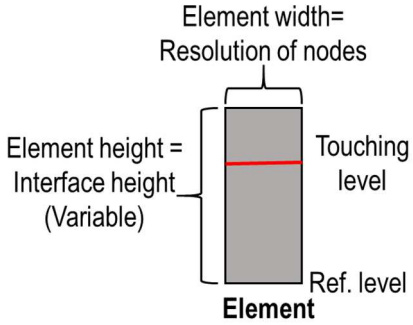

Figure 3.6 Description of touch level defining local/element material properties

3. Current Distribution

It is assumed that electric charges flow across the interface boundary and none of them move along the boundary, as shown in Figure 3.7. The amount of charges flowing into an element depends on the element electric resistance, i.e., the local material resistance. The elements are treated as resistors arranged in parallel as illustrated in Figure 3.5. The equivalent resistance and the current of an element can be calculated by Eqns. 3.3 and 3. 4.

$$R_{eq} = \frac{1}{\sum_i^N \frac{1}{R_{e_i}}} \qquad \text{(Eqn. 3.3)}$$

$$I_{e_i} = I \frac{R_{eq}}{R_{e_i}} \qquad \text{(Eqn. 3.4)}$$

where R_{e_i} and I_{e_i} are the element resistance and current, respectively. N is the number of elements and I is the total current.

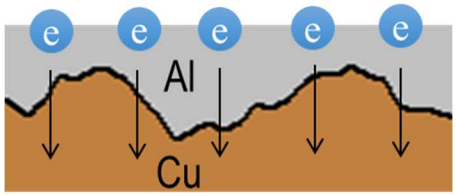

Figure 3.7 Illustration of electric charges flowing across an interface boundary

4. Initiation of Current Flow

A touch between two protrusions on two approaching surfaces is not a good indicator for the onset of current flow. Although the touch closes the "circuit" as depicted in Figure 3.5, its touching area may be too small to allow current flow, resulting in too high electrical resistance. Therefore, a criterion should be defined to determine the instant that current flow begins. In the model, current starts flowing when the equivalent resistance of "contacted" regions at the interface is smaller than the macro resistance, i.e., $R_{eq} < R_{macro}$.

5. Joule Heating Effect

In the physical experiment, current flowed from the upper to lower roll through the sheets. Due to the large mass of the rolls and low current density applied on the roll, the Joule heating effect on the roll was insignificant. Therefore, the Joule heating effect on the roll is ignored in the model. Additionally, because this study focuses on the localized Joule heating effect at the interface layer, the Joule heating in the regions other than the interface is neglected. For the non-

interface regions, macro material properties, which are defined by Eqn. 3.1, are applied. Joule heating effect calculation is conducted in the interface layer. The adiabatic Joule heating effect can be calculated by Eqn. 3.5.

$$\Delta T_J = \frac{J^2 \rho \Delta t}{cd} \qquad \text{(Eqn. 3.5)}$$

where ΔT_J is the adiabatic Joule heating temperature rise. J and Δt are the current density and heating time, i.e., increment time, respectively. ρ, c and d are material properties: electrical resistivity, specific heat capacity, and density, respectively. Equation 3.5 describes the adiabatic Joule heating effect in a unit area. For element with volume, Eqns. 3.6 and 3.7 can be used to determine the Joule heating power and Joule heating energy of element.

$$P_e = {I_e}^2 R_e \qquad \text{(Eqn. 3.6)}$$

$$\Delta E_J = {I_e}^2 R_e \Delta t \qquad \text{(Eqn. 3.7)}$$

where I_e and R_e are the element current and element electrical resistance. Both I_e and R_e can be represented in terms of element current density, J_e, and element electrical resistivity, ρ_e, with Eqns. 3.8 and 3.9.

$$I_e = J_e A_e$$

$$I_e = J_e w_e l_e \qquad \text{(Eqn. 3.8)}$$

$$R_e = \frac{\rho_e h_e}{A_e}$$

$$R_e = \frac{\rho_e h_e}{w_e l_e} \qquad \text{(Eqn. 3.9)}$$

where A_e, w_e, l_e and h_e are the element current passage area, element width, length and height, respectively. By combining Eqns. 3.7, 3.8 and 3.9, the element Joule heating energy can be expressed by Eqn. 3.10.

$$\Delta E_{J_e} = {J_e}^2 \rho_e w_e l_e h_e \Delta t \qquad \text{(Eqn. 3.10)}$$

6. Energy Loss

In the model, energy loss is assumed solely due to the thermal conduction from the sheets to the roll body. It is assumed that energy distributes evenly over the interface at the end of each step, and transfers from the interface to the sheet surface and then to the roll body in the sheet thickness direction. The sheet surface temperature, T_s, can be found by Eqn. 3.11 and it can be used to obtain the energy loss at interface by Eqn. 3.12.

$$\frac{K_{mat}(T_i - T_s)}{L_{mat}} = \frac{K_{roll}(T_s - T_\infty)}{L_{roll}} \qquad \text{(Eqn. 3.11)}$$

$$\Delta E_{loss} = \frac{K_{mat}(T_i - T_s)}{L_{mat}} \Delta t \qquad \text{(Eqn. 3.12)}$$

The K_{mat} and K_{roll} are the macro thermal conduction coefficients of material and roll. K_{mat} is found by Eqn. 1. L_{mat} is the distance between the interface and the sheet surface, where it comes into contact with the roll surface, and L_{roll} is the distance from the roll surface to a point where its temperature reaches room temperature. It is assumed that the heat transferred from the sheet dissipates in the infinite length with respected to the sheet thickness; therefore, it is assumed $L_{roll} = 100L_{mat}$. T_i, T_s and T_∞ are the macro temperature at the interface, sheet surface and room temperature respectively. Because it is assumed that energy distributes evenly over the interface at the end of each step, the interface temperature, T_i, is defined by the mean interface temperature obtained by Eqn. 3.13.

$$T_i = \frac{\sum f T_e}{\sum f} \qquad \text{(Eqn. 3.13)}$$

where T_e is the element temperature and f is frequency of T_e found in the elements.

Since Eqn. 3.12 is in macro scale, the element heat loss due to conduction is assumed to be divided by the total number of element at the interface, N, as shown as in Eqn. 3.14.

$$\Delta E_{loss_e} = \frac{\Delta E_{loss}}{N} \qquad \text{(Eqn. 3.14)}$$

With Eqns. 3.10 and 3.12, the element net energy can be obtained via Eqn. 3.15 and the element temperature rise can be found by Eqn. 3.16.

$$\Delta Q_e = \Delta E_{J_e} - \Delta E_{loss_e} \qquad \text{(Eqn. 3.15)}$$

$$\Delta T_e = \frac{\Delta Q_e}{c_e d_e w_e l_e h_e} \qquad \text{(Eqn. 3.16)}$$

Since it is assumed that energy distributes evenly over the interface at the end of the previous step, initial temperature of each step is defined as the macro interface temperature, T_i, obtained in the previous step. As a result, the element temperature can be expressed in Eqn. 3.17.

$$T_e = T_i^o + \Delta T_e \qquad \text{(Eqn. 3.17)}$$

where T_i^o is the macro interface temperature with the consideration of heat loss in the previous step.

7. Modeling Algorithm

The algorithm of the model is shown in Figure 3.8. At the beginning, 3-dimensional surfaces, both upper and lower faces with actual measured topography, are generated with desired resolutions. Each data point describing the topography of the surface is treated as a node, as shown in Figure 3.9. In other words, the nodes are the coordinates of data points of the surface topography. Therefore, the resolution of the surface topography is actually the mesh size of elements. Both surfaces should have the same resolutions so that their nodes can align with the nodes on the facing surface enabling "touches" when surfaces are approaching each other. Each element is comprised of 4 nodes and it is formed when 4 adjacent nodes come into contact. Two surfaces are facing each other and moving toward each other according to the designated displacement increment. In this study, 0.2 and 0.4 μm per step are used. After each increment, all nodes are checked if they are touching with the facing nodes to form an element. It is defined that current flows through a surface instead of a point to induce Joule heating, which is

determined by a current density over an area. An element is formed once 4 adjacent nodes touched with facing nodes. Then, the material properties of element are defined by the volume fraction which is determined by the touching level as described in Figure 3.6. Note that the touching level and the element height, i.e., the interface thickness, are updated in every step. As a result, material properties change as the process goes on. Next, equivalent resistance of all formed elements is calculated with Eqn. 3.3. If the criterion for current flow onset is met, i.e., $R_{eq} < R_{macro}$, current starts flowing and Joule heating effect occurs. The two surfaces keep closing and Joule heating continues until all nodes are touched, which means the surfaces are completely closed.

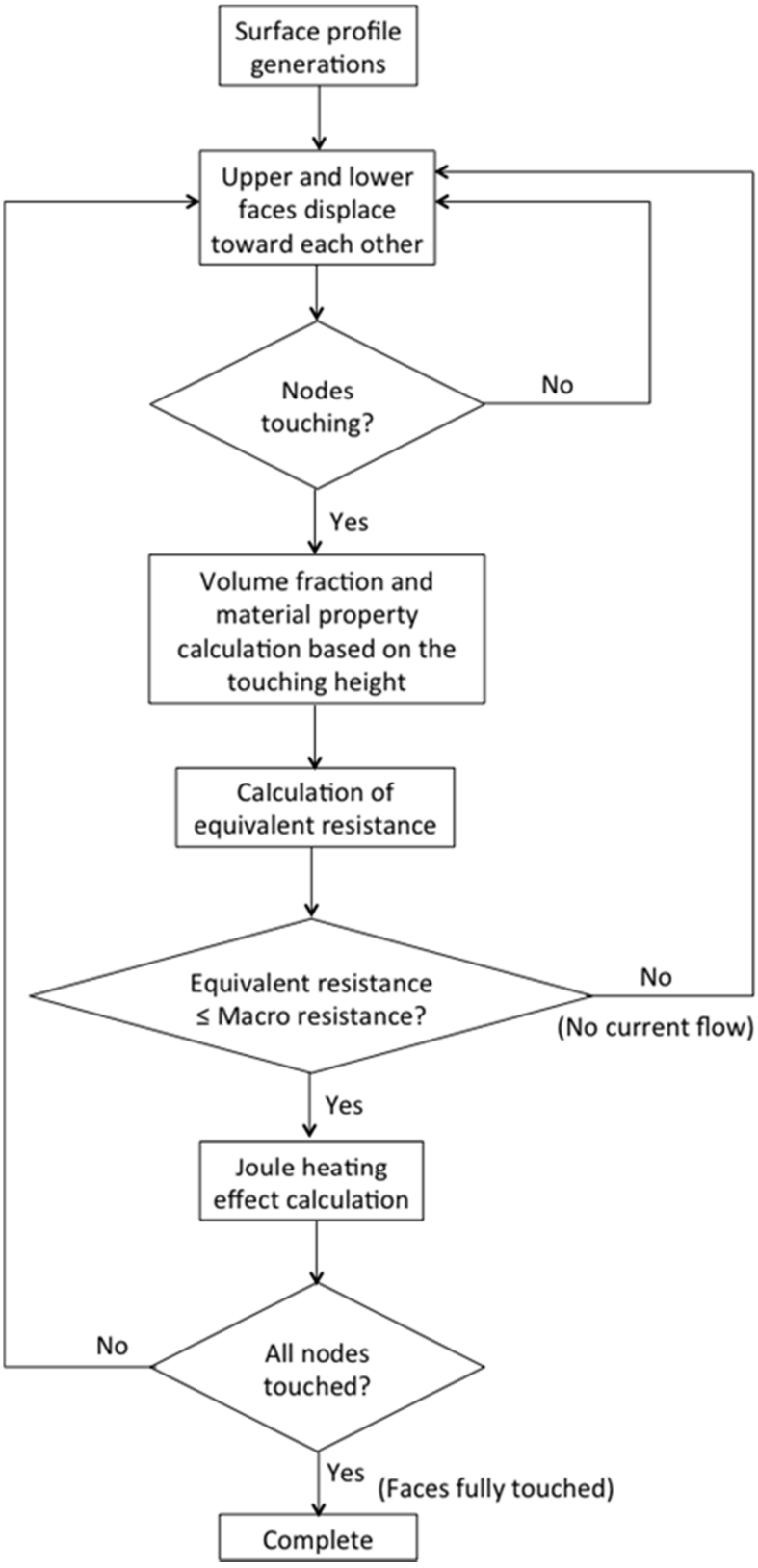

Figure 3.8 Model algorithm

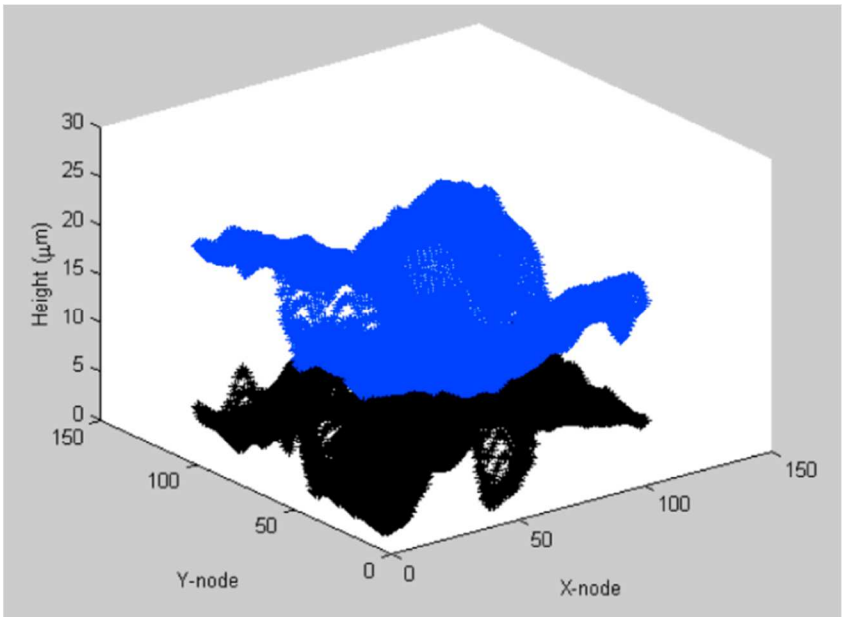

Figure 3.9 Upper and lower surfaces presented by nodes

8. β : A ratio of mesh resolution to step increment

Equation 3.10 is rearranged into Eqn. 3.18. In Eqn. 3.18, I_e is a process parameter and ρ_e is the material properties. Δt is the heating time, which is defined by the step time. A_e is the current passage area, i.e., mesh size, depending on the topography of a surface. Both Δt and A_e exercise numerical influence on the simulation results. Although h_e, i.e., the interface layer thickness, is also surface topography-dependent, its variation is not significant enough to exert as critical an effect as A_e does on Joule heating. Recalling from the previous section, an element size depends on the topography resolution of a measured surface; a lower resolution gives a larger A_e.

$$\Delta E_{J_e} = \left(\frac{I_e}{A_e}\right)^2 \rho_e A_e h_e \Delta t$$

$$\Delta E_{J_e} = \frac{I^2}{A_e} \rho_e h_e \Delta t \qquad \text{(Eqn. 3.18)}$$

In the simulation, surfaces are approaching each other under a constant displacement velocity, v. The displacement velocity determines both the step time, Δt, and the surface displacement

increment per step, Δs. Note that v is a physical parameter while Δt and Δs are numerical parameters. Their relations are described in Eqn. 3.19.

$$v = \frac{\Delta s}{\Delta t} \qquad \text{(Eqn. 3.19)}$$

In order to generate a simulation result close to practice, both the numerical Δt and Δs should be set to match the physical v. Please note that the step time, Δt, is driven by the surface displacement increment, Δs, in the simulation. Additionally, A_e is driven by the surface topography resolution. Since square element is applied, $A_e = l_e \times w_e = l_e^2$. Element length, l_e, is taken to represent the mesh size. The effects of Δs and l_e on maximum local temperature are shown in Figure 3.10. The time in x-axis refers to the period of time from when Joule heating starts until two surfaces are contacted completely. Therefore, the time is short, which is about 0.22 s. Note that surface topography resolutions which determine the mesh size will slightly affect the process time. The maximum local temperature refers to the highest element temperature and it is not necessarily always at the same spot during the entire process. From Figure 3.10, the local temperature is very sensitive to the mesh size, l_e, and surface displacement increment, Δs. They may lead to unreasonably high local temperature. Ideally, physical results, i.e., the local temperature in this case, should be as insensitive as possible to the change of numerical parameters, Δs and l_e. In other words, curves in Figure 3.10 should be coincident or as close as possible. In order to eliminate the dependency of numerical parameters to the physical results, a ratio, β, is introduced as a sensitivity indicator of Δs and l_e on the calculated temperature. It is used to determine reliable results (details will be given in "Results" section). The β is expressed with numerical parameters. It is a ratio of mesh size to displacement increment. Meanwhile, it also implicitly links numerical and physical parameters together. The derivation of β is shown in Eqn. 3.20.

$$\beta = \frac{Mesh\ size}{Surface\ Displacement\ velocity \times Heating\ Time} \qquad \text{(Eqn. 3.20.1)}$$

$$\Rightarrow \qquad \beta = \frac{l_e\ [\mu m]}{v\ [\mu m/s] \times \Delta t[s]} \qquad \text{(Eqn. 3.20.2)}$$

$$\beta = \frac{l_e\ [\mu m]}{\frac{\Delta s\ [\mu m]}{\Delta t\ [s]} \times \Delta t[s]} \qquad \text{(Eqn. 3.20.3)}$$

$$\beta = \frac{l_e\ [\mu m]}{\Delta s\ [\mu m]} \qquad \text{(Eqn. 3.20.4)}$$

In Eqn. 3.20.1, numerical (the numerator) and physical (the denominator) parameters influencing the Joule heating effect are linked together, and their symbols and units are shown in Eqn. 3.20.2. v and Δt are physical parameters and they are constrained by Eqn. 19. The conversion of v in Eqn. 3.20.3 makes Δt from a physical parameter, i.e., heating time, to a numerical parameter, step time. The effect of Δt, which is determined by Δs, is "cancelled" out. Note that Δs is controlled by a physical v according to Eqn. 3.19. β is a ratio of mesh size, l_e, to displacement increment, Δs. The effect of β is going to be discussed in the "Results" section.

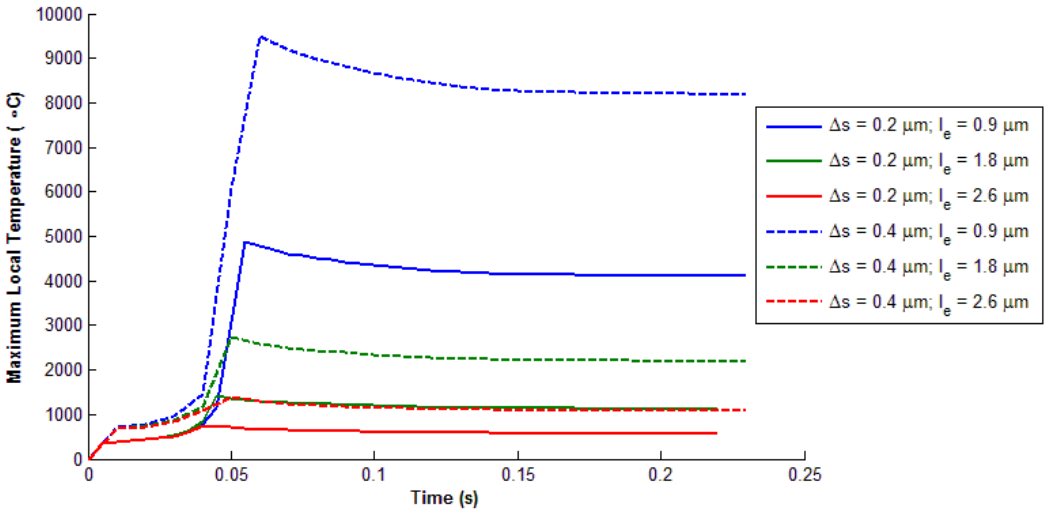

Figure 3.10 The effects of step increment (Δs) and mesh size (l_e) on the maximum local temperature history

3.4 Model Implementation and Results

The model was converted into a MATLAB program for simulation. In this section, simulation was tested with different numerical parameters in order to determine which would yield the most reasonable and realistic results. With the appropriate numerical parameters, macro and local interface temperatures are predicted and compared.

1. Model Setup

Two manually brushed surfaces were measured by an optical 3D microcoordinate system, *Alicona InfiniteFocus*, with x/y-resolution and z-resolution of 0.87 μm and 0.0001 μm, respectively. Their contour images are shown in Figure 3.11. Each surface was 250 μm by 250 μm. The upper and lower surfaces represent commercially pure aluminum and commercially pure copper surfaces, respectively. The roll, which contacts with the sheet laminate leads to conductive energy loss of the sheet, is made with D2 tool steel. Material properties of commercially pure Al and Cu as well as D2 tool steel are tabulated in Table. 3.1. The surface displacement velocity and current density was 40 μm/s and 15 A/mm^2, respectively. These values are similar to the actual EARB process conducted experimentally for this study. In this study, two surface displacement increments, Δs, were used: 0.2 μm and 0.4 μm. The step time, Δt, was driven by Δs according to Eqn. 3.19. The model was simulating a process under a room temperature of 25 °C. In the simulation, different β were applied for investigation. The mesh size and total number of elements are shown in Figures 3.12 and 3.13, respectively. Region with $\beta >$ 20 in Figure 5.13 is magnified and shown in Figure 3.14.

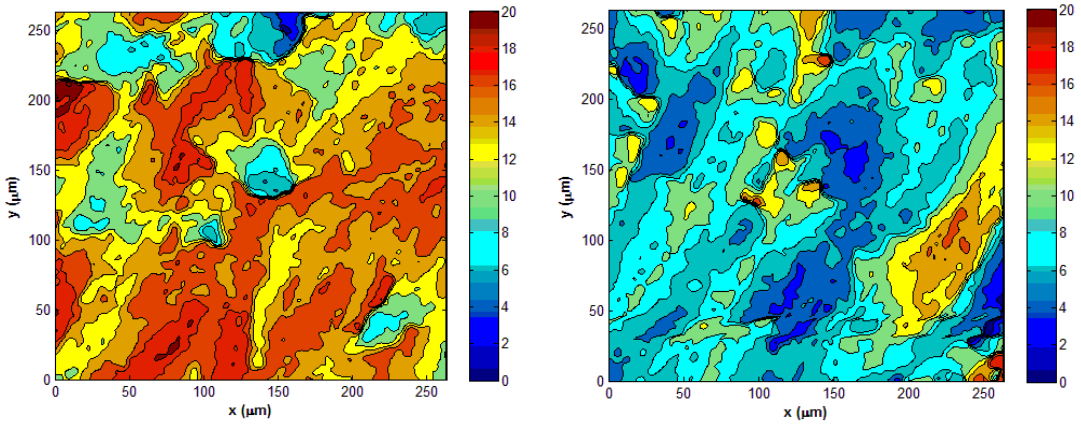

(a) (b)

Figure 3.11 Contour of (a) upper surface mimicking aluminum surface and (b) lower surface mimicking copper surface

Table 3.1: Material properties of aluminum and copper applied in the simulation

	Aluminum	Copper	D2 Tool Steel
Density (Kg/m^3)	2700	8900	7700
Specific heat capacity (K/kg-C)	904	385	461
Thermal conductivity (W/m-K)	210	391	36
Electrical resistivity (Ω-m)	2.7e-4	17e-9	----

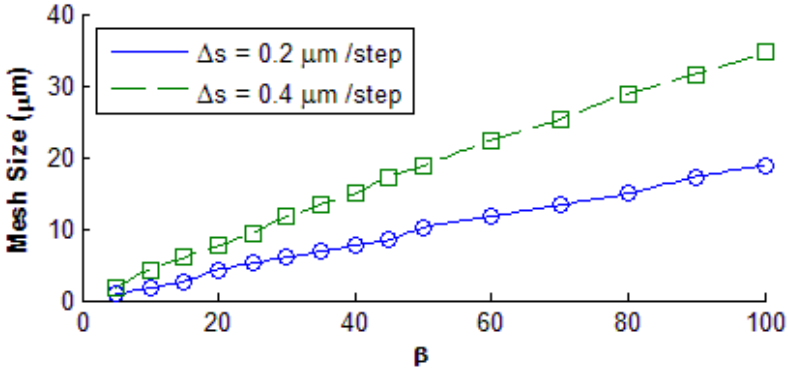

Figure 3.12 Mesh size with different β and Δs

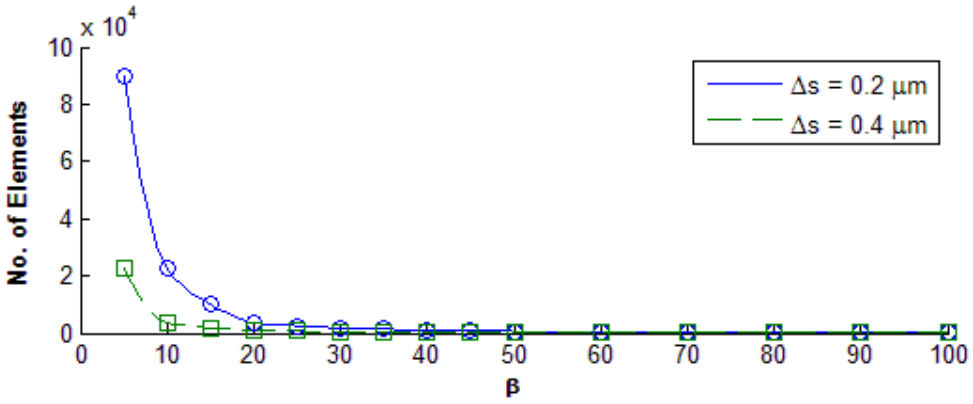

Figure 3.13 Number of elements with different β and Δs

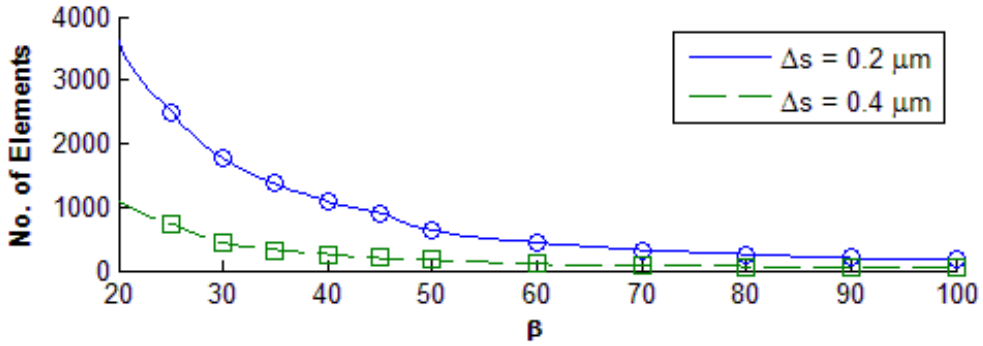

Figure 3.14 Number of element with different β and Δs. (Magnification of Figure 3.13)

2. Local Interface Temperature

As mentioned in the previous section, curves of different Δs in Fig, 3.10 are expected to be as close as possible. In order to study the sensitivity of model with β, the differences in temperatures calculated with Δs = 0.2 μm and 0.4 μm are studied. Figure 3.15 is the illustration of two temperature histories generated with two different displacement increments, Δs, but with the same β. Note that although the increments are different, they have the same physical surface displacement velocity. The temperature in Figure 3.15 can be referred to either maximum local temperature or macro interface temperature. The time in x-axis is the process time which is from

the onset of current flow until the upper and lower surfaces are completely in contact. The temperature difference between two curves at time t is defined as ε_t. In order words, ε can be understood as the "tolerance range" on the difference between temperatures found with different increments. The overall ε of a β in the entire process is denoted as ε_β and is defined by Eqn. 3.21.

$$\varepsilon_\beta = \frac{\sum_i^n \varepsilon_{t_i}}{n} \qquad \text{(Eqn. 3.21)}$$

where n is the total number of steps. ε is denoted as, for example, ε_{10} if β is 10. Equation 3.21 is applied to find ε_β for the "tolerance range" tests for both maximum local temperature and macro interface temperature. ε_β^L and ε_β^M are used to distinguish the ε_β between local and macro temperature, respectively. The superscripts L and M refer to "Local temperature" and "Macro temperature", respectively. It is expected that ε_β is as small as possible so that curves in Figure 3.15 align with each other. Therefore, the ideal values for ε_β^L and ε_β^M would give the smallest tolerance range on the temperatures found with different increments.

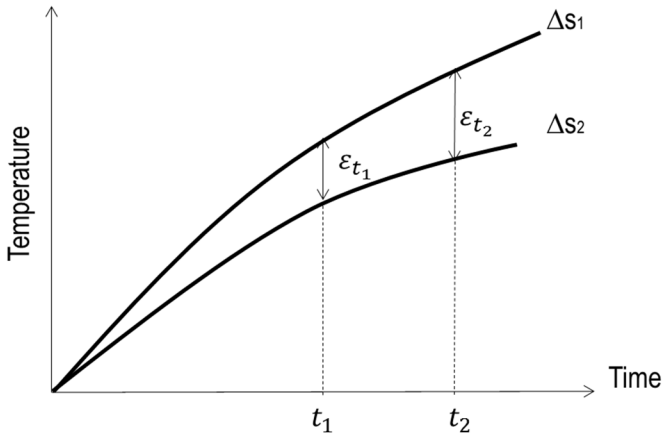

Figure 3.15 Illustration of ε in curves generated with different increments, Δs

The relation between ε_β^L and β is shown in Figure 3.16. As melting and recrystallization of aluminum are suspected during EARB according to the microstructure observed in the Al/Cu bonded sheets in the previous investigation, ε_β^L is normalized by the melting point of aluminum, which is about 660 °C. The normalized ε_β^L gives an insight on the significance of temperature difference between two curves with respect to aluminum melting point. A small normalized ε_β^L value gives a better guarantee that the overall temperature difference between temperatures found with different increments is not large enough to cause phase change of aluminum, such as melting. In other words, smaller ε_β^L keeps the calculated temperature variance in a smaller tolerance range. From Figure 3.16, when β = 5, ε_5^L is about 2000 °C, which means the average difference in temperature, calculated with Δs = 0.2 μm and 0.4 μm, is about 2000 °C. Note that ε_β is expected to be as small as possible. ε_β^L drops rapidly after β = 5 and becomes relatively stable when β = 25. The region of β from 20 to 100 is magnified in Figure 3.17. From β = 25 to 50, ε_β^L is rather stable; its value varies between 40 and 80 °C, which is about 0.1 after normalization. Compared to the high maximum local temperature, the ε_β^L values are small so that the local temperature curves given by Δs = 0.2 μm and 0.4 μm are almost coincident as shown in Figure 3.18. Starting from β = 60, fluctuation of ε_β^L increases and becomes less stable. However, the normalized ε_β^L is still low when compared to the cases that β < 25 from Figure 3.16; it is about 0.1-0.2, as can be seen in Figure 3.17.

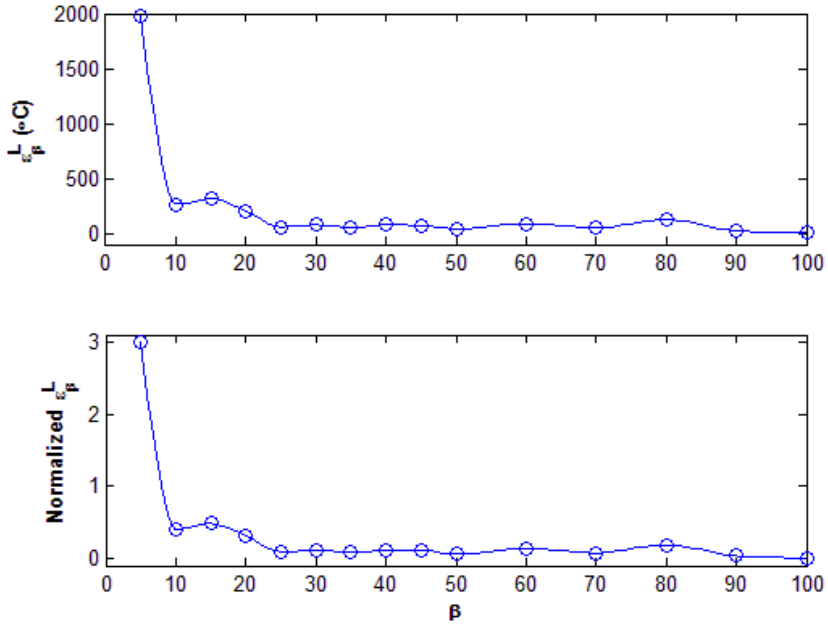

Figure 3.16 Absolute and normalized ε_β^L given by different β simulated with pre-defined current density

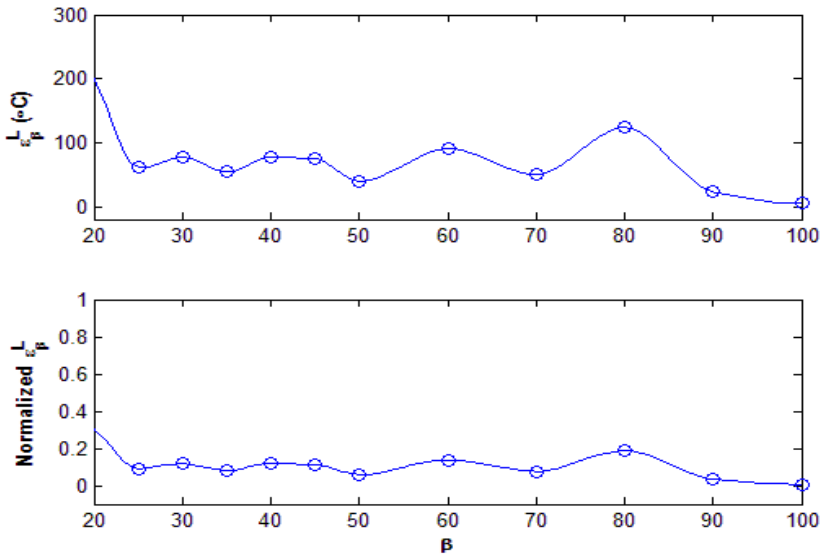

Figure 3.17 Absolute and normalized ε_β^L given by different β simulated with pre-defined current density (Magnification of Figure3.16)

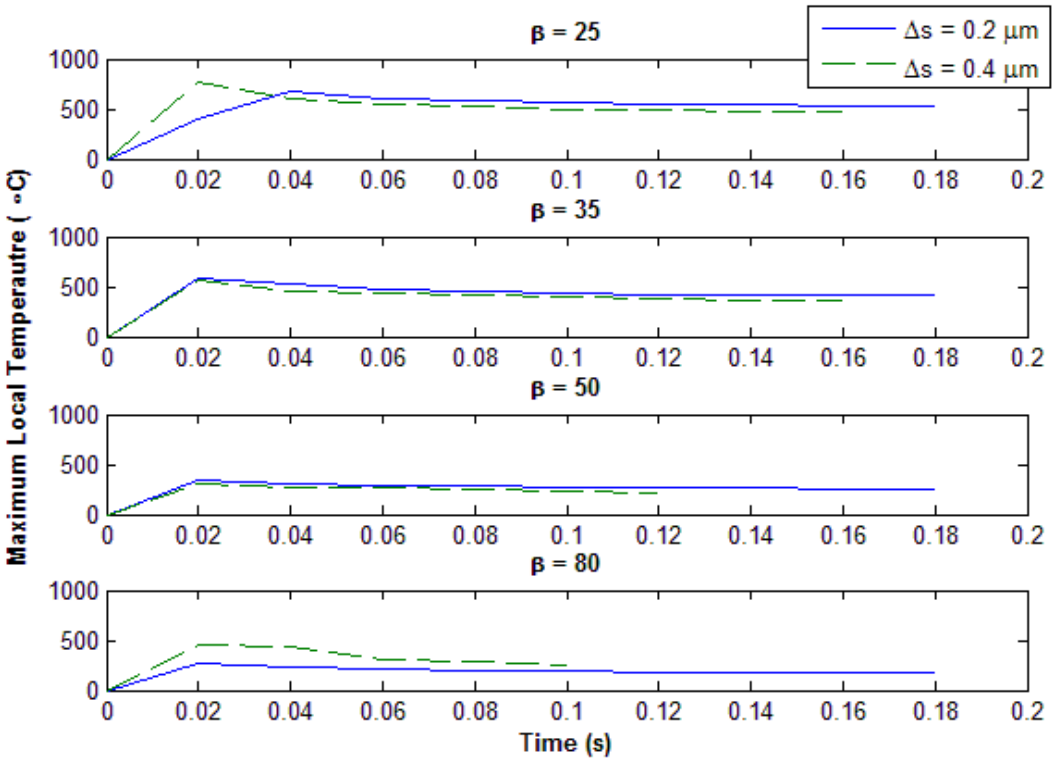

Figure 3.18 Temperature histories of different βs given by different displacement increments, Δs

From Figure 3.18, both increments give similar temperature history with the same β. However, gradual drops of maximum local temperature are noticed when β increases. The drops are due to the decreases on the total current size caused by numerical errors even though both the current density and surface size are pre-defined. Note that numerical errors are inherent errors in computational calculations. The total current size depends on the current density, mesh size and the total element number. It is expressed in Eqn. 3.22. Note that the total current size is calculated at the beginning of the simulation and remains unchanged during the entire simulation.

$$I_{total} = NJw_e l_e \qquad \text{(Eqn. 3.22)}$$

The percentage of total initial current loss due to numerical errors with different β is shown in Figure 3.19. Reference current size is defined as the total current size with the finest mesh size of the corresponding Δs and it is assumed as the current size without current loss. Since the reference current size is the current size expected to be assigned to the model, it is also call assigned current size in this case. Figure 3.19 shows that total current size decreases with increasing β even though current density is pre-defined. (The case with pre-defined current size is going to be discussed in the "Discussions" section.) The decrease of current size causes the decrease of maximum local temperature with increasing β in Figure 3.18. For a better comparison, temperature histories of the selected β are shown in Figure 3.20. Only the temperature histories with $\beta > 25$ are selected because they give small ε_{β}^{L}, which means the results are insensitive to numerical displacement increment. In order to determine which β gives a more reliable local temperature, the sensitivity of current loss corresponding to the element size should be understood. Actual current size and element area are normalized by assigned current size and reference area. Reference area is defined as the total interface area. Normalized actual current size and normalized element area are represented by η and ξ, respectively, as expressed in Eqns. 3.23 and 3.24.

$$\eta = \frac{Acutal\ Current\ Size}{Assigned\ Current\ Size} \qquad \text{(Eqn. 3.23)}$$

$$\xi = \frac{Element\ Area}{Interface\ Area} \qquad \text{(Eqn. 3.24)}$$

Figure 3.21 is the log(η) – log(ξ) relationship in this pre-defined current density simulation. Log(η) drops significantly after the log(ξ) corresponding to $\beta = 25$. It reflects that the magnitude of change in normalized actual current size when $\beta > 25$ is significant with respect to the mesh size. In other words, the current losses in the cases $\beta \leq 25$ are comparable. On the contrary, the

current sizes in the cases $\beta > 25$ are not large enough to give a comparable Joule heating effect compared to the case in which the assigned current is expected without current loss. By the consideration of ε_{β}^{L}, a more realistic result can be achieved when $\beta = 25$. It gives a maximum local temperature approximately 600 °C on average from Figure 3.20. Figure 3.22 is the temperature distribution over the interface at the end of the simulation. A hot spot can be seen in the figure. Note that Figure 3.22 is taken at the end of the simulation, therefore, its hot spot temperature is lower than 600 °C because part of the current is distributed to other regions, diminishing the local Joule heating effect.

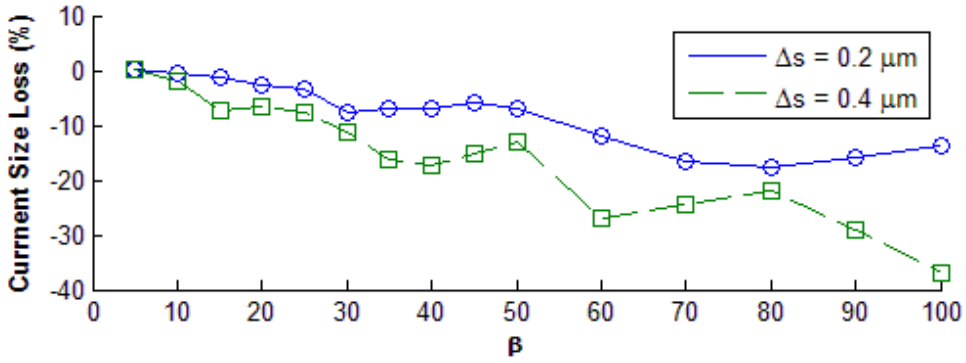

Figure 3.19 Percentage of current size loss in the current density pre-defined simulation with different β

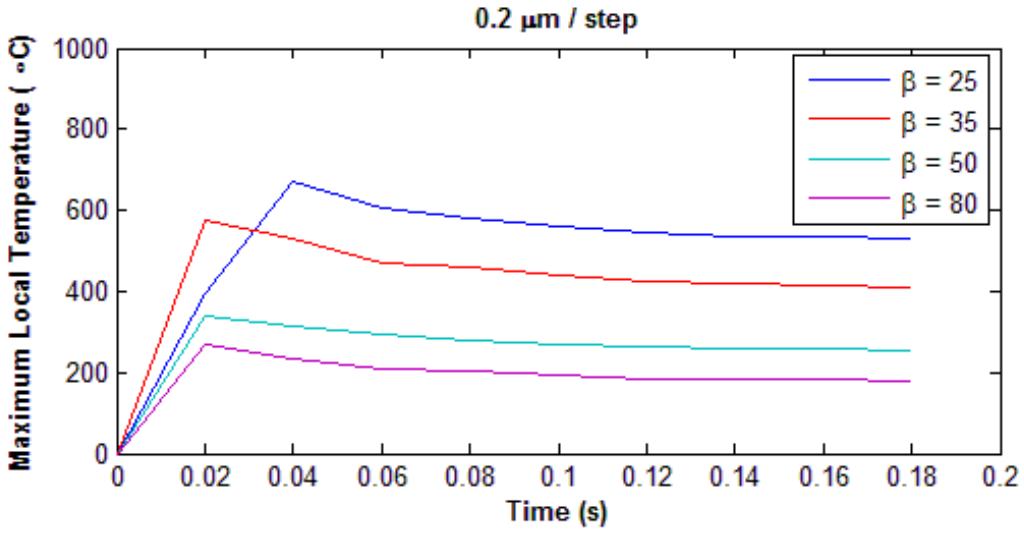

Figure 3.20 Maximum local temperature histories of selected β when Δs = 0.2 μm

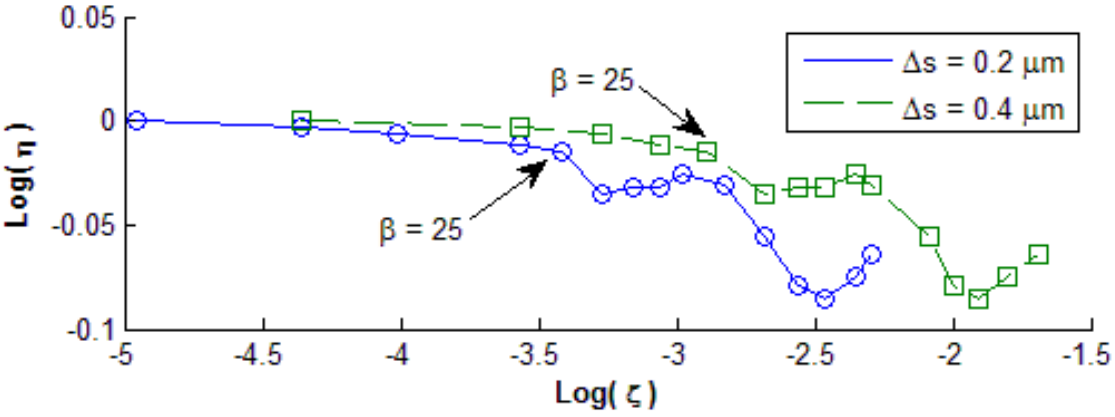

Figure 3.21 log(η) – log(ξ) curves of pre-defined current density simulation

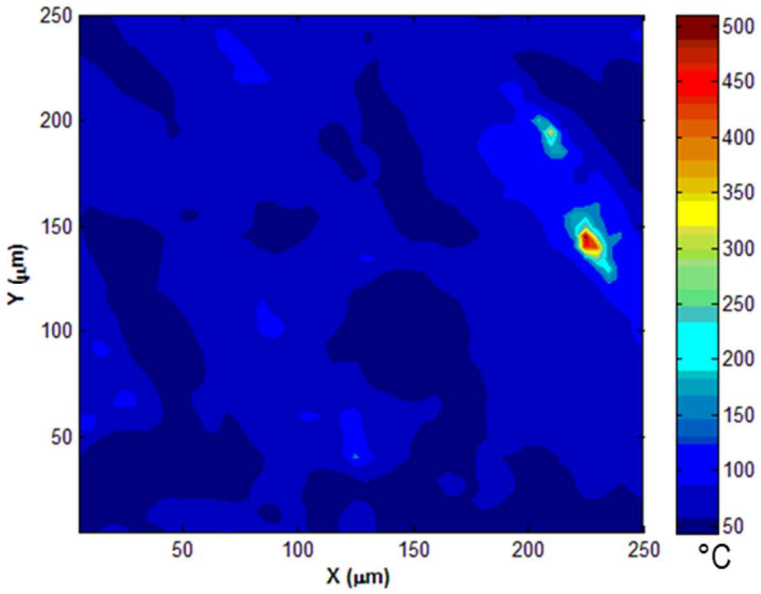

Figure 3.22 Temperature distribution on the interface at the end of the simulation. (β = 25, Δs = 0.2 μm)

3. Macro Interface Temperature

The numerical effect of surface displacement increment, Δs, on macro interface temperature is investigated. Figure 3.23 shows the relation between ε_β^M and β. The macro interface temperatures were found according to Eqn. 3.13. Results show that, generally, ε_β^M is small although it trends to increase with β. The absolute ε_β^M is varying between 1 ° C to 15 °C. After normalization of ε_β^M, the value of normalized ε_β^M is only about 0.02 in maximum. The results reflect that the selected Δs does not give a significant impact on macro interface temperature. Macro temperature histories of selected β when Δs = 0.2 μm is shown in Figure 3.24. There are no remarkable differences in macro interface temperatures in different β cases. The macro temperature is about 70 °C on average. Compared to the maximum local temperatures in Figure 3.20, the macro interface temperature is low. This shows that high local interface temperatures or hot spot

temperatures are not reflected by the macro interface temperature. Further discussion will be given in the "Discussion" section.

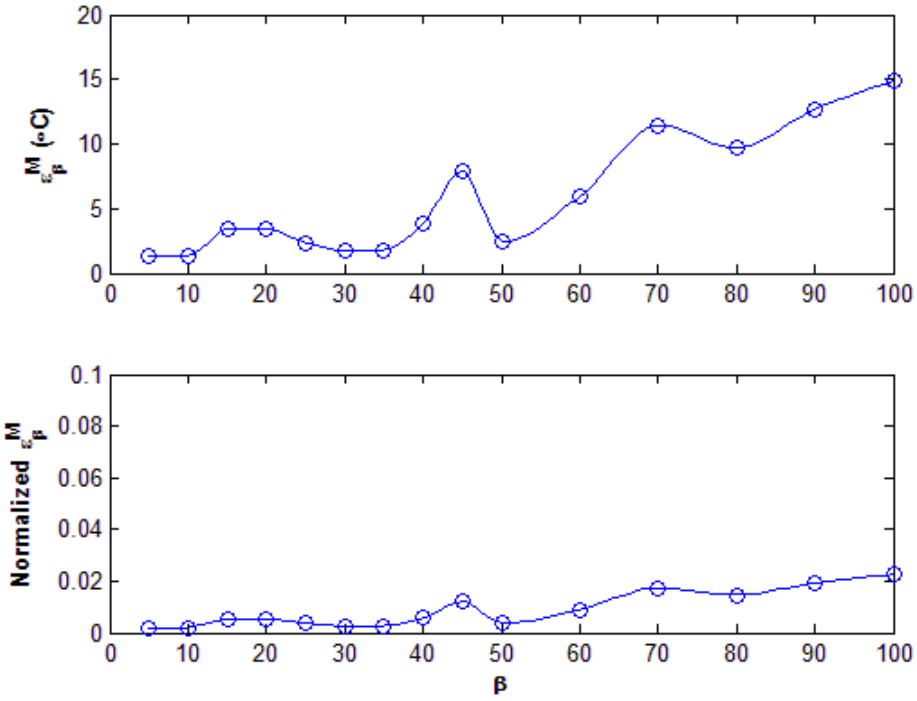

Figure 3.23 Absolute and normalized ε_β^M given by different β simulated with pre-defined current density

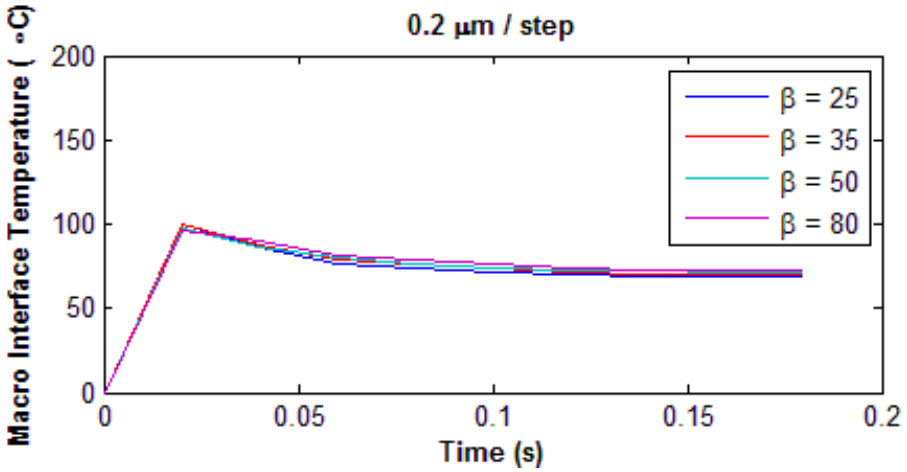

Figure 3.24 Macro interface temperature histories of selected β when Δs = 0.2 μm

3.5 Discussion

The model was tested and appropriate numerical parameters were found in the previous section. To further discuss the Joule heating effect in the process, the simulation was repeated with an additional surface pair set for deep investigation. Moreover, the numerical errors affecting this model will also be discussed in this section.

1. Local and Macro Interface Temperatures

Simulation results show that high local interface temperatures are not reflected by macro interface temperatures. In the simulation, maximum local temperature is around 600 °C, while the macro temperature is only about 70 °C. The simulated local interface temperatures are proved by the experimental microstructure observation, as shown in Figure 3.2. Nanocrystalline particles were found in some locations instead of the entire interface. It indicates that only some regions had temperatures higher than the recrystallization temperature or the melting point of the material. The hot spot strengthened the bonding of metals locally and led to non-uniformed bond strength over the bonded interface. The non-uniformed bond strength was reflected by the changing peeling force in the peeling tests of the sheets produced by EARB, as shown in Figure 3.1. The reason that the hot spot temperatures in the interface are not captured by the macro interface temperature can be attributed to the very fine hot spot zone; the hot spot zone is too small, compared to the interface area. Figure 3.25 is the area percentage "occupied" by different local temperatures at the end of the simulation under the conditions of Δs = 0.2 μm and β = 25. The blue line ("Surface Pair Set 1") is the result generated with the surface pair shown in Figure 10. The interface is 250 μm by 250 μm large. Assuming 200 °C is the crystallization temperature of aluminum (1/3 of the aluminum melting point), 0.5% of the area has the temperature higher than the recrystallization temperature of aluminum. Only 0.12% of the area is above 400 °C. As

a result, high local temperature is not captured by the macro interface temperature. This localized heating effect is a feature of electrically-assisted processes. In order to prove its dependency on surface topography, another surface pair (Surface Pair Set 2) was applied for further investigation. The topography of the surface pair is shown in Figure 3.26. In this surface pair set, the upper surface was as the same as Set 1 but the lower surface was changed. In Figure 3.25, the highest local temperature at the end of the simulation is about 320 °C and is lower than that from Surface Pair Set 1, which is about 530 °C. There is about 0.24 % of the area above recrystallization temperature of aluminum (200 °C). The macro interface temperature for Set 2 is about 90 °C while it is about 70 °C for Set 1. There is about 96 % and 83 % of the area below 100 °C for Set 1 and Set 2, respectively. The results are tabulated in Table 3.2 for an easy comparison. The results prove that topography of surface pairs does not remarkably vary macro interface temperatures but it exerts considerable impacts on local temperatures. The results also give an explanation on the non-uniform peeling force during the peeling test of an EARB bonded Al/Cu sheet. The manually brushed metal surfaces gave a non-uniform surface topography and led to a variation of hot spot distribution and local temperature, resulting in a bond strength variation at the interface. Furthermore, from the results shown in Figure 3.27, the hot spots are found in the regions with low aluminum volume fraction, i.e., the regions with high copper volume fraction. The results give an insight that smoother aluminum surface with rougher copper surface may have a higher chance to produce hot spots at the bonding interface.

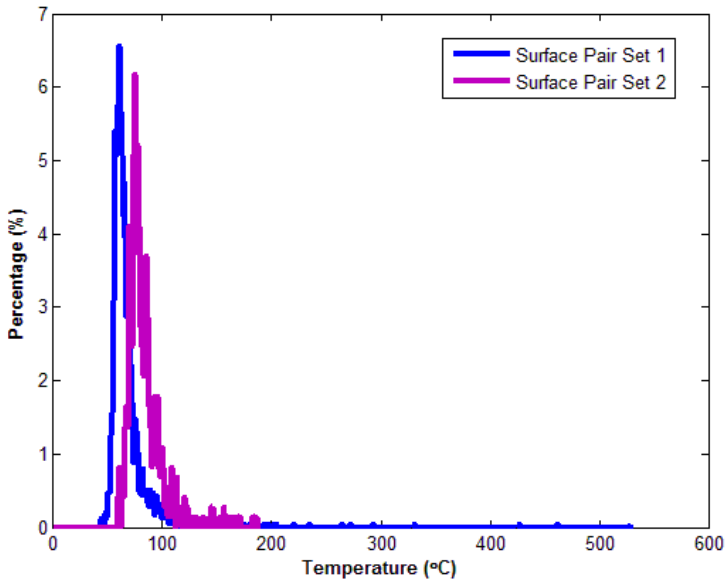

Figure 3.25 Area percentage distribution of local interface temperature at the end of simulation. (Δs = 0.2 μm and β = 25)

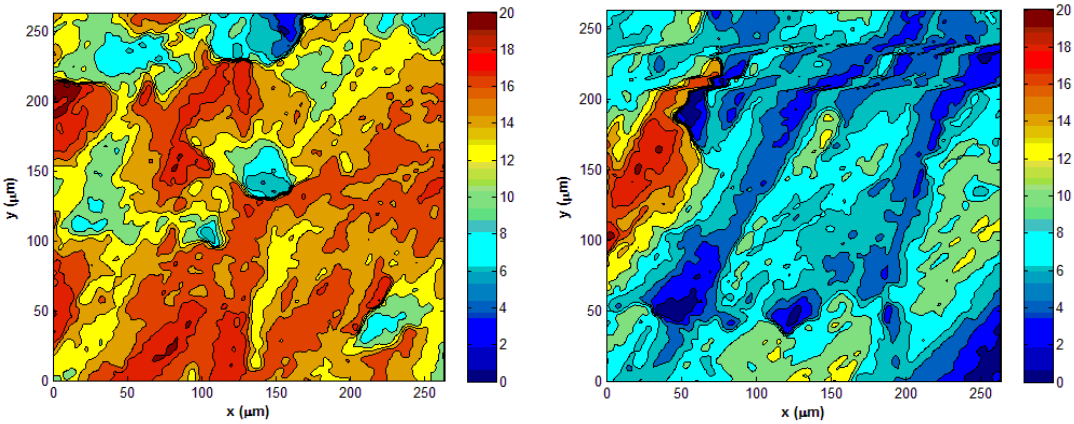

(a) (b)

Figure 3.26 Contour of surface pair set 2: (a) upper surface mimicking aluminum surface, and (b) lower surface mimicking copper surface

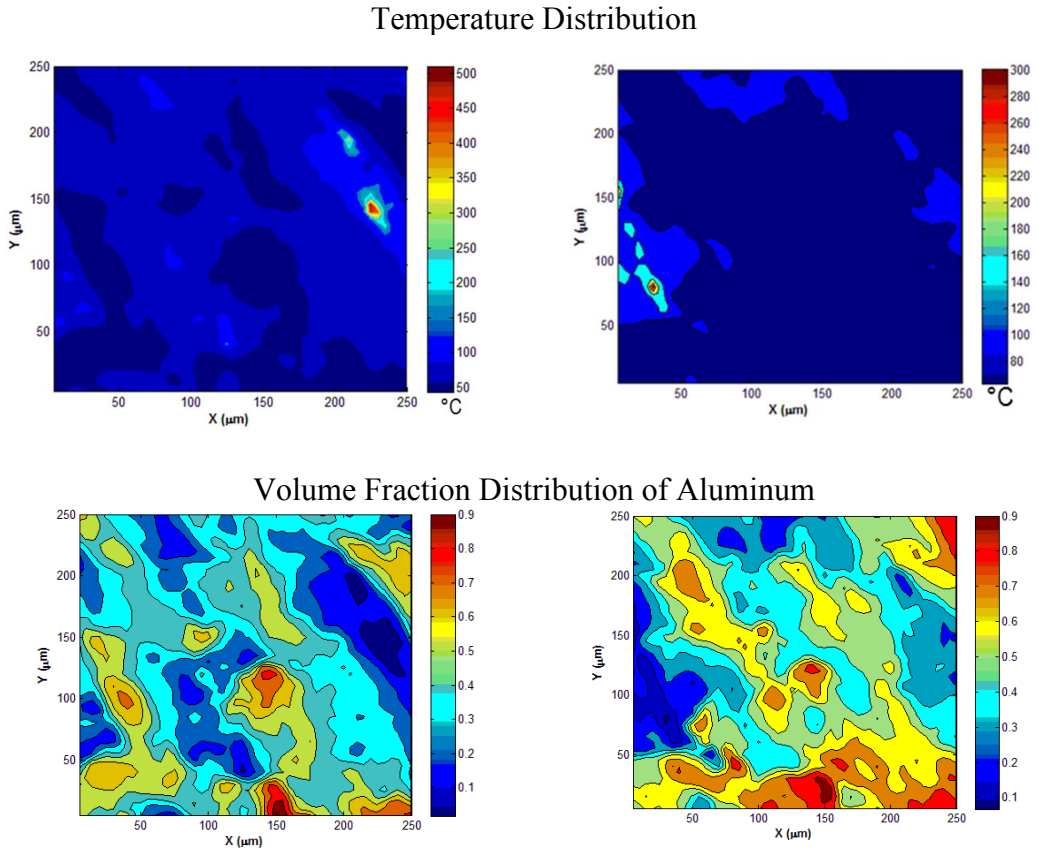

(a) Surface Pair Set 1 (b) Surface Pair Set 2

Figure 3.27 Temperature distribution and volume fraction distribution of aluminum at (a) Surface Pair Set 1, and (b) Surface Pair Set 2

Table 3.2: Interface temperature comparison between surface pair sets 1 and 2.

Surface Pair Set	1	2
Highest local interface temperature (°C)	530	320
Macro interface Temperature (°C)	70	90
Percentage of area below 100 °C (%)	96	83
Percentage of area above 200 °C (%)	0.5	0.24
Percentage of area above 400 °C (%)	0.12	0

2. Current Size and Current Density Losses

As mentioned in the "Model Implementation and Results" section, a numerical error caused an initial current size loss, as shown in Fig 3.19. Instead of assigning current density to the model which has been conducted in the prior section, constant initial current size is assigned to the model for interface temperature investigation. The assigned current size was the maximum current size, i.e., without loss, in the pre-defined current density case done earlier. The purpose of this investigation is to find out the interface temperatures in the case without current size loss. Same surface pair set, i.e., Set 1, (Figure 3.11) was used. Figures 3.28 and 3.29 show the ε_β^L and ε_β^M trends of the pre-defined current size case, respectively. Similar to the pre-defined current density case in the prior sections, ε_β^L becomes stable when $\beta \geq 25$. However, it increases and becomes more fluctuated after $\beta > 50$. ε_β^L in the β range between 20 and 50 is magnified and compared with those from the pre-defined current density case in Figure 5.30. Results show that, in the case of pre-defined current size, the values of normalized ε_β^L in this β range are less than 0.1. It means the maximum local temperatures found with Δs = 0.2 μm and Δs = 0.4 μm are consistent in the β range between 25 and 50. Meanwhile, from Figure 3.28, although results show that ε_β^M increases and becomes less stable when β increases, it maintains small values; its normalized ε_β^M is less than 0.05 in general. The region of ε_β^M in β range between 25 and 50 is magnified and compared with the pre-defined current density case is shown in Figure 3.31. In the case of pre-defined current size, the absolute ε_β^M and normalized ε_β^M vary in the range of 5-25 °C and 0.01-0.04, respectively. In the β range between 25 and 50, small normalized ε_β^L and ε_β^M values in both the pre-defined current density and the pre-defined current size cases prove that

the differences between maximum local temperatures found with Δs = 0.2 μm and Δs = 0.4 μm are small with respect to the melting point of aluminum. Therefore, results in this β range can be brought together for comparison. In the case of pre-defined current density, it is shown that a more valid result is given when β = 25 because of (1) its small corresponding ε_{β}^{L} and ε_{β}^{M}, and (2) its insignificant current size loss. Note that the current size loss in the pre-defined current density case when β = 25 is less significant and is supposed to have a comparable effect in the pre-defined current size case, in which its current size is defined as the "current size without loss" in the pre-defined current density case. For the pre-defined current size case, the "current density loss" is shown in Figure 3.32. It is similar to the trend of current size loss in the pre-defined current density case, in which current density decreases with increasing β due to inevitable numerical errors. There is no current density loss when $\beta \leq 25$ with Δs = 0.2 μm. Since the losses of current size and current density in both cases are negligible to exert significant impact on the results when β = 25, it can be supposed that the simulations with the pre-defined current density and the pre-defined current size have similar current setting when β = 25. The maximum local temperature and macro interface temperature are taken to do comparison with the pre-defined current density case when β = 25 in Figures 3.33 and 3.34. The differences in maximum localized temperature and macro interface temperature between two cases are 37 °C and 3 °C, respectively. These temperature differences can be neglected for metals with high melting points and recrystallization temperatures, such as aluminum. Results show that maximum local temperature and macro interface temperature of Surface Pair Set 1 are about 600 °C and 80 °C, respectively, during the process. The results of high local temperature also prove that recrystallization and melting can be found locally at the interface. However, the hot spot area is

not necessarily large according to Figure 3.25. Consequently, the hot spot temperatures are not reflected by the macro interface temperature.

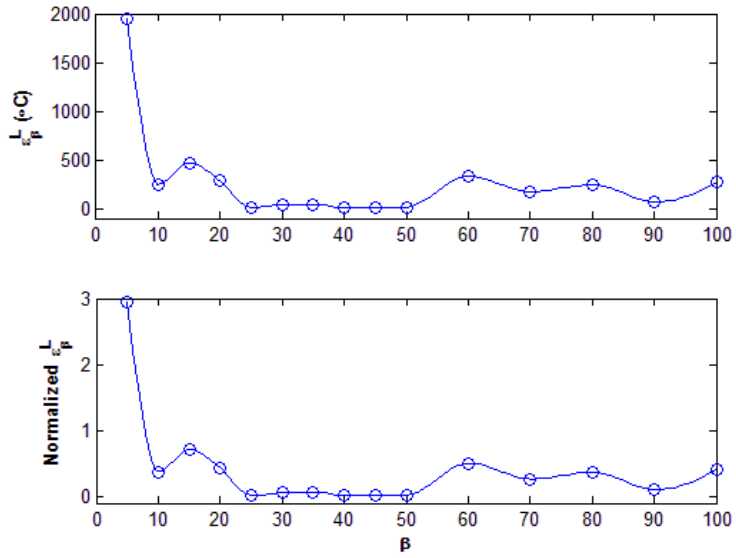

Figure 3.28 Absolute and normalized ε_β^L given by different β simulated with pre-defined current size

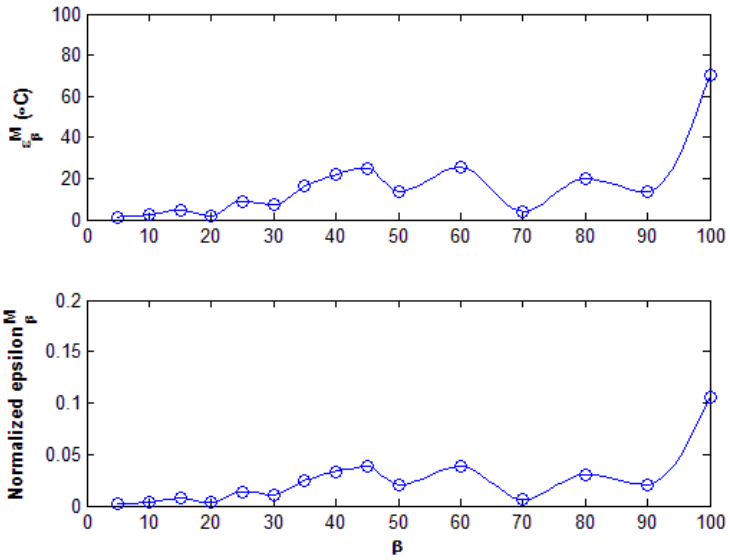

Figure 3.29 Absolute and normalized ε_β^M given by different β simulated with pre-defined current size

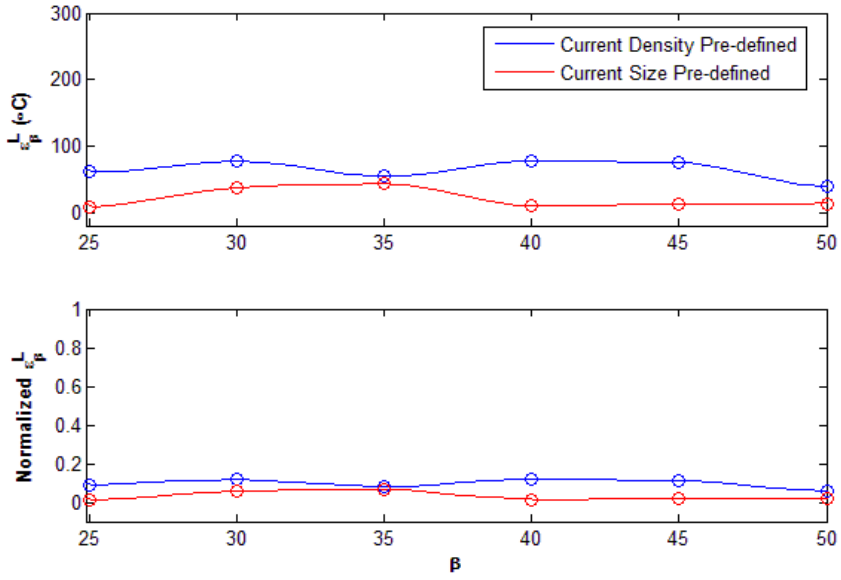

Figure 3.30 Comparison on absolute and normalized ε_{β}^{L} obtained from simulations with pre-defined current size and current density

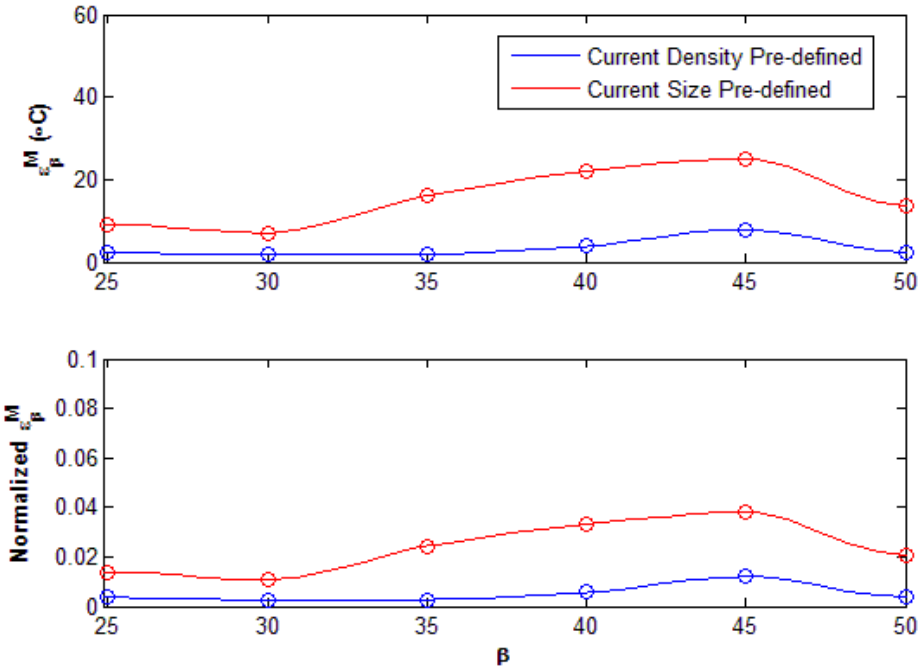

Figure 3.31 Comparison on absolute and normalized ε_{β}^{M} obtained from simulations with the pre-defined current size and current density

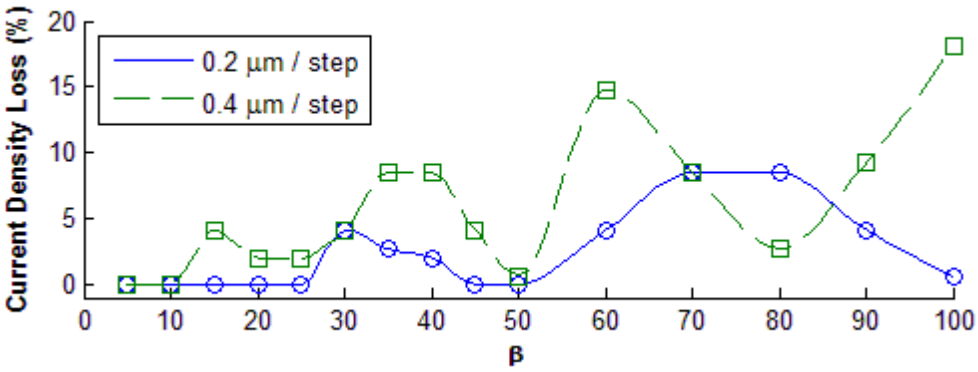

Figure 3.32 Percentage of numerical current density loss with different β simulated with the pre-defined current size

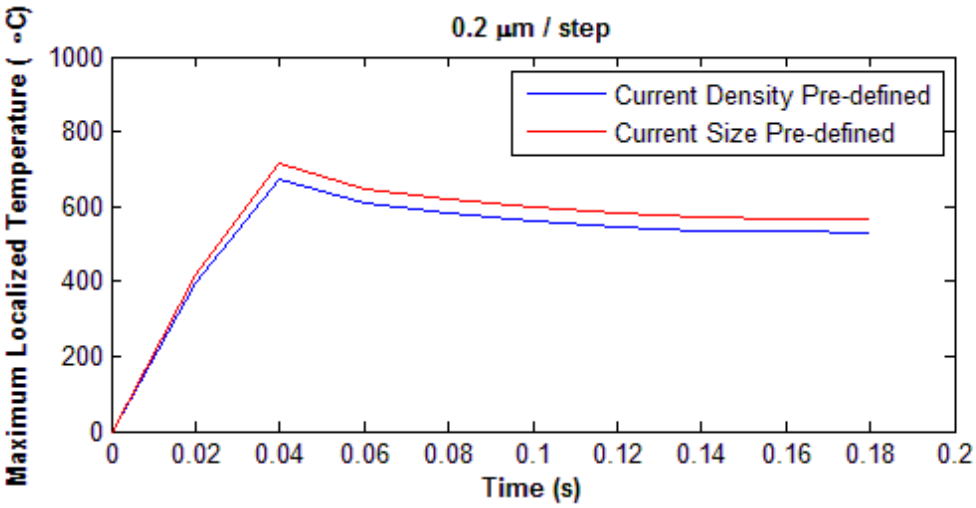

Figure 3.33 Comparison of maximum localized temperature histories simulated with the pre-defined current density and pre-defined current size when $\beta = 25$

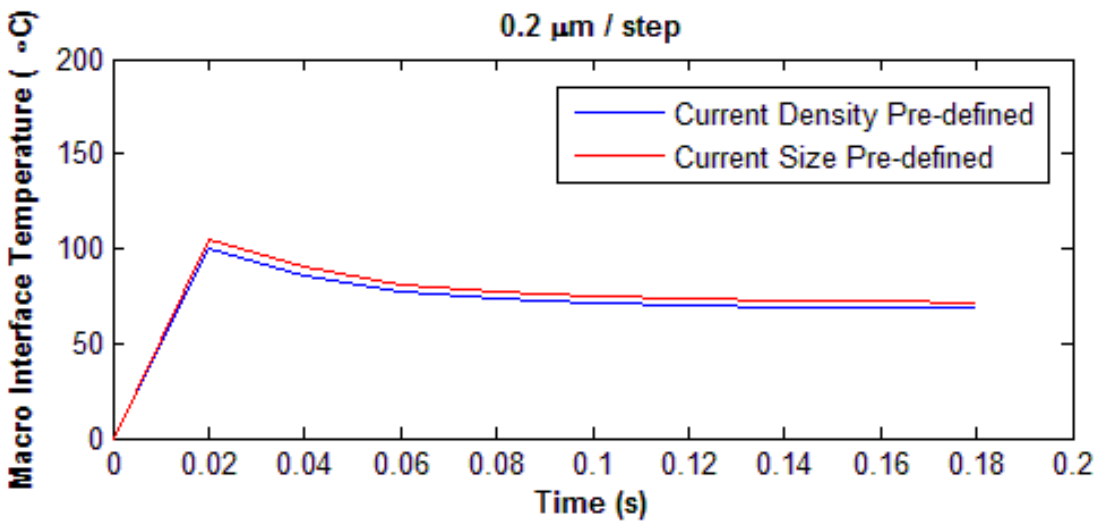

Figure 3.34 Comparison of macro interface temperature histories simulated with the pre-defined current density and pre-defined current size when $\beta = 25$

3. Nanostructure due to Joule Heating

Some reports have revealed that nanostructures would be produced by performing roll bonding repeatedly, which is called accumulative roll bonding (ARB) [137,151,174–176]. Those nanostructures are produced by severe plastic deformation by ARB. In our study, only single-pass roll bonding was performed for Al/Cu sheet production. Only one pass of rolling is not sufficient to perform severe plastic deformation and produce nanostructure. Additionally, ARB proves nanostructure in the entire rolled sheets. However, there were only a few spots found with nanostructures in our single-pass EARB produced Al/Cu sheets. Meanwhile, our simulation results show that only a small percentage of area has local interface temperature above the recrystallization temperature and melting point of the material (Figure 3.25). Therefore, it is highly possible that the nanostructures were produced due to high local interface temperature.

3.6 Conclusion

A model has been developed to simulate the Joule heating effect at the metal-metal interface for local and macro interface temperature predictions. The model successfully estimates the local interface temperature (Figures 3.22 and 3.32) which is not necessarily reflected by the macro interface temperature calculation (Figure 3.33). The local temperature is highly dependent on the interface surface topography (Figure3.25 and Table 3.2). Simulation shows that it is possible to reach the melting point and recrystallization temperature of aluminum locally at the interface of an Al/Cu sheet. Previous experimental microstructure observation gave evidence to support the results. This model can be applied in any interface involve Joule heating when the current passes across interface, not only limiting to electrically-assisted roll bonding.

Chapter 4

Electrically-assisted Microrolling-based Texturing

In this chapter, investigations specifically focus on the surface texturing performed by microrolling. This chapter investigates the efficacy of the electrically-assisted microrolling-based texturing (EAμRT) on aluminum alloy (AA3003-H14) and titanium alloy (Ti-6Al-4V). Based on the experimental results, an analytical model is developed to quantify the current effect in the EAμRT process. Additionally, a capacitive embedded pressure sensor is developed to investigate the pressure distribution in the workpiece width direction.

4.1 Literature Review

Reviews on the electrically-assisted manufacturing (EAM) and surface texturing technology were discussed in Chapter 1. Considering the production rate and energy input, the forming-based texturing method enables surface texture fabrication with a relatively higher yield rate and less energy consumption. Among different types of forming processes, rolling is a forming process that is suitable for the production of planar parts with a large surface area and an infinite length. By integrating texturing process to rolling, texturing over a large surface area in high production rate can be achieved. Texturing with a rotating roll allows continuous imprinting of textures on a surface. Hirt et al. used a roll wounded with wires to imprint riblets on aluminum surfaces, as shown in Figure 4.1 [177]. Riblets with a minimum spacing of 100 μm and height of 33 μm were produced on a 1-2 mm thick Al99.7 sheet with a roll wounded with wire. The riblet

dimension could be modified depending on the diameter of the wire. The uniformity of the riblet was maintained by using force data for calibration between simulations and experiments. Zhou et al. utilized a pre-textured tungsten carbide roll to perform rolling-based texturing[178]. The roll was pre-textured by wire EDM. The channel density and depth could be improved by multi-pass rolling, i.e., repeated rolling on the same surface[179]. Multi-pass rolling was also used to produce grid and rhombus patterns on a previous-pass-textured workpiece with a planar rotation, as shown in Fig, 4.2[179]. Both the studies reported by Hirt and Zhou demonstrated texturing of metal surfaces by (micro)rolling-based texturing. However, the texturing materials in both studies were soft materials, such as aluminum. Texturing of hard materials, such as titanium, can be challenging, especially on a meso/micro-scale level. Heating to soften workpiece materials before forming is a conventional practice adopted by the industry. The heating process is usually done with furnaces. However, the heating time can be a few hours long, and the temperature required is high in order to compensate for the heat loss during workpiece transportation from the furnace to the forming machine. To overcome the limitations in the conventional furnace heating, heating with electric current can be applied. The passage of electric current in a conductive material generates the Joule heating effect. Depending on the material properties and current density, both the heating time and temperature rise vary. However, compared to the furnace heating, Joule heating is able to heat up materials within a few minutes or even a few seconds. Mai et al. utilized electrically-assisted embossing to texture micro-channels on 316L stainless steel plates, as shown in Figure 4.3[111]. A 10 *mm* by 10 *mm* die with different texture dimensions was employed for texturing. Electric currents with densities of 5 A/mm^2 and 10 A/mm^2 were set flowing through the workpiece during the embossing process. The channel width and spacing produced depended on the texture of the die. The produced channel depth was

determined by the die press. The maximum and minimum channel depths produced were 482 μm and 16 μm, respectively. Oh et al. textured stainless steel (SUS304) and titanium using electrically-assisted indentation[180]. Electric current was applied near the indentation region as shown in Figure 4.4. It gave a localized heating on the workpiece surface for the hardness reduction so that the tool could be indented deeper to the workpiece. Squares/diamonds of a 2 mm × 2 mm size were imprinted on both SUS304 and titanium. The texture depths were in the ranges between 55 μm and 62 μm for SUS304, and between 63 μm and 67 μm for titanium. By the utilization of electric current, both Mai and Oh formed textures on hard materials, such as stainless steel and titanium. However, both forming processes have the limitation on the texturing over a large surface area. By taking the advantages of microrolling-based texturing and electrically-assisted forming, two processes are merged into the electrically-assisted microrolling-based texturing (EAμRT) for the texturing on hard materials. In this chapter, EAμRT is performed for texturing on aluminum and titanium surfaces. The imprinted texture depth, groove/channel depth in this case, is measured for process investigation and analytical modeling in this chapter as well.

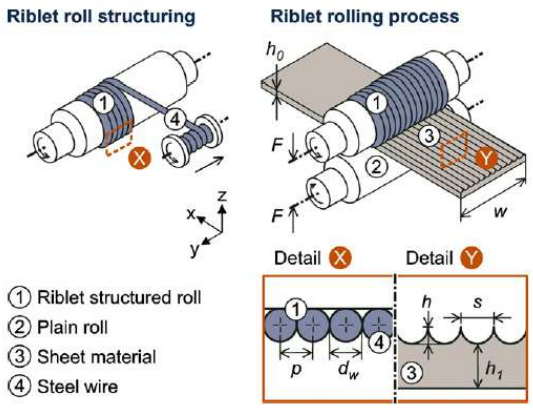

Figure 4.1 Riblet roll structuring and rolling process[177]

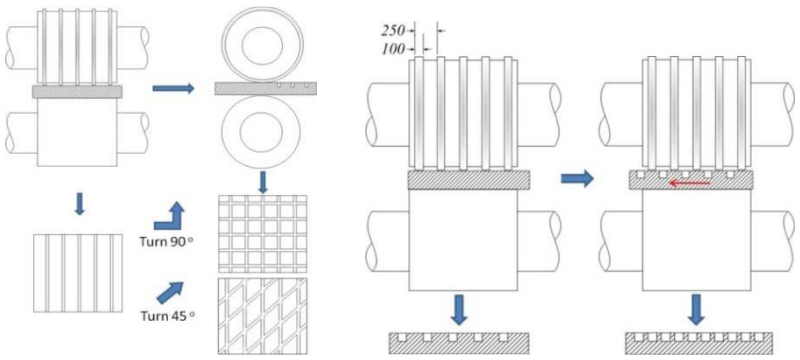

(a) (b)

Figure 4.2 (a) Two-pass surface texturing by shifting sheet, (b) grid and rhombus patterns textured by multi-pass texturing[179]

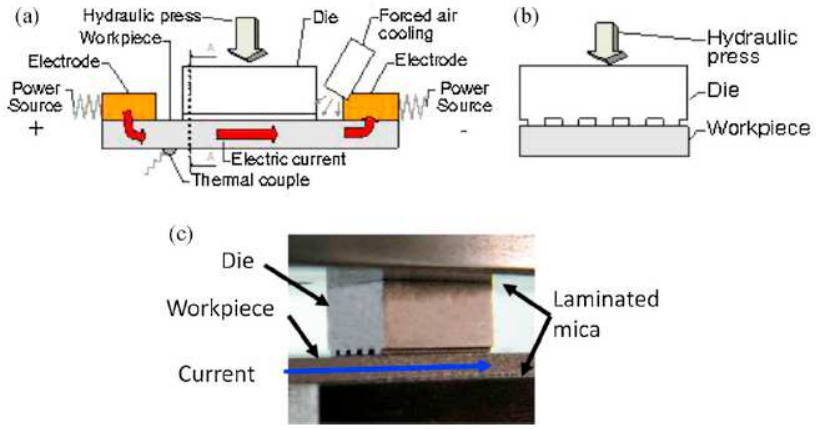

Figure 4.3 Schematic structure of embossing system: (a) front view, (b) side view, (c) experimental step[111]

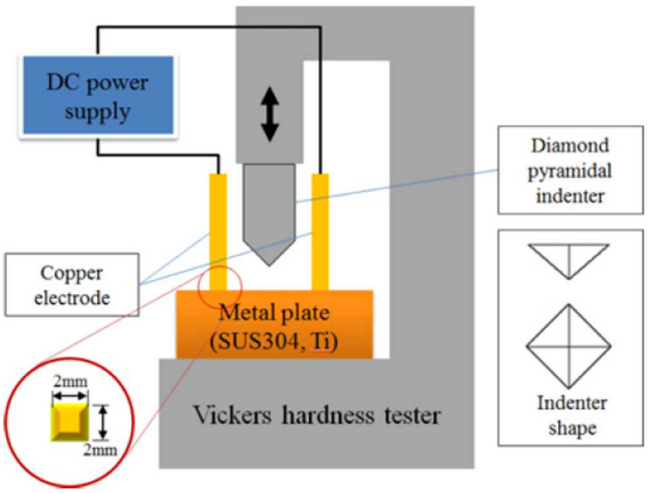

Figure 4.4 Schematic of electrically-assisted indentation[180]

4.2 Electrically-assisted Microrolling-based Texturing on Aluminum Alloy and Titanium Alloy

Conventional microrolling-based texturing has been advanced by introducing electric current acted as a means to offer rapid and localized softening effect on material easing texture imprinting. The advanced process is termed as electrically-assisted microrolling-based texturing (EAμRT). The effectiveness of EAμRT on aluminum alloy and titanium alloy is discussed.

1. Experimental Setup and Texture Depth Measurements

Both microrolling-based texturing (μRT) and electrically-assisted microrolling-based texturing (EAμRT) were performed with the desktop microrolling mill mentioned in Chapter 2. In conventional sheet rolling, a pair of smooth rolls was employed to perform deformation on sheet metals. For microrolling-based texturing, one of the rolls is replaced by a roll with textures pre-printed on its surface. In this study, a pre-textured roll with a diameter of 27.58 mm was fabricated with micro-grooves by wire EDM. In order to afford high local pressure at the texture tips during the process, it was made by tungsten carbide. There were three sections of textures

with different dimensions on the pre-textured roll, as shown in Figure 4.5(a). Each section was 10 mm width and separated by a 3 mm wide smooth region. The dimensions of textures on those sections were tabulated in Table 2.1. A profile of textures in the middle section was shown in Figure 4.5(b) as an example. Note that the dimensions in the table were measured when the pre-textured roll was completely new. Wearing out of the roll causes the change of texture dimensions.

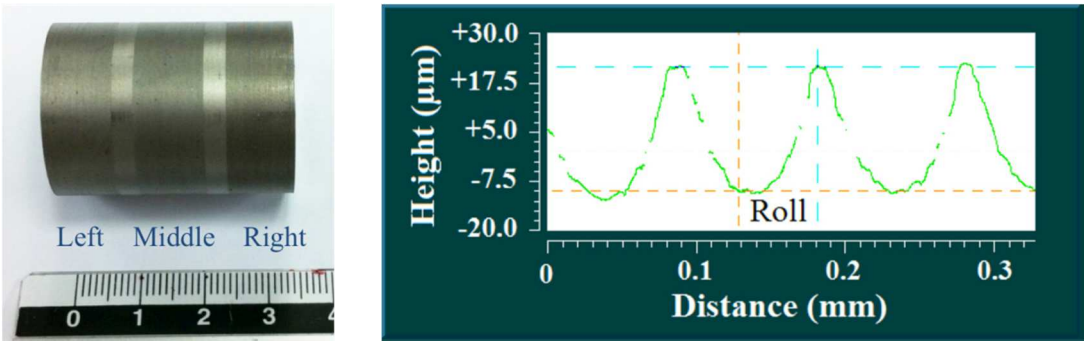

(a) (b)

Figure 4.5 (a) A pre-textured roll; (b) Tooth profile in the middle section of the pre-textured roll

In this study, the middle section was employed in order to prevent tilting of rolls due to the unbalanced force at the roll ends. The tilting of rolls may not be an effective impact in the macro-scale; however, it could be a disaster in micro-scaled texturing since its fabricated textures are only about few micrometers. Due to the imperfectness of the rolls, their circumferences are varying in micro level. Although the variation is insignificant in macro-scale, it is enough to create a significant periodic variation on texture depth. To minimize the impact from rolls, rolling always starts at the same roll location and comparison on texture depths of textured workpieces was made at the same location as well. For EAμRT, constant DC current with the

size of 100A was applied. An embedded capacitive pressure sensor was used for the rolling pressure measurement.

0.4 mm thick aluminum alloy (AA3003-H14) and titanium alloy (Ti-6Al-4V) stripes were textured. Their material properties are tabled in Table 4.1. After texturing, the depths of imprinted channels were measured with an optical 3D micro coordinate system, *Alicona InfiniteFocus*, with a vertical resolution of 10 nm.

Table 4.1 Material properties of AA3003-H14 and Ti-6Al-4V

	AA3003-H14	Ti-6Al-4V
Density (g/cm^3)	2.73	4.43
Young's modulus (GPa)	70	113.8
Electrical resistivity (Ω-cm)	3.4×10^{-6}	1.78×10^{-4}
Specific heat capacity (J/g-°C)	8.93×10^{-4}	5.26×10^{-1}
Linear thermal expansion coefficient (μm/m-°C)	21.5 @ 20°C 24.9 @ 250°C --	8.6 @ 20°C 9.2 @ 250°C 9.7 @ 500°C

2. Results and Discussions

In the imprinting of channels, deeper channels require larger forming force because of the strain hardening increasing the deformation force, i.e., the flow stress. In the microrolling-based texturing, the depth of a channel depends on the forming pressure at its corresponding position. Figure 4.6 shows the normalized channel depths along the AA3003-H14 workpiece width and its corresponding pressure distribution obtained by the 1st generation of the embedded capacitive pressure sensor during μRT. Because the tooth heights are different in different roll texture sections, the measured channel depths are normalized by their corresponding tooth heights, as listed in Table 2.1 for comparison. The "Gap" is referred to the machine setting and does not equal the actual roll gap. The actual roll gap is smaller than the set roll gap because there is roll

displacement due to inherent component and machine stiffness issues, such as, the elastic deformation of components and component-to-component clearances. The channels at the middle section have the deepest channel on the textured sheet. This indicates that the forming force in this region should be the highest among all three sections and which is proved by the observance of pressure peak at the middle region of the texturing zone. The rolling force concentrated at the center of the roll during the rolling process. Note that the middle section has the shortest tooth height among all sections (Table 2.1), however, it gave the highest pressure at this region. The high pressure at this section is due to the constraints of the neighboring materials. Furthermore, the pressure distribution is not symmetric; the rolling forces are different between the left and right sections. The differences are also reflected by the channel depths at these two sections. The difference in rolling pressure was caused by the tooth height. Furthermore, a smaller roll gap gave a higher compression for imprinting deeper channels resulting in pressure increment.

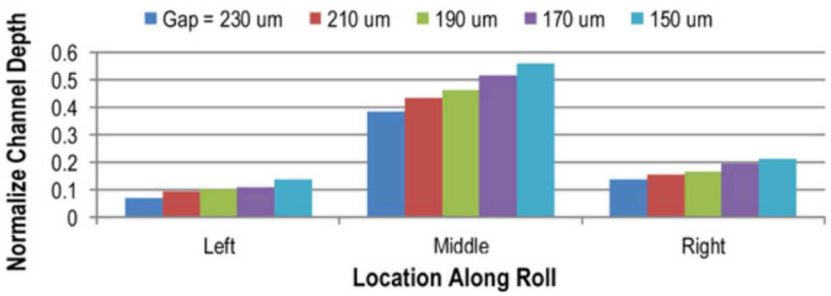

(a)

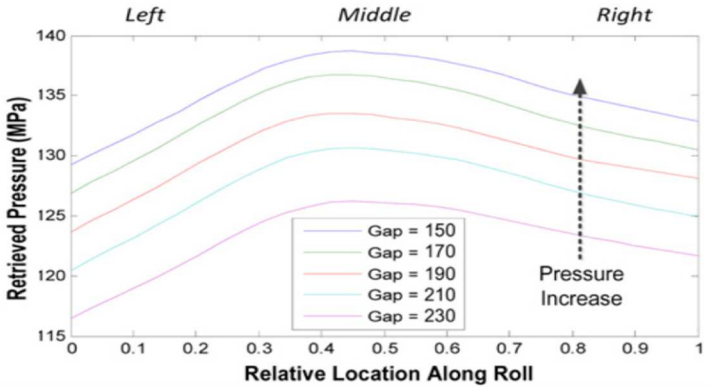

(b)

Figure 4.6 (a) Normalized channel depth, and (b) pressure distribution measured by the 1st generation embedded capacitive pressure sensor during μRT

In order to investigate the effect of Joule heating on the forming pressure, pressure distributions during μRT and EAμRT of AA3003-H14 and their produced channel depths are compared in Figure 4.7. Instead of the entire three texture sections, only the pressure at the middle section was measured with the 2nd generation embedded sensor. Similar trends of pressure distributions were found between μRT and EAμRT: the center of the workpiece gave the highest pressure. Moreover, EAμRT produced deeper channels but with lower rolling pressure compared to μRT. The decrease of rolling pressure in EAμRT provides evidence that the Joule heating effect induced by current passage softens material, resulting in easier texturing for deeper channels. The results prove that EAμRT outperforms μRT in terms of rolling pressure and produced channel depth.

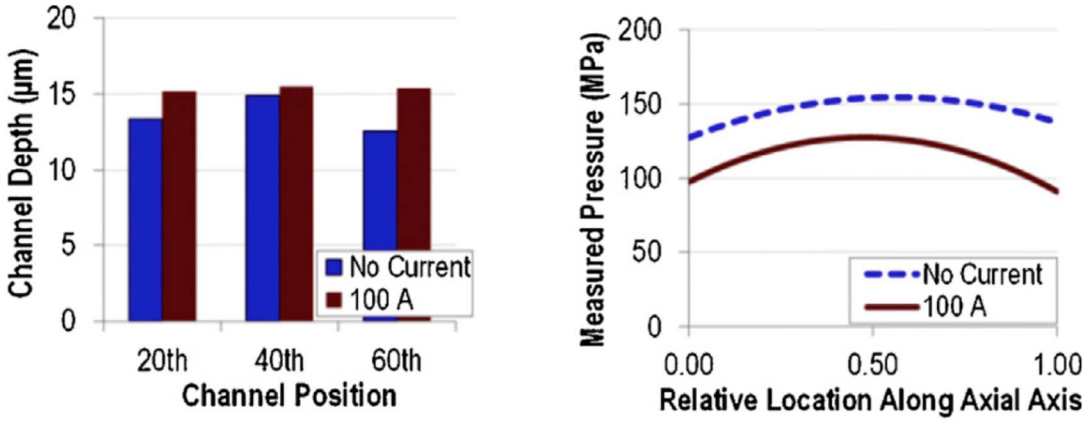

Figure 4.7 (a) Measured channel depths, and (b) their corresponding pressure distribution done by μRT and EAμRT

Comparison on the channel depths textured on AA3003-H14 and Ti-6Al-4V by μRT and EAμRT and their images are shown in Figures 4.8 and 4.9, respectively. The measured channel depths are shown in Figure 4.10(a). In Figure 4.10(b), the forces were measured with loadcells at the locations where channel depths were measured. Note that the wore-out pre-textured roll gave non-uniform channel dimensions, particularly at the tooth tips; therefore, the comparisons shown in both Figs 4.10(a) and 4.10(b) are made with their corresponding channels. As can be seen in Figure 4.9, although the widths of channels are not uniform, a same channel width variation trend between Figure 4.9(a) and 4.9(b) can be observed. For example, the 3rd channels are particularly thinner and the 4th channels are significantly wider in both figures. Because the ease of texturing on AA3003-H14, deeper channels were produced, which were less impacted by the worn-out tooth tips of the pre-textured roll, the width of channels are rather similar.

In Figure 4.10, because of the relatively lower Young's modulus of AA3003-H14 compared to Ti-6Al-4V, deeper channels were produced, even without the assistance of electric current. Continuous channels can be clearly seen in Figure 4.8. Channels with depth larger than 10 μm

can be produced by both μRT and EAμRT. On the contrary, the higher strength of Ti-6Al-4V demotes the ease of imprinting channels resulting in generally shallow channel depths, which are only about 1 to 5 μm, as can be seen in Figure 4.9(b). Because very fine channels were produced in Ti-6Al-4V, the grain size of the material was measured to ensure that it is incomparable to the tooth size. Micrographs of the cross-section in the workpiece thickness direction were taken to measure the grain size. It was found that grains are relatively isotropic in this plane as shown in Figure 4.11. The measured mean grain size is 2.39 μm with a standard deviation of 0.46 μm. As seen from the figure, there are multiple grains along the feature, meaning that the size-effect can be neglected here.

Although it is hard to imprint channels on Ti-6Al-4V, significant improvement can be noticed in EAμRT. There is about 2 to 3 μm deeper in the channel produced with EAμRT than those with μRT. It is approximately 200% increase in produced channel depth in Ti-6Al-4V brought by EAμRT. On the other hand, there is only 15% channel depth improvement in EAμRT of AA3003-H14. The significant difference in the result can be explained by the effect of material electrical resistivity on the Joule heating effect. The joule heating is a function of material electrical resistivity. The electrical resistivity of Ti-6Al-4V is 50 times larger than AA3003-H14. Consequently, the significant Joule heating effect in Ti-6Al-4V during EAμRT softened the material to ease deformation. The improvement is noticeable in Figure 4.9. Ti-6Al-4V is too strong to be imprinted by μRT resulting in some of the areas could not be imprinted and led to discontinuities of channels. The Joule heating effect softened Ti-6Al-4V to enhance texture imprinting. Therefore, continuous channel can be observed in Figure 4.9(b).

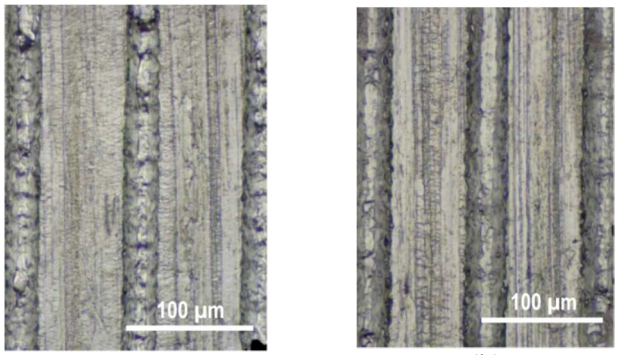

(a) (b)

Figure 4.8 Images of channels produced on AA3003-H14 by (a) microrolling-based texturing, and (b) electrically-assisted microrolling-based texturing with 100A DC

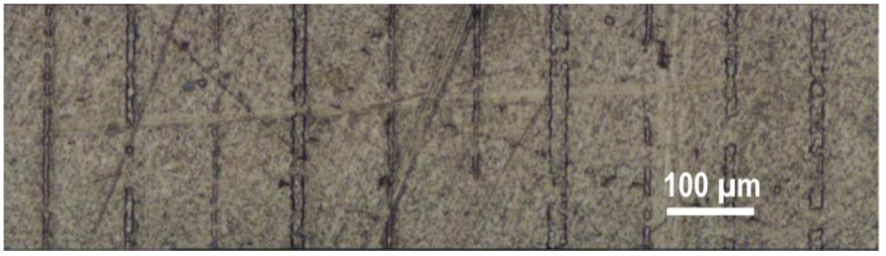

(a)

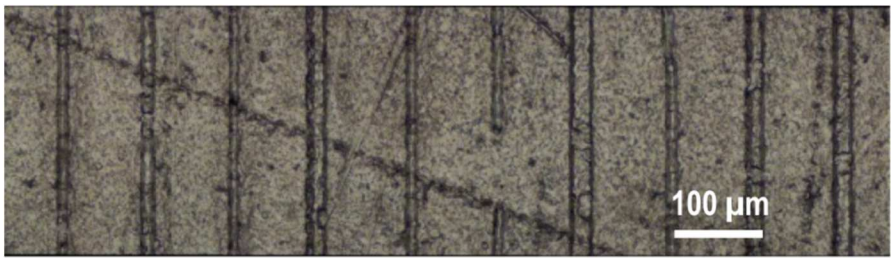

(b)

Figure 4.9 Images of channels produced on Ti-6Al-4V by (a) microrolling-based texturing, and (b) electrically-assisted microrolling-based texturing with 100A DC

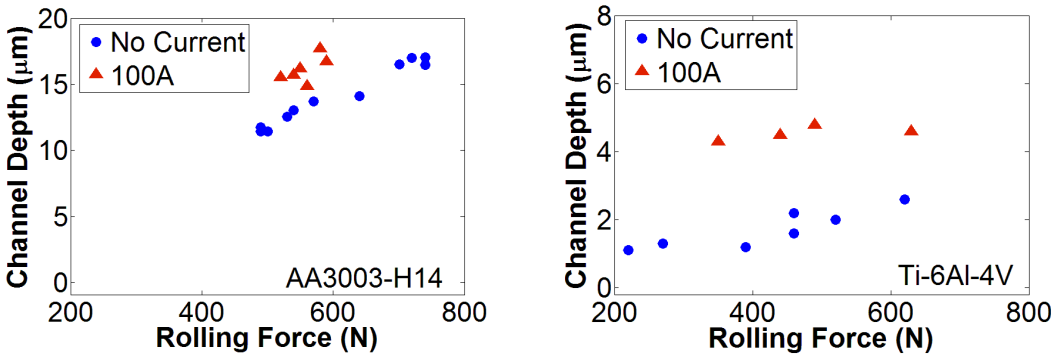

(a) (b)

Figure 4.10 Measured depths of channels produced on (a) AA3003-H14 and (b) Ti-6Al-4V with microrolling-based texturing, and (b) electrically-assisted microrolling-based texturing with 100A DC

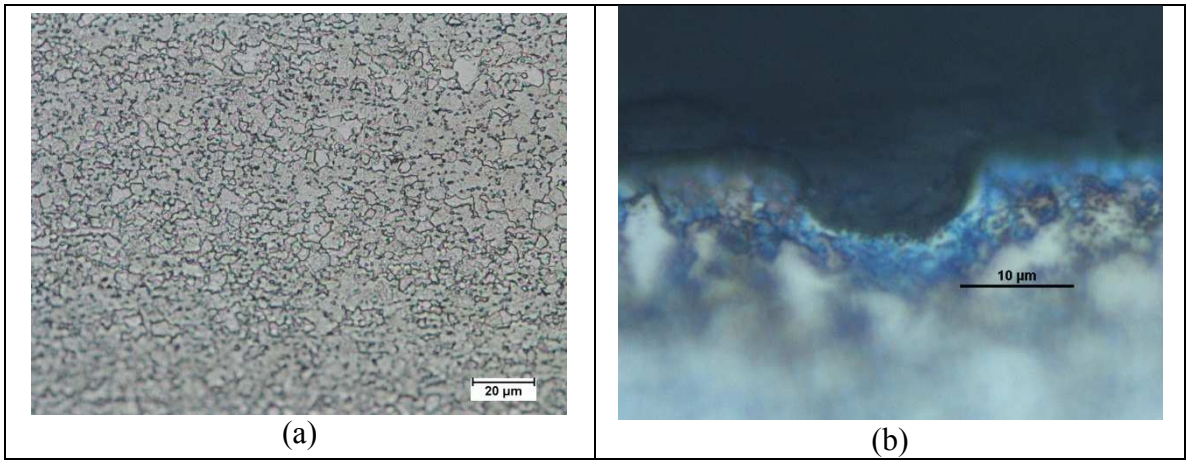

(a) (b)

Figure 4.11 (a) Grains of initial Ti-6Al-4V, and (b) grains near a textured channel

3. Conclusions

In summary, according to the presented experimental results, EAμRT improves the texturing efficacy with the benefits brought by the Joule heating effect induced by electric current passage. The material softening effect resulted by the Joule heating deepened the channels while reducing the forming pressure. More significant improvement can be achieved with materials having

higher electrical resistivities. For example, the higher electrical resistivity of titanium alloy (Ti-6Al-4V) gives a more impressive Joule heating effect than aluminum.

4.3 Analytical Modeling of Electrically-assisted Microrolling-based Texturing for Texture Depth Prediction

An experimental investigation has been discussed in the previous section. To quantify the effect of the electric current on channel imprinting in EAμRT and provide guidance for a better control of the process, an analytical model has been developed and performed for EAμRT produced channel depth prediction. Besides the Joule heating effect, the impact exerted by the non-uniform tooth geometry of a worn-out pre-texture roll is also taken into account. Because of the effectiveness of Ti-6Al-4V in EAμRT, Ti-6Al-4V was chosen as the demonstration material for modeling.

1. Model Construction

This model predicts the produced channel depth under the effect of Joule heating, which is induced by the passage of electric current in the workpiece material. Electric current is flowing in the workpiece sheet thickness direction, i.e. from a roll to the other across the workpiece. The deformation of workpiece is assumed in a plane strain condition and its elastic recovery is neglected. Material properties and the roll force are the input parameters in this model for channel depth prediction in EAμRT.

Swift's hardening law, as descripted in Eqn. 4.1, is applied to model the hardening behavior of material.

$$\sigma_T = K_T\left(\varepsilon_0 + \varepsilon_p\right)^{n_T} \qquad \text{(Eqn. 4.1)}$$

where T is the temperature. σ_T is the stress of a material under a process temperature of T. ε_0 and ε_p are the material constant and plastic strain, respectively. K_T and n_T are the temperature-dependent strength coefficient and strain hardening exponent at a temperature of T, respectively. In this rolling process, ε_p in Eqn. 4.1 can be expressed as:

$$\varepsilon_p = \ln\left(\frac{1-y}{h_0}\right) \qquad \text{(Eqn. 4.2)}$$

with y and h_0 are the channel depth and the original workpiece thickness, respectively.

The total contact area between the pre-textured roll and the workpiece is a very important piece in the model. Besides finding the material stress with applied rolling forces, it is critical to estimate the current density with an applied current. The total roll-workpiece contact area A is defined by the total number of imprinted channel N, the roll radius R and channel depth y and width w as in Eqn. 4.3. The illustration is shown in Figure 4.12.

$$A = NRw \cdot \cos^{-1}\left(1 - \frac{y}{R}\right) \qquad \text{(Eqn. 4.3)}$$

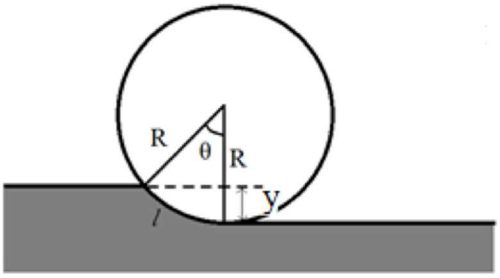

Figure 4.12 Illustration of roll-workpiece contact

Combining Eqns. 4.1 to 4.3, Eqn. 4.1 can be rewritten as Eqn. 4.4:

$$K_T\left(\varepsilon_0 + \ln\left(\frac{1-y}{h_0}\right)\right)^{n_T} = \frac{F}{NRw\cdot\cos^{-1}\left(1-\frac{y}{R}\right)} \qquad \text{(Eqn. 4.4)}$$

Because the elastic recovery is neglected, the produced channel depth and width are equal to the contact depth and width, respectively. Both the contact depth and width depend on the tooth

profile, which can be measured experimentally. Eqn. 4.5 described the contact width in terms of contact depth according to a tooth profile which measured when the pre-textured roll was completely new, i.e. without wearing.

$$w = 2.779 \times 10^{3} y^{2} - 9.019 \times 10 y^{2} + 2.099 y + 4.838 \times 10^{-3} \quad \text{(Eqn. 4.5)}$$

Both w and y are in mm. To be consistent, the roll radius R in Eqn. 4.4 is also in mm. The expression in Eqn. 4.5 is particularly for the pre-textured roll used in this study. Alteration of the equation depends on the tooth geometry being used. With Eqn. 4.5, contact area A can be obtained. Note the Eqn. 4.5 is based on an assumption that all the teeth have the same profile, i.e. all N channels have the same dimensions. However, the wear of the pre-textured roll causes the teeth on it to no longer have the same profile. Therefore, actual contact area A^* is different from the ideal contact area A found basing on Eqn. 4.5. The teeth on a worn pre-textured roll have non-uniform dimensions, and it is very challenging to measure all the teeth for their profiles. Therefore, a correction factor β is introduced to correct the total contact area. More detail on β will be given in the "Results and Discussions" section.

K_T and n_T in Eqn. 4.4 are temperature-dependent, therefore, they can be expressed as a function of temperature. Based on the experimental results reported by Vanderhasten et al.[181], temperature-dependent K_T and n_T of Ti-6Al-4V can be expressed as Eqns. 4.6 and 4.7.

$$K_T = 1.678 \times 10^{-6} T^{3} - 3.644 \times 10^{-3} T^{2} - 3.586 \times 10^{-1} T + 1678 \quad \text{(Eqn. 4.6)}$$

$$n_T = -3.627 \times 10^{-7} T^{2} + 1.611 \times 10^{-4} T + 6.022 \times 10^{-2} \quad \text{(Eqn. 4.7)}$$

with K_T and T in MPa and °C, respectively.

In order to verify that Eqns. 4.6 and 4.7 are able to successfully model the true stress-strain relation of Ti-6Al-4V under different temperature, true stress-strain curves generated with K_T and n_T at different temperatures are compared with experiments reported by Vanderhasten et

al[181]. The comparison is shown in Figure 4.13. Results show that there are good agreements between the material models and experiments within the strain range of interest to this study.

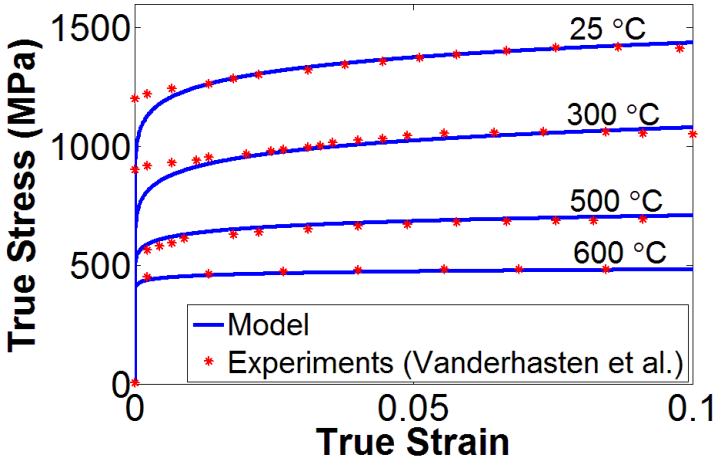

Figure 4.13 Ti-6Al-4V true stress-strain curves at different temperatures

In this study, the strain rate was on the order of 10^{-2}, corresponding to the rolling speed employed, and the temperature was less than 700°C (~1000 K). According to the Figure 4.14, which shows the strain rate sensitivity exponent of Ti-6Al-4V under different strain rates and deformation temperatures reported by Lou et al[182], the temperature dependency of strain rate sensitivity under the processing conditions in this study can be neglected.

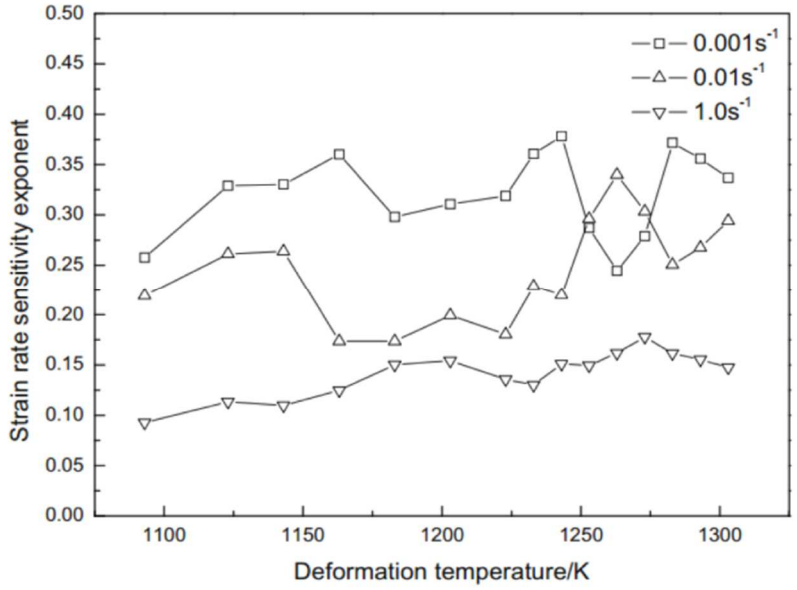

Figure 4.14 Strain rate sensitivity exponent of Ti-6Al-4V under different strain rates and deformation temperatures[182]

In EAμRT, the electric current induced Joule heating effect contributes to the temperature rise:

$$T = T_{initial} + \Delta T_{Joule} \qquad \text{(Eqn. 4.8)}$$

The adiabatic temperature rise due to the Joule heating effect can be calculated by Eqn. 4.9.

$$\Delta T_{Joule} = \frac{\rho J^2 t_p}{cd} \qquad \text{(Eqn. 4.9)}$$

where J is the current density, t_p is the current duration, and ρ, c and d are electrical resistivity, specific heat capacity and density of material, respectively. The heating time t_p in this study is defined as the roll-workpiece contact time depending on the contact geometry and rolling speed. Eqn. 4.10 defined t_p in terms of the roll geometry, channel depth and rolling speed.

$$t_p = \frac{\cos^{-1}\left(1-\frac{y}{R}\right)}{\omega} \qquad \text{(Eqn. 4.10)}$$

where ω is the angular velocity of the roll in rad/s.

With the contact area defined by Eqn. 4.3, current density can be obtained by Eqn. 4.11.

$$J = \frac{I}{A} \qquad \text{(Eqn. 4.11a)}$$

$$J = \frac{I}{NRw \cdot \cos^{-1}\left(1-\frac{y}{R}\right)} \qquad \text{(Eqn. 4.11b)}$$

where I is the current size.

Combining Eqns. 4.9 to 4.11, the adiabatic Joule heating temperature rise can be obtained as:

$$\Delta T_{Joule} = \frac{\rho I^2}{cd\omega N^2 R^2 w^2 \cos^{-1}\left(1-\frac{y}{R}\right)} \qquad \text{(Eqn. 4.12)}$$

After knowing the Joule heating temperature rise by Eqn. 4.12, the deformation temperature can be obtained by Eqn. 4.8. Then, the material strength coefficient K_T and strain hardening exponent n_T can be found by Eqns. 4.6 and 4.7, respectively. Finally, the relationship between the force and channel depth can be found by solving Eqn. 4.4 numerically.

2. Results and Discussion

As the deformation temperature is highly dependent on the current density in which the knowledge of the actual contact area is important. The contact area in Eqn. 4.3 is found based on the tooth profile as expressed in Eqn. 4.5, which is based on a pre-texture roll without wear. However, after various uses of the pre-textured roll, a wide range of tooth widths was observed, as represented by the shaded region in Figure 4.15. Therefore, Eqn. 4.5 is no longer enough for finding an actual width.

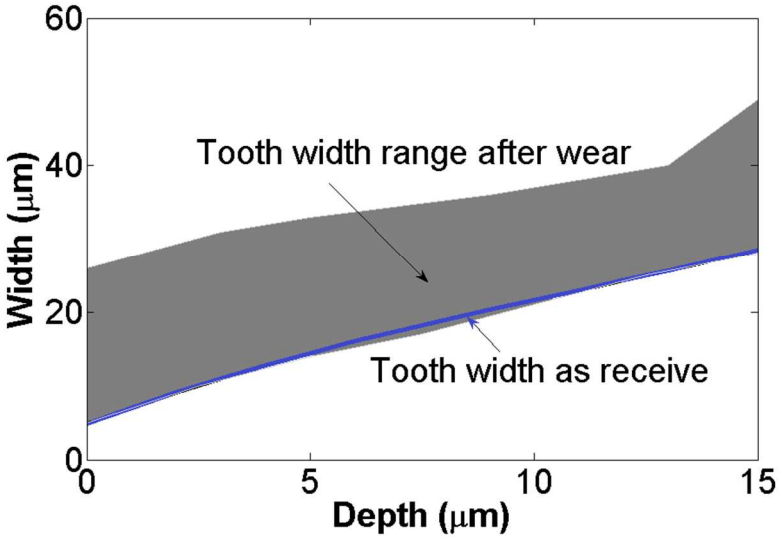

Figure 4.15 Measured tooth depth and width relationships of the pre-textured roll before and after wear

It is known that the wear of the pre-textured roll affects the actual contact area, therefore, a correction factor α is used to correct the contact area from the ideal contact area found by Eqn. 4.3. The relation between the actual contact area $A^*$and the ideal contact area A is expressed as Eqn. 4.13.

$$A^* = \alpha A \qquad \text{(Eqn. 4.13)}$$

The α can be either a constant or a function of contact depth y. This correction factor is virtually essential for micro-scale forming, which is very sensitive to tooling variations and those variations cannot be caught easily.

With the correction factor β, Eqn. 4.4 becomes:

$$K_T\left(\varepsilon_0 + \ln\left(\frac{1-y}{h_0}\right)\right)^{n_T} = \frac{F}{\alpha NRw\cdot\cos^{-1}\left(1-\frac{y}{R}\right)} \qquad \text{(Eqn. 4.14)}$$

To obtain β, experimental rolling force and its corresponding produced channel depth relationship in conventional microrolling-based texturing (μRT) are required. The dots and the

dash lines in Figure 4.16 represent experimental data points and the analytical channel depth predictions using this model without area correction, i.e., $\alpha = 1$. Experimental rolling forces were from both the loadcells and the embedded sensor. Although the predicted trend follows the experimental results, the predictions do not give satisfactory alignments with the experiments. The errors in the predictions are due to the failure of obtaining an actual contact area. To correct the contact area, a α -map is required. An example of β-map is shown in Figure 4.17. Predictions of channel depth with different correction factors using Eqn. 4.14 are plotted in a α--map. As rolling force increases, contact area varies with deformation depth and leads to an increase of α as well. The flatten tooth tips, which is caused by wearing, increase the total contact area. As a result, the actual contact area is larger than the ideal contact area and obtained a α larger than 1. By using the α -map, α corresponding to depth can be obtained and represented as a function of depth. Equations 4.15a and 4.15b are the obtained β-functions for AA3003-H14 and Ti-6Al-4V, respectively.

$$\alpha = 4.7 \times 10^{3} y^{2} - 4.7 \times 10 y + 1.1 \qquad \text{(Eqn. 4.15a)}$$

$$\alpha = -4 \times 10^{-10} y^{2} + 2 \times 10^{2} y + 1.7 \qquad \text{(Eqn. 4.15a)}$$

Corrected channel widths were calculated with the obtained α -function. The calculated α -corrected channel widths are all within the range of tooth width variation in Figure 4.18. It demonstrates the validities of the α-functions to capture the actual tooth width-depth relation.

With the obtained α-functions, Eqn. 4.14 can be used to predict produced channel depth. The predictions with and without contact area corrections are compared in Figure 4.19. Results show that the α-corrected model delivers predictions with better coincidence with the experiments than the previous non α-corrected model. Additionally, the calculated α-corrected channel widths are

all within the range of tooth width variation in Figure 4.18. It also confirms the α-functions in Eqn. 4.15 sufficiently well to capture the differences between the actual and ideal contact areas.

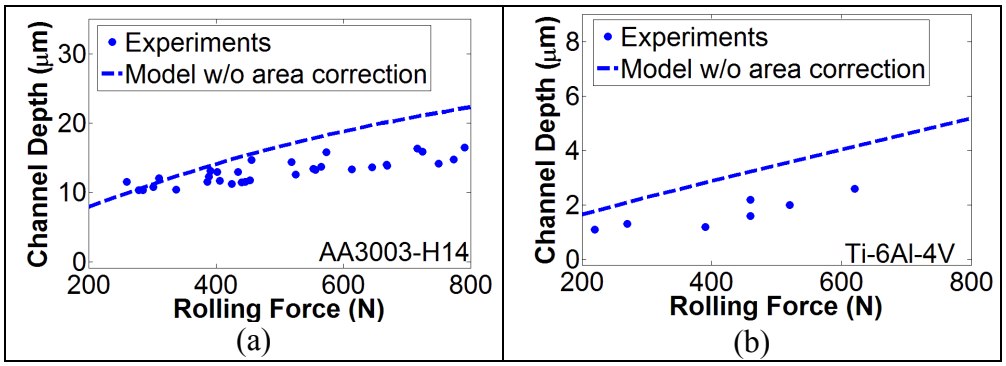

Figure 4.16 Channel depth predictions without contact area correction for conventional microrolling-based texturing of (a) AA3003-H14, and (b) Ti-6Al-4V

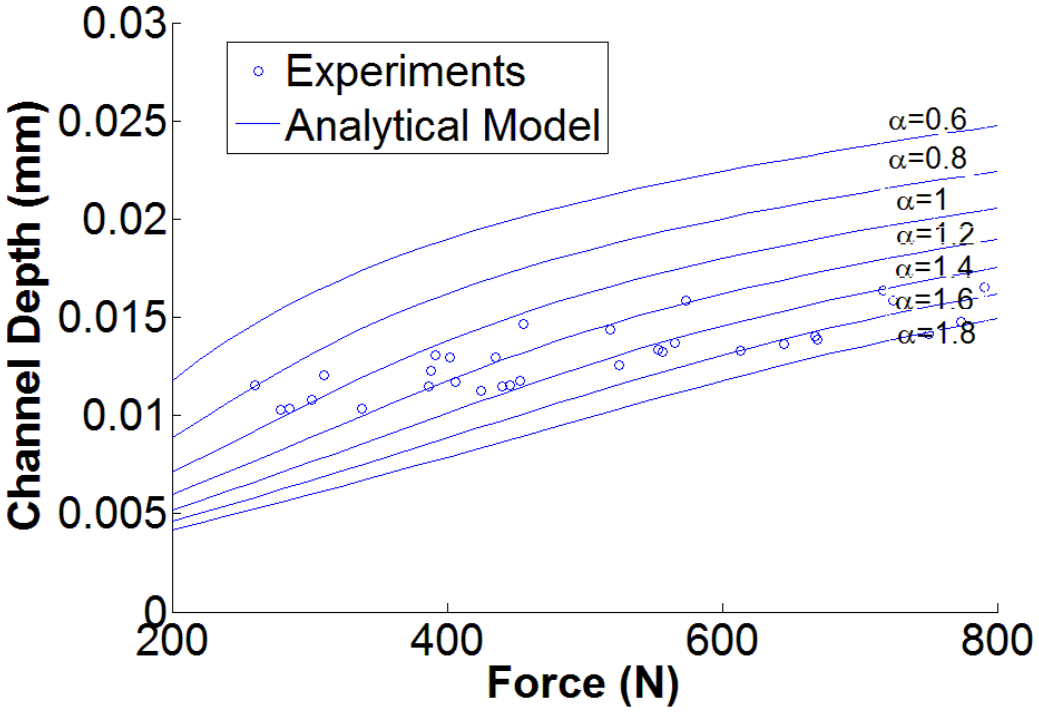

Figure 4.17 A α -map for finding a contact correction factor/function α

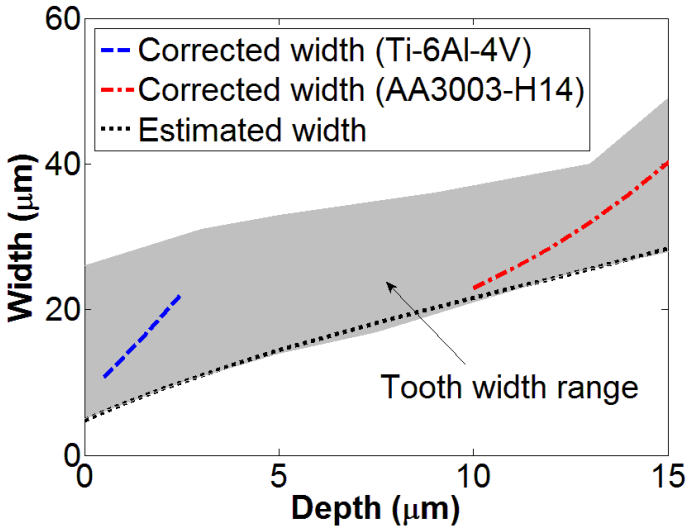

Figure 4.18 Calculated channel width corresponding to the channel depth

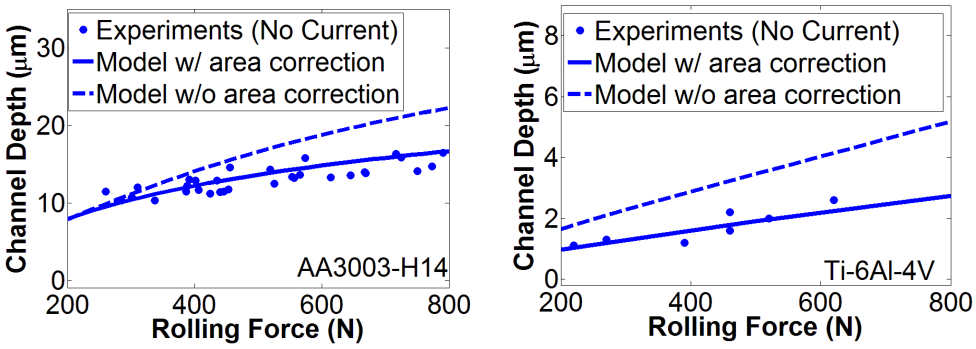

(a) (b)

Figure 4.19 Channel depth predictions with and without contact area corrections for conventional microrolling-based texturing of (a) AA3003-H14, and (b) Ti-6Al-4V

Experimental results from μRT served as a calibration for the actual contact area using a α-function. It is a very critical piece for channel depth prediction in EAμRT because the contact area plays an important role in temperature prediction in order to capture temperature-dependent material properties. With a valid β-function, Eqns. 4.10 to 4.12 become:

$$t_p = \frac{\alpha \cos^{-1}\left(1-\frac{\gamma}{R}\right)}{\omega} \qquad \text{(Eqn. 4.16)}$$

$$J = \frac{I}{A^*} = \frac{I}{\alpha A} \qquad \text{(Eqn. 4.17a)}$$

$$J = \frac{I}{\alpha NRw \cdot \cos^{-1}\left(1-\frac{y}{R}\right)} \qquad \text{(Eqn. 4.17b)}$$

$$\Delta T_{Joule} = \frac{\rho I^2}{\alpha c d \omega N^2 R^2 w^2 \cos^{-1}\left(1-\frac{y}{R}\right)} \qquad \text{(Eqn. 4.18)}$$

According to the experiments, a promising improvement in the texturing of Ti-6Al-4V by EAμRT can be achieved, therefore, Ti-6Al-4V is selected as the demonstration material for the depth prediction in EAμRT. Modeling of texturing Ti-6Al-4V by EAμRT with a continuous DC of 100 A was performed. Figure 4.20 is the produced channel depth predictions with a α-corrected model. The α-corrected model demonstrates an excellent depth prediction with a good agreement with experiments. It further confirms that the α-function indeed accurately corrects the contact area to be more realistic. Furthermore, the model gives analytical evidence to testify that the Joule heating effect in EAμRT eases deformation and promotes texturing.

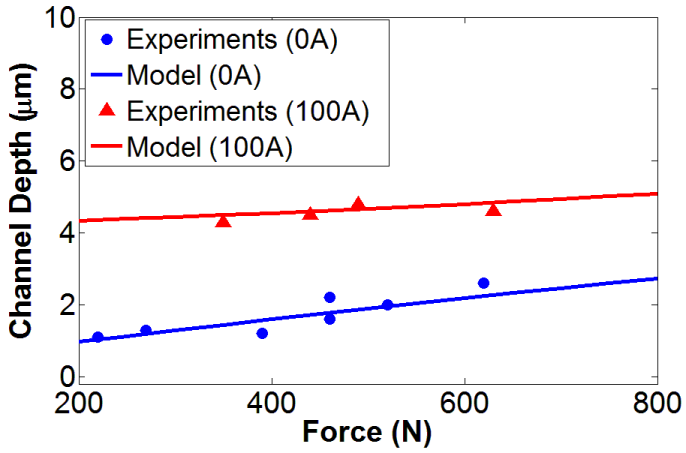

Figure 4.20 Channel depth prediction for electrically-assisted microrolling-based texturing of Ti-6Al-4V

4.4 Conclusion

An analytical model has been developed for channel depth prediction in electrically-assisted microrolling-based texturing (EAμRT). The predicted results established a good agreement with the experimental results. The α-factor/function in the model enables the calibration of the contact geometry with experimental data for a better channel depth prediction in the EAμRT. It improves the correction of contact area that is affected by the tool defects and wears. It is essentially important for precise contact area adjustment for the processes in which tool-workpiece contact is a determining factor, especially for the forming tools with micro-scaled textures.

The analytical model in channel depth prediction gives an insight that contact area is a determining factor in microforming and Joule heating. The differences in contact geometry will lead to remarkable impacts on the generated heating results. The texturing tool in this study gives a favor geometry condition for an impressive heating because of its tooth tips allowing small tool-workpiece contact area. The small contact area concentrates the electric current so that smaller electric current input is required. Note that this may be only for the case of electric current flowing from one roll to the other in the workpiece thickness direction. Furthermore, however, the contact increases with texture depth resulting in a lower current density. Too-deep textures may weaken or even vanish the Joule heating effect. Also, this current flow configuration may not be suitable for flat rolling, which a smooth roll is used instead of a pre-textured roll. The smooth roll greatly increases the roll-workpiece contact area and leads to a reduction of current density for the Joule heating. Therefore, for the situation of flat rolling and texturing with deep features, instead of in-thickness direction, more noticeable Joule heating effect can be achieved when current is set flowing along the workpiece length direction, i.e., from one end of the sheet to the other, and in which the current density is predominated by the

sheet thickness and width. Consequently, the electric current flow direction should be taken into account in electrically-assisted forming, particularly in texturing.

Chapter 5

A Case Study Microrolling-based Texturing Produced Surface: Functional Surface Production

This chapter presents an application example of textured surfaces produced by microrolling-based texturing (μRT). The products of different texturing processes leave the fabricated textures unique characteristics inherently given by their processes. Material pile-ups at the texture openings defines the characteristic of μRT differing from other processes, such as machining and laser texturing. The inherent characteristic corresponding to the process brings a textured surface a hierarchical roughness altering the hydrophobic property of the surface. In an experiment, aluminum (AA3003-H14) surfaces were textured with different texture dimensions by μRT. The hydrophobicity improvement of the textured aluminum surfaces is investigated in this chapter.

1. A Functional Surface: Surfaces with Hydrophobicity

"Functions" or "properties" can be enhanced or imparted to a surface by modifying it, for example by adding coating or creating surface textures. Those surfaces with "functions" are termed as "(multi)functional surfaces". The functions are the enhanced or added surface properties, such as hydrodynamic behavior[183], tribological behavior[8–11], optical reflectivity[184] and heat exchange efficiency[185]. Researchers are interested in one particular behavior -- Wetting behavior – because it makes it possible to control the liquid behavior on a surface. One of the interests is to create a surface with water repelling ability, i.e., a (super)hydrophobic surface.

The degree of water repellence can be measured by the contact angle between the tangent of a water droplet and its attached surface, as shown in Figure 5.1. Surfaces with contact angles larger than 90° and 150° are defined as hydrophobic and superhydrophobic surfaces, respectively. Surfaces with a high ability in liquid repellence also have a so-call "self-cleaning" effect because liquids and contaminated liquids cannot attach on the surface. The hydrophobicity of a surface highly depends on the surface energy of the surface material. Material with lower surface energy has a lower tendency to disrupt intermolecular bonds between the surface and contacting liquid. Besides, the topography of a surface also impacts its hydrophobicity. Reducing the liquid-surface contact area can limit the liquid attachment to the surface. Therefore, the creation of a surface with hydrophobicity can be done by lowering its surface energy and altering its surface topography, such as roughness. Surface energy can be modified by coating the surface with a lower surface energy substance. However, the substrate materials and working environments may limit the application of coatings. The alternative method is surface texturing. By creating micro surface features with appropriate dimensions, the liquid-surface contact area can be minimized for liquid adherence to the surface. Furthermore, textures with appropriate dimensions help to form a composite solid-liquid-air interface to increase the contact angle [186]. Texturing of surfaces can be performed by different conventional methods: micromachining[120], laser material processing[104–108,187], sandblasting[188]. photolithography[189], electrochemical etching[124], chemical vapor deposition[190] and anodization[191]. Microrolling-based texturing (μRT) is an alternative for surface texturing. It is suitable for texturing surfaces with large surface areas and infinite lengths in a relatively higher production rate than micromachining. μRT is likewise less energy intensive than laser texturing. Its fabrication process is relatively simple: it just needs a pre-textured roll.

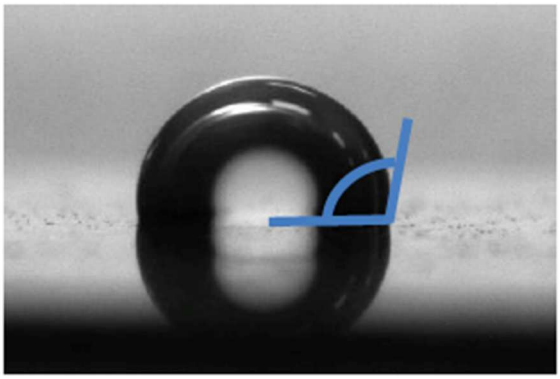

Figure 5.1 An illustration of contact angle

2. The Hypothesis

Besides the designated texture geometry, each texturing method produces unique characteristics. These characteristics also impacts on the hydrophobicity of a textured surface even if the geometries are the same. For example, micromachining produces a texture with sharper edges than those produced by µRT. From a cross-section image of textures formed by µRT in Figure 5.2, round corners can be found. This is the characteristic of texture produced by µRT and may not be observed in other texturing processes. Therefore, the process itself is also an inherent factor affecting the hydrophobicity of a surface. In Figure 5.3, dimples or valleys can be seen on some of the pillar tops produced by µRT. These characteristics may be associated with a concept of hierarchical roughness/structures[186,192] in which multiscale features are superimposed. For instance, submicron/nanofeatures superimpose over a microscale feature. The hierarchical structures promote the formation of a liquid-air-solid interface, which reduces the liquid adhesion to a surface and results in a hydrophobic effect. The inherent hierarchical nature of textures results from characteristics of the manufacturing process. For example, femtosecond laser ablation induces superhydrophobic properties on the surfaces of steel, aluminum, and tungsten carbide in which contact angles between 150° to 180° were measured[193] .

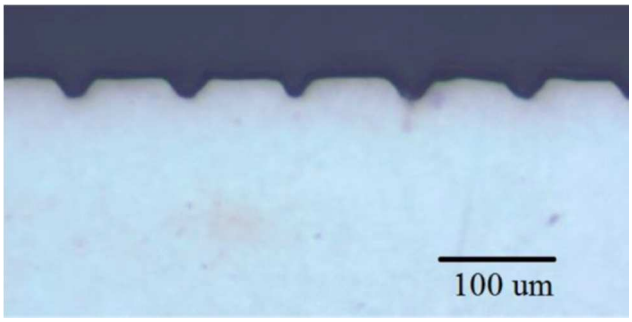

Figure 5.2 Cross-sectional optical image of textures produced by microrolling-based texturing

In μRT, textures are produced by plastic deformation. Due to incompressibility and mass conservation, material flows to the region with less stress under compression and piles up around a die, as illustrated in Figure 5.4. The amount and the shape of pile-ups depend on the depth of indentation, friction coefficients, temperature, and force[194]. Figure 5.5 shows the simulation of pile-ups under different rolling forces and friction coefficients in μRT. Depending on the dimensions of the designated textures, the pile-ups can create a hierarchical structure, as illustrated in Figure 5.6(b), to form air pockets. These air pockets separate liquid from the surface by forming a solid-air-liquid interface, preventing liquid adhesion to the surface. As a result, the surface becomes more hydrophobic than those textures without pile-ups.

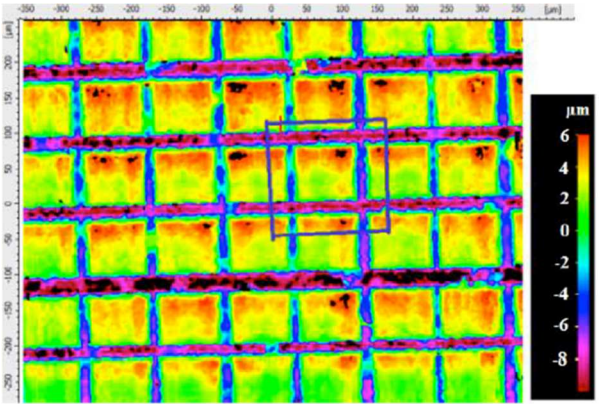

Figure 5.3 Topography of a surface textured by microrolling-based texturing

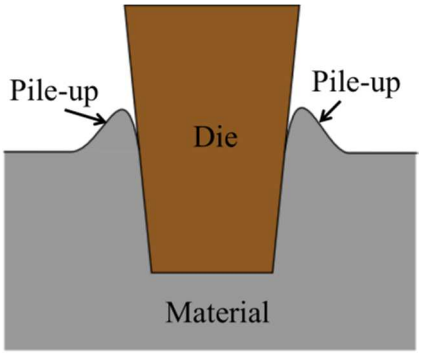

Figure 5.4 An illustration of pile-up effect

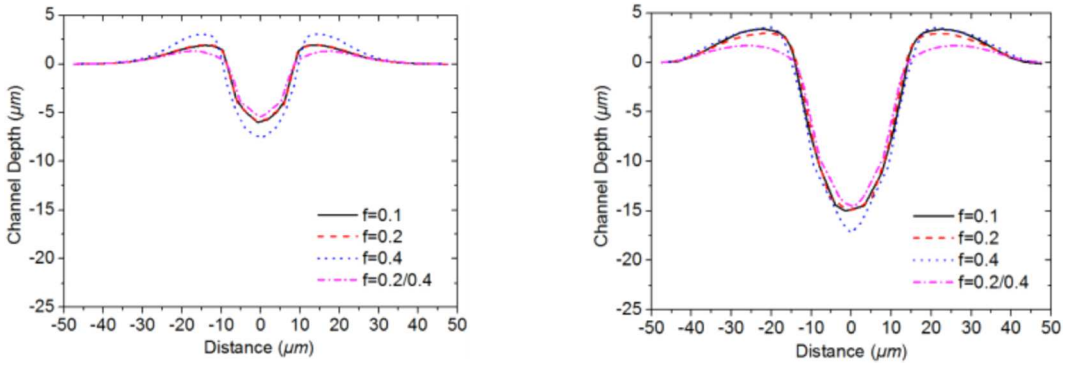

(a) Rolling force = 400 N (b) Rolling force = 800 N

Figure 5.5 Numerical simulation of pile-up under different friction conditions and rolling forces

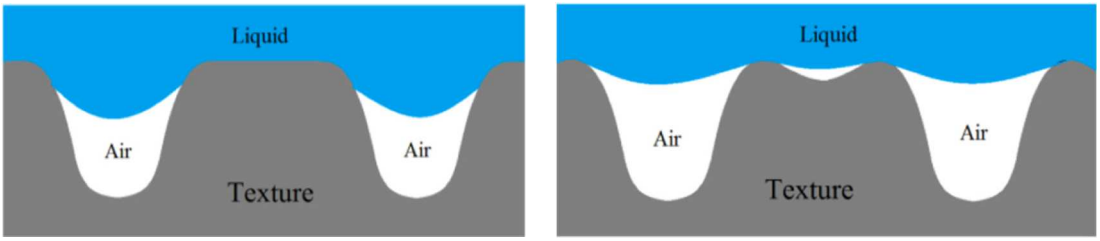

(a) (b)

Figure 5.6 Schematic of the pile-up effect on liquid adhesion in the hypothesis: (a) textures without pile-ups and (b) textures with pile-ups

3. Experimental Settings and Contact Angle Measurements

To enable the formation of air pockets illustrated in Figure 5.6, micro-pillar structures were produced by 2-pass μRT so that material could pile up to form air pockets on the tops of pillars. Note that the pile ups were randomly shaped and were found on virtually all pillar tops. Precise production of pile-ups on pillar tops requires controls in rolling force, rolling speed and temperature as well as texture geometry design. However, this is beyond the scope of this study. An optical image of the micro-pillar structures is shown in Figure 5.7. A pre-textured roll of Figure 4.5(a) was employed for texturing. A 0.4 mm thick aluminum sheet (AA3003-H14) was first textured by producing grooves along the rolling direction. Then, the textured sheet was cut into the same length as the pre-textured width and rotated 90° for the second pass μRT. In the second pass, grooves perpendicular to the first pass grooves resulted in square patterned textures, i.e., pillars. All the μRT were performed at room temperature and a rolling speed of approximately 86 mm/min. The procedures of 2-pass μRT are depicted in Figure 5.8. Note that the pre-texture roll is made of tungsten carbide, which is much harder than the workpiece material, so there are no observable wears between passes. In order to compare the effect of texture geometry on surface hydrophobicity, coarse and fine square patterned textures were produced. Therefore, middle and right sections of the pre-textured roll were used because of their significant differences in groove spacing referred to Table 2.1 in Chapter 2.

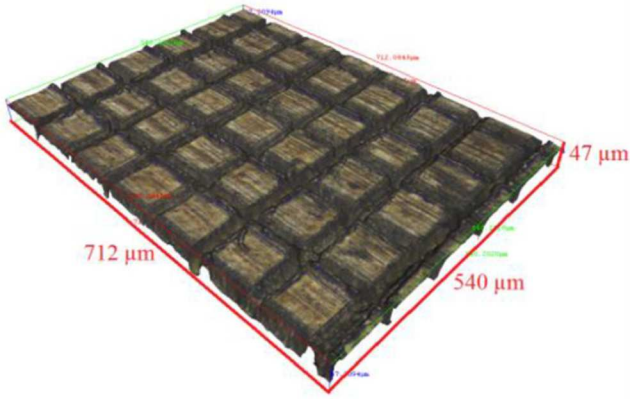

Figure 5.7 An optical 3D image of micro-pillar textures produced on AA3003 by 2-pass microrolling-based texturing

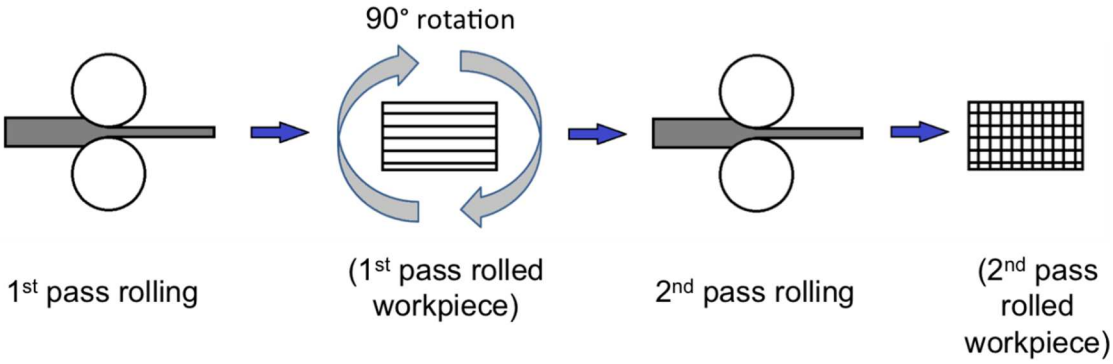

Figure 5.8 Procedures of 2-pass microrolling-based texturing for square patterned texture fabrication

Since pile-ups do not necessarily form air-pockets on pillar tops in the current texturing process, to test the hypothesis that valley-topped pillars enhance surface hydrophobicity, both flat-top and valley-topped pillar structures were reproduced by laser induced plasma micro-machining (LIPMM). LIPMM has better control in the dimensions of valley-topped pillars during the process. The schematic of LIPMM is depicted in Figure 5.9. However, compared to µRT, LIPMM is an energy intensive process with a long processing time that lowers the cost and

energy efficiencies in the process for mass production. Therefore, LIPMM is utilized for the purpose of concept validation only. For the LIPMM process, a commercially available Nd-YVO_4 laser (Lumera Laser, Inc., Santa Clara, CA) with 8 ps pulse duration operating at its second harmonic (532 nm wavelength) was used. The pulse petition frequency varies between 10kHz and 50kHz depending on the processing situation. An external power meter (Gentec Solo 2(R2)) was utilized for the maximum pulse energy measurement. A maximum of 6 μJ pulses were achieved with the consideration of reflection and transmission loses within the beam delivery system. A Gaussian beam with a spot size of 10.5 μm ($1/e^2$) was focused using a 25 mm focusing lens. During the LIPMM process, a workpiece was mounted on a five-axis motion stage with a 10 nm translation resolution and immersed in a dielectric medium. Then, a pulsed laser beam was focused in a dielectric medium to create localized thermal plasma. The plasma was then brought in contact with the workpiece for texture machining through thermomechanical ablation[195]. The workpiece was moving at a feed rate of 0.4 mm/s for a single groove machining. Grooves were produced in both longitudinal and transverse directions for pillar structure fabrication. A dimple was machined on each pillar top separately by keeping the workpiece stationary. A 3D optical image of a LIPMM textured AA3003 surface is shown in Figure 5.10. Note that textures are fabricated on the same material (AA3003) in both μRT and LIPMM.

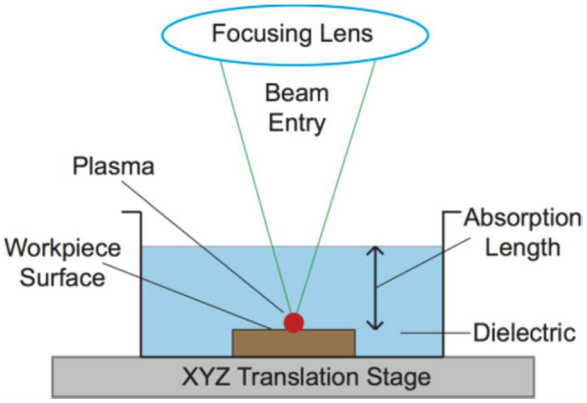

Figure 5.9 Schematic of the LIPMM process

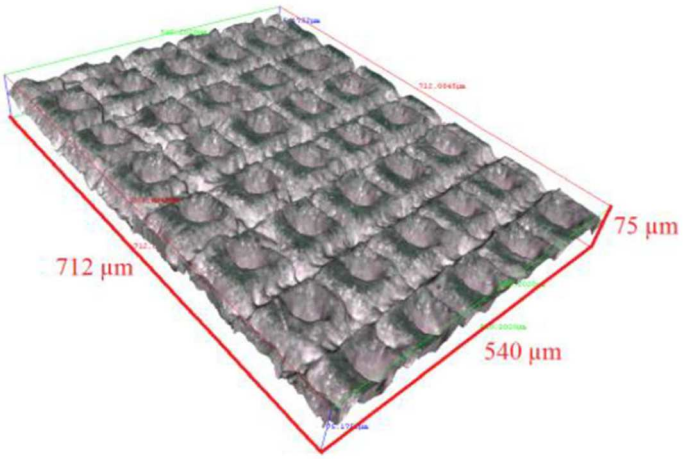

Figure 5.10 An optical 3D image of valley-topped pillar structures produced on AA3003 by LIPMM

After texture fabrication, texture geometry on each surface was measured with an optical three-dimensional microcoordinate system, Alicona InfiniteFocus, using a 20× magnification with the vertical and lateral resolutions of 0.05 µm and 2 µm, respectively. Then, the contact angle of the textured surfaces was measured. Prior to measurement, surfaces were cleaned with acetone, rinsed with water, and air-dried. The contact angle measurements were performed by a Drip Shape Analyzer DSA30 (Kruss, Germany), which particularly designed for droplet imaging and contact angle measurement. For the measurement, a single water droplet with dose size of 3 µl was slowly placed on a surface. The dose was controlled by the analysis system. On each surface, measurements were repeated for 5 times and an average value was taken for investigation.

4. Results and Discussion

The impacts on the hydrophobicity of textured surfaces due to their surface texture geometry are studied. Investigations on the effects of various aspects of texture geometry including surface area-volume ratio and groove aspect ratio are conducted. For the investigation, fine (denoted by

"F") and coarse (denoted by "C") texture patterns with different texture depth, i.e., pillar height, were produced via μRT. Each pattern has two different texture depths. Note that the teeth of the pre-textured roll were not fully indented into the material so that spaces were left for material pile ups at the groove openings. The dimensions of textures are summarized in Table 5.1. Figures 5.11 and 5.12 show the images and the average contact angles on each textured surfaces. The error bars in Figure 5.12 represents the minimum and the maximum contact angles in the five measurements. First, the contact angle of a surface without texture was measured and a mean contact angle of 100° was obtained. Results show that surfaces with textures had larger contact angles than the surface without texture, except C1 surface. C1 surface has coarse and shallow texture of about 1μm, which is comparable to the initial roughness of the initial surface, i.e., non-textured surface. The initial surface roughness was Ra = 0.3 μm. Because the imprinted texture on C1 surface did not produce a significant alternation on its initial surface topography, the hydrophobicity was not improved noticeably to result in a significant contact angle increase. Contact angles ranging from 110° to 130° were measured on C2, F1 and F2 surfaces. For both fine and coarse texture patterns, deeper textures had larger contact angles, which can be reflected by F2 and C2 surfaces when they are compared to F1 and C1, respectively. Additionally, the pillar surface fractions of fine and coarse textures were about 64% and 57%, respectively. The pillar surface fraction is defined as the ratio of the total pillar-top area to the total surface area. According to the theory, the percentage of pillar top area affects the contact angle because it determines the area of water droplet adhesion. However, the current results are not sufficient to make a comparison because the depth of textures varied differently.

Table 5.1 Summary of texture dimensions produced by microrolling-based texturing

Label	Average pillar width (μm)	Average groove width (μm)	Average groove depth (μm)
C1	200	65	1 ± 0.9
C2	200	65	15 ± 1.1
F1	100	25	4 ± 0.9
F1	100	25	7 ± 0.7

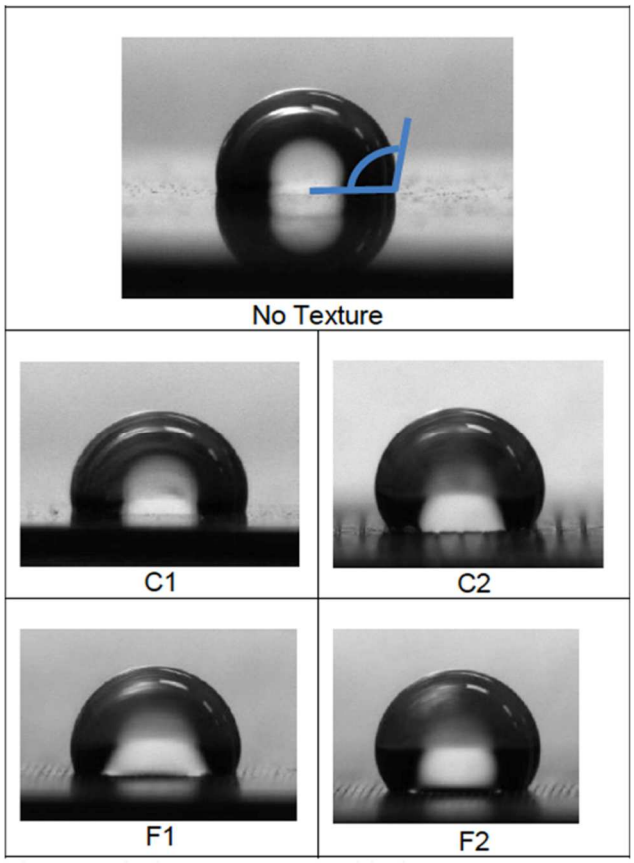

Figure 5.11 Images of water droplets on different textured surfaces produced by microrolling-based texturing.

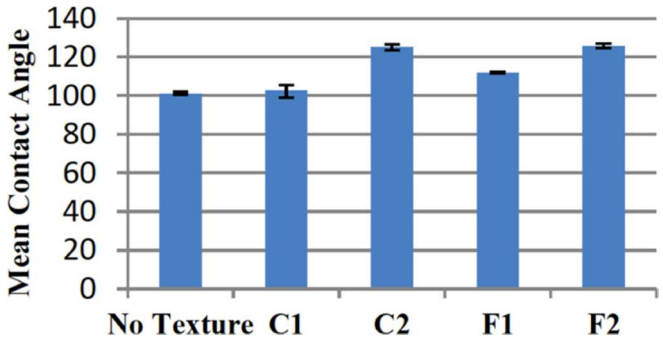

Figure 5.12 Mean contact angles of different textured surfaces produced by microrolling-based texturing

The results on the effect of groove aspect ratio of a texture on the surface hydrophobicity are shown in Figure 5.13. Note that there are noticeable differences in widths between grooves and pillars. Results show that contact angle increases with increasing aspect ratios for both fine and coarse textures. The contact angle of the surface with a texture groove aspect ratio of 0.02 is about 105°. This value is similar to the result of a non-textured surface. This observation shows that textures with too small of an aspect ratio is like a non-textured surface and it is not enough to exercise influence on hydrophobicity improvement. When the aspect ratio increases, the contact angle can be improved from 105° to 125°. The results are experimentally consistent with the theory derived by Patankar[196]. His theoretical method for contact angle calculation found that increasing texture aspect ratio led to an increase of contact angle. Furthermore, although larger contact angle can be achieved by increasing the groove aspect ratio, there is a limit capping the contact angle. According to the result, there is no remarkable change in contact angle when the aspect ratio is above 0.2.

The reason of aspect ratio increasing contact angle can be explained by the formation of a composite solid-liquid-air interface[186]. The grooves formed air pockets between the liquid and solid surfaces preventing their adhesions to each other. This composite solid-liquid-air interface

increases the contact angle of a water droplet. With a larger air pocket, the solid area for liquid attachment decreases. Therefore, the contact angle increases with increasing aspect ratio. However, there is a limit to upper-bound the aspect ratio. Otherwise, the air pocket will be too large so that water can fall into and land on the bottom of the air pocket, i.e., the groove, due to the domination of water mass weight over the hydrogen bonds to the groove opening. This happens when the gravity-capillary amplitude of a liquid is comparable to the groove depth. According to the results in Figure 5.13, when the aspect ratio was 0.02, the groove was too shallow to transit the interface to a composite solid-liquid-air interface. As a result, the contact angle was not increased. Meanwhile, when the aspect ratio was above 0.2, the groove depth became comparable to the water gravity-capillary wave amplitude and water fell into the groove leading to no further contact angle improvement.

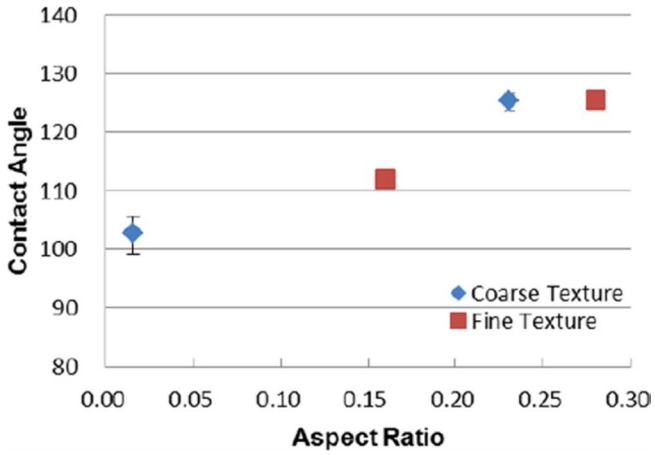

Figure 5.13 Effect of groove aspect ratio on contact angles of microrolling-based texturing produced surfaces

Figure 5.14 is the contact angle of surfaces with the pillars having different pillar surface area-to-volume ratios. The surface area-to-volume ratio is the ratio of the total surface area of a pillar to

its volume. The total pillar surface area includes the pillar top area and four pillar wall areas. Generally, the contact angle is in a reverse relationship with the pillar surface area-to-volume ratio for both fine and coarse texture patterns. When the ratio is below 0.2, the contact angles were 125°. Then, the contact angles start to drop. However, the slopes of the drop are different with texture patterns. The difference in slopes reflects the sensitivities of textures toward the ratio on the contact angle. Fine texture pattern surface resulted in a steeper slope than the coarse texture. Its contact angle drops rapidly when the ratio is slightly changed from 0.2 to 0.3. Therefore, fine texture surface is very sensitive to the ratio change.

Both the contact area and groove depth varies the hydrophobicity of a textured surface. In other words, the pillar width and height are the determining factors affecting the improvement of the contact angle. The surface area-to-volume ratio was varied by the change of pillar height, i.e., the groove depth, and the pillar width, i.e., the texture pattern resolution. A larger ratio had a larger area per volume for liquid attachment, and therefore, a smaller contact angle was obtained. Furthermore, the pillar surface fraction of the fine texture pattern was 64%, which is higher than the 57% of the coarse pattern. The higher pillar surface fraction of the fine texture pattern combines with the effect of the surface area-to-volume ratio, resulting in a sharper drop in the contact angles exhibited on fine texture patterned surfaces. By combing the results in Figure 5.13, textures with finer and taller pillars promote larger contact angles and improve hydrophobicity of a textured surface. However, the variation of pillar geometry of a texture pattern with higher pillar density may significantly impact on the hydrophobicity of a surface.

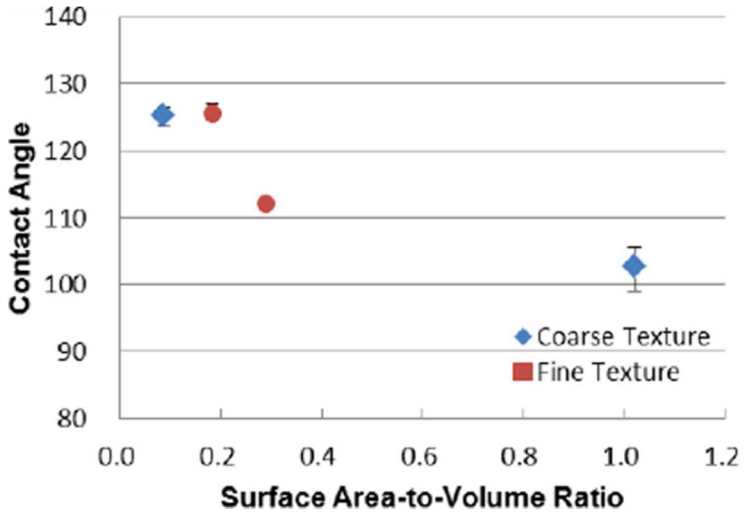

Figure 5.14 Effect of surface area-to-volume ratio on the contact angle of microrolling-based texturing produced surfaces

Due to the pile-up effects at the texture openings, valleys were formed on some of the pillar tops formed by 2-pass μRT (Figure 5.3). To prove the valley-topped pillars further improve the hydrophobicity of a surface, valley-topped pillars were replicated by LIPMM. The 3D image of LIPMM refabricated valley-topped pillars can be found in Figure 5.10. The LIPMM textured surfaces were taken for contact angle tests. The images of water droplets on the textured surfaces and the corresponding mean contact angles are shown in Figures 5.15 and 5.16, respectively. Both textured surfaces resulted in larger contact angles than the surface without texture. The contact angle improved from about 95° to 105° on a textured surface with flat-top pillars. The valley-topped pillars further improved the contact angle to 120°. There were approximately 10° and 20° contact angle increases in flat-top and valley-topped pillar textured surfaces, respectively. The results successfully prove the hypothesis that the valley-topped pillars formed due to the pile-up characteristic in μRT created a hierarchical roughness feature to a textured surface for a surface hydrophobicity improvement. The valleys are the sub-structures and act as

the air pockets to transit the liquid-solid interface to a composite liquid-air-solid interface at the contact between the pillar-top and liquid. The less area for liquid attachment improves the surface hydrophobicity resulting in a larger contact angle. Therefore, surface textures with valley-topped pillars further promote its hydrophobicity than those with flat-top pillars.

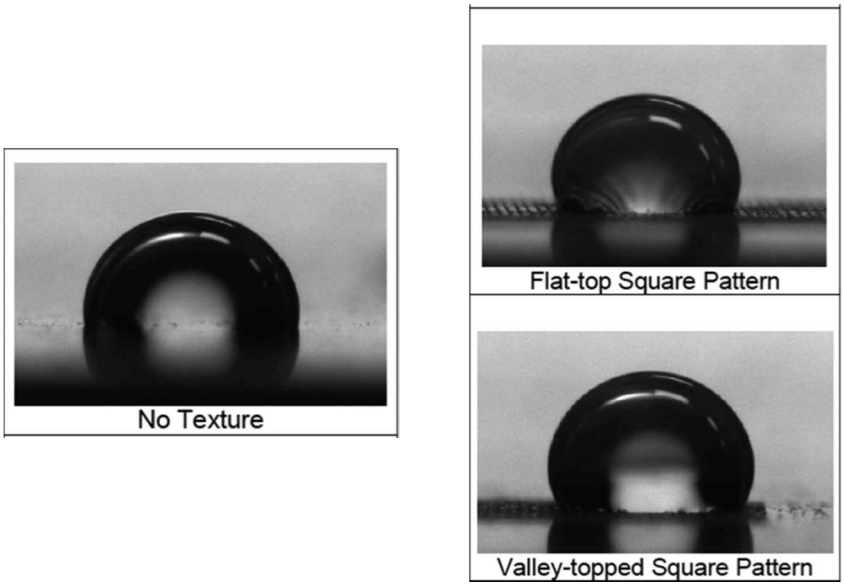

Figure 5.15 Images of contact angles on different textured surfaces produced by LIPMM

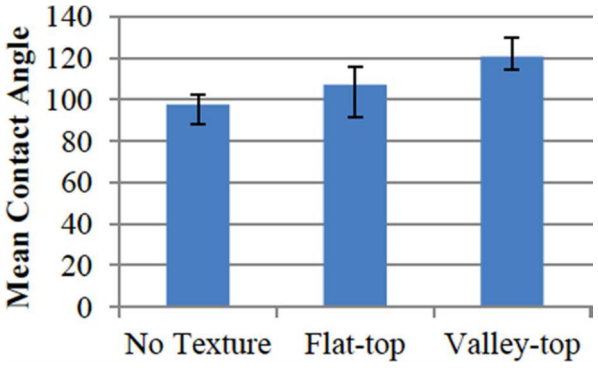

Figure 5.16 Mean contact angles of different LIPMM textured surfaces

This study also examined the contact angle anisotropy on unidirectional grooves. Contact angles were measured in both longitudinal and transverse directions on the surfaces that μRT produced with fine and coarse grooves. The coarse grooves have a width and a depth of 65 μm and 17 μm, respectively, while the fine grooves have a width and a depth of 25 μm and 7 μm, respectively. The contact angles measured in both longitudinal and transverse directions are compared with square pattern textures, i.e., pillar patterns, in Figure 5.17. Contact angles on both fine and coarse grooves imprinted surfaces do not have a significant improvement in transverse direction compared to a smooth surface, i.e., the control. However, remarkable contact angle improvements were observed in the longitudinal direction; contact angles range between 130° and 140° was achieved. The contact angles in this orientation even exhibited better improvement than square pattern textured surface, i.e., F and C cases. The difference of water droplet shapes in different directions can be seen in Figure 5.18. The remarkable contact angle improvement in the longitudinal direction is attributed to the disruption of the surface continuity by the grooves. The discontinuity of the surface prevents the water from attaching to the surface. As a result, the hydrophobic property of a surface is reinforced resulting in a large contact angle exhibition than that in the transverse orientation.

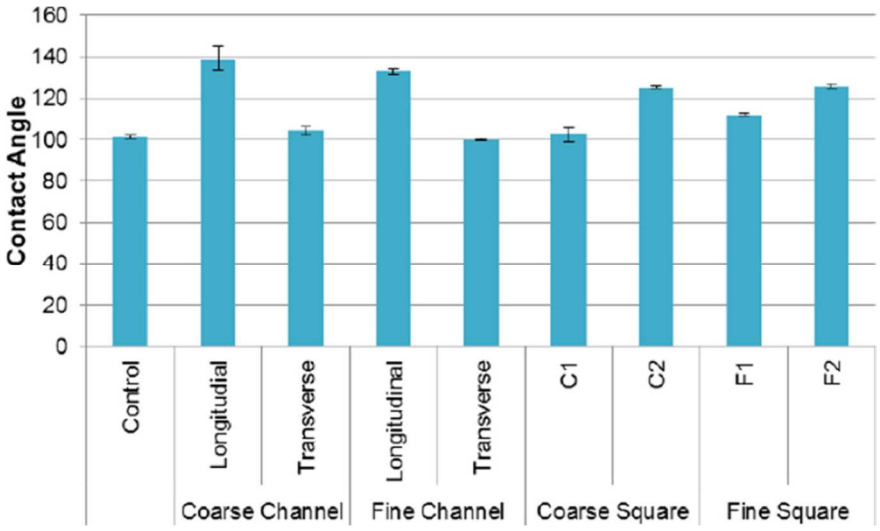

Figure 5.17 Contact angles on different microrolling-based texturing produced surface

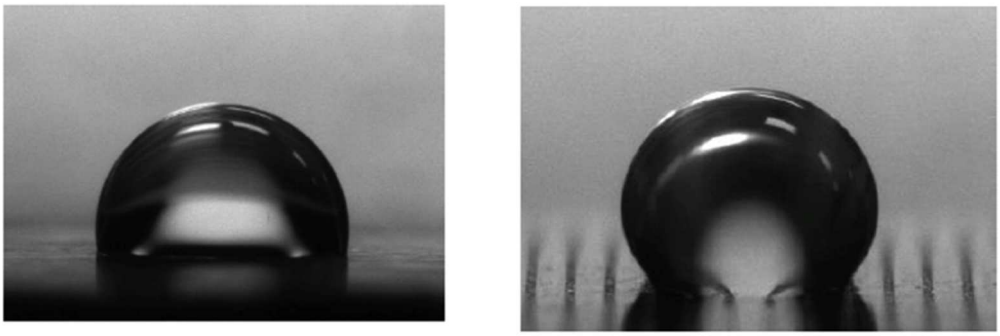

Figure 5.18 Images of contact angles on grooves in different orientations

5. *Conclusion*

Microrolling-based texturing (μRT) is a high-yield texturing process particularly suitable for texturing a surface with an extended surface area. The process can be applied to the productions of surfaces with improved hydrophobic properties. The μRT textured surfaces demonstrated different degrees of improvement on their hydrophobic properties depending on the texture geometry. Through the contact angle tests, textured surfaces have better hydrophobicity than the surface without textures. The grooves' aspect ratio and pillar surface area-to-volume ratio impact

the surface hydrophobicity. Deeper and finer texture exhibited more significant improvements. However, the change of hydrophobic behavior is more sensitive to a surface with finer textures. Additionally, the pile-up effect, which is a unique feature left on the formed texture in μRT, produced valleys on the top of pillars, which are formed by 2-pass μRT. The valley-topped pillar feature combining the pillars created a hierarchical roughness to the surface for further hydrophobicity improvement. Moreover, the anisotropy of textures results in different contact angle in different orientations.

Chapter 6

Conclusion and More

This chapter concludes the presented study. It summarizes the work and findings in both electrically-assisted microrolling-based texturing and electrically-assisted roll bonding, and gives some further discussion on the electrically-assisted microrolling. Finally, insights on future need and development related to this study are also given in the end for the future research.

6.1 Project Summary

This study investigated and evaluated the process of electrically-assisted microrolling-based texturing (EAμRT) for the fabrication of micro surface features on aluminum and titanium, and electrically-assisted roll bond (EARB) for the production of Al/Al and Al/Cu laminated metal composites (LMCs). There are numerous studies reported that when electric current passes thought a material, depending on the amount and the form of the applied current, such as continuous and pulsed DC, there may be the athermal effect other than the thermal effect, i.e., the Joule heating. However, the mechanism of the athermal effect, known as the electron wind effect, is still unclear and be proved in-situ, leading to a doubt on its existence. Nevertheless, the existence of the thermal effect is undoubtedly true and well-accepted. Therefore, in this presented study, continuous direct current is utilized to serve as a heating mean for the material softening effect. The rapid and localized heating effect allows simultaneous execution of material heating and forming, resulting in faster production. The softening effect also benefits to

the machine load reduction. Moreover, the passage of current also provides a local heating in the desired region to reduce energy loss of heating at the regions where heating is not required.

1. *Forming Force Reduction*

Due to the Joule heating effect, workpiece materials are softened. Therefore, there are reductions in the flow stress of the materials. The reduced flow stress of a material decreases the force required to form the material. Decreases of rolling forces due to the Joule heating effect can be seen in both EAμRT and EARB. However, the significance of reduction varies with materials. Besides the current density affecting the amount of heat generated for material softening, the material properties also influence the heating effectiveness. Materials with high electrical resistivities generally have a better heating effect resulting in a larger flow stress reduction for a lower forming force. For example, titanium has a larger electrical resistivity than aluminum, therefore, it has a more significant Joule heating effect than aluminum, resulting in a larger improvement in channel depth in EAμRT.

The forming force reduction brought by the Joule heating also benefits in the production of laminated metal composite by EARB. A large forming force is always required in roll bonding of sheet metals since a high percentage of thickness reduction is necessary, and it creates a challenge to the process. The Joule heating induced material softening effect in EARB provides a solution to this problem. EARB greatly reduces the rolling forces required in the production of both Al/Al and Al/Cu LMCs.

2. Improvement in Bond Strength of Laminate Metal Composites

EARB produces Al/Al and Al/Cu LMCs with improved bond strength. The elevated interface temperature provides a better processing condition for bond formations. Furthermore, the localized heating effect in the bonding interface associating with the surface topography causes

hot spots at the interface. The hot spot temperatures can be as high as the melting point of aluminum, according to the microstructure observed at the bonded interface and model prediction. The high spot temperature melts the materials and welds the materials, resulting in strong bond causing fracture of LMCs during the peeling test.

3. Analytical Modeling

This study develops two individual analytical models for both the prediction of channel depth produced in EAμRT and prediction of macro/local interface temperature in EARB. Both models are applied to the condition that continuous DC electric current flows from a roll to the other through a workpiece, which is sandwiched between rolls. The Joule heating effect is considered as a dominant effect due to electric current in both models.

In the channel depth prediction model for EAμRT, a α-factor/function is introduced to calibrate the real tool-workpiece contact area for a precise prediction of Joule heating effect and material stress. The methodology of introducing α-factor/function provides a solution to prevent over or underestimation of the Joule heating effect and material stress due to uncertain contact area with a wore tool and workpiece, especially for the tool with micro surface features.

The interface temperature prediction model for EARB models the interface temperature due to continuous DC electric current passage across two approaching bonding surfaces right before compression from the rolls. Modeling results show that there are existences of hot spots at the interface. The hot spots are due to the topography of two bonding surfaces. The hot spot temperature varies with surface topography, it is possible to reach the recrystallization temperature or even the melting point of aluminum but is not necessarily reflected in the macro temperature. The macro temperature is generally low, which is usually below 100°C.

4. Improvement in Texturing

Experimental results prove that EAμRT successfully enhances texturing on metal surfaces. EAμRT is utilized to perform texturing on aluminum and titanium surface. There are approximately 15% and 200% deeper channels produced on aluminum and titanium, respectively, when 100A continuous DC EAμRT is applied. Although the significance may be different, improvements are found in EAμRT of both aluminum and titanium. The difference is due to the material properties that titanium has higher electrical resistivity than aluminum, resulting in a much higher Joule heating temperature for a larger flow stress reduction.

5. Application of Textured Surface

Surfaces with textures are found different applications in, for example, tribological improvement and aerodynamic drag reduction. The effects of textures on surface hydrophobicity are investigated in this presented study. Depending on the texture geometry and depth, the hydrophobic behavior of a surface varies. In this study, the hydrophobicity of a surface is generally improved with texture dimensions in a micro-scaled level. The textures create the composite solid-air-liquid interface to interrupt the attachment of liquid onto the surface. Therefore, the hydrophobicity of the surface is improved. Furthermore, the surface characteristics resulted from the texture fabrication process also influences the surface hydrophobicity. The pile-up effect, which is usually found in forming process, creates some sub-micro features on the textures. These features superimpose with the designated textures to form a hierarchical roughness, providing a favorable condition for the composite solid-air-liquid interface formation in order to prevent liquid attachment on the surface. As a result, the hydrophobicity of the surface improved.

6.2 More Discussion on Electrically-assisted Microrolling

In most of the reported literature of rolling using electric current as a mean for heating, electric current is applied in the rolling direction, i.e. from one end of the workpiece to the other (ETE configuration). Differing from these investigations, the present study applies current from roll to roll (RTR configuration), i.e. in the workpiece thickness direction. The advantages of this current flow configuration are that it much localizes the heating right at the forming zone and minimizes the energy loss to the ambient at the region beyond the forming zone. However, the selection of current flow configuration also depends on the applications and forming tool geometry. For example, a pre-textured roll used in EAμT has small tooth tips, which provide small tooth-workpiece contact area to concentrate current for significant heating. However, the equivalent heating effect may be not achieved with the same current flow configuration in flat rolling, because the roll-workpiece contact may be too large resulting in low current density for significant heating at the forming zone. In the case of flat rolling of thin sheets especially with large rolls and large thickness reduction, it may be wiser to apply current along the rolling direction because the current passage area is the cross-sectional area of the sheet, which is small and easier to achieve high current density. However, if the rolling a thick sheet, the decision of current flow configuration may not be easier because the current passage in both configurations are comparable.

Besides the current passage area variation, the components affected by the Joule heating should also be taken into the consideration. Electric current does not only heat up the workpiece, but may also be the tools. In the RTR configuration, the current also passes through rolls and causes heat up of the rolls. Because the rolls in this study are large and the rolling time is short, there is no remarkable heat up of the rolls. However, in the applications with small rolls, the heating of

roll in this configuration should be noticed. Inspiring by this scenario, electric current is not only utilized for workpiece softening, it can also be used for heating up the tools, instead of the workpiece, to the process temperature for forming. For the ETE configuration, attention should be paid on the forming temperature drop at the tool contact zones. The temperature drop may be so severe that the heating effect completely vanishes if the tool mass is large.

6.3 Future Development

1. Tool Wear Prevention in Electrically-assisted microrolling

The electrically-assisted microrolling (EAμR) in this presented study is conducted under dry condition; no lubricants are applied in the process. Dry condition is usually an important reason causes tool wear. However, the situation is a bit different in EAμR. Instead of the friction, the electric sparks and high tool-workpiece interface temperature are the main causes of tool wear. Sparks are sometimes found during experiments, especially when the applied current is high. The high electric current and the continuous motion of workpiece increase the chance of electric spark occurrence. The sparks are usually found at the corners or edges of the workpiece. The unnoticeable burrs and corners usually have high charge concentration promoting electric sparks. The high-temperature sparks damage the roll and formed part surfaces. In some severe situation, it melts the workpiece material and welds the material to the rolls. The sparks may also depend on the current flow configuration, i.e. ETE or RTR configurations. Furthermore, high workpiece temperature sometimes remains some marks on both the roll and workpiece surfaces, disregarding the current flow configurations. The marks may be due to the localized heating effect of electric current, which may be dependent on the surface conditions of roll and workpiece.

Solutions to tool damages due to random electric sparks and high workpiece temperature are required to improve tool lifetime. This is especially important to surface texturing. The solution should be current flow configuration into account. For example, lubricants may be useful to spark suppression but it should be electrical conductive in RTR configuration. The continuous feeding motion of workpiece may also increase the difficulty in resolving the problems. To ensure the workpiece surface quality, measures to tool wear prevention are required in the future investigation in order to extend EAμR for the industrial mass production.

2. Bond Strength Control in Electrically-assisted Roll Bonding

Electrically-assisted roll bonding enhances the bonding of the produced laminated metal composite (LMC) sheets. However, the localized heating effect leads to non-uniform of bond strength over the interface. The non-uniformity of bond strength gives a negative impact on the quality of the LMCs. To have a quantitative understanding of the association between the bonding surface roughness or topography and Joule heating behavior at the interface may be one of the ways to improvement the bond strength uniformity.

3. Bond Strength Prediction

Understanding of the bonding mechanism in electrically-assisted bonding/welding process helps to predict the bond strength of the bonded sheets. Bond strength prediction with the association to the current density and bonding surface topography benefits the production of LMC in terms of process control and quality control. With the bond strength prediction, the production of LMC with designated non-uniform bond strength, such as enhanced bond strength at some selected regions, can be achievable.

REFERENCES

1. http://ei.marketwatch.com//Multimedia/2016/03/25/Photos/MG/MW-EI736_gross__20160325123438_MG.jpg?uuid=7766853e-f2a7-11e5-8930-0015c588dfa6.
2. http://fortune.com/2016/03/31/united-states-manufacturing-china/.
3. Hill, K., Menk, D. M., Cregger, J. &Schultz, M. Contribution of the Automotive Industry to the Economies of all Fifty State and the United States. *Cent. Automot. Res. Econ. Dev. Strateg. Gr.* 1–57 (2015). at <http://www.autoalliance.org/files/dmfile/2015-Auto-Industry-Jobs-Report.pdf>
4. http://reports.weforum.org/manufacturing-growth/aerospace-industry-infographics/.
5. Wadsworth, J. &Lesuer, D. R. Ancient and modern laminated composites Ð from the Great Pyramid of Gizeh to Y2K $. **45,** (2001).
6. Mclelland, A. R. A., Atkinson, H.V &Anderson, P. R. G. Thixoforming of a novel layered metal matrix composite. **15,** 939–945 (2014).
7. Emadoddin, E., Tajally, M. &Masoumi, M. Damping behavior of Al/SiCP multilayer composite manufactured by roll bonding. *Mater. Des.* **42,** 334–338 (2012).
8. Meng, F. *et al.* Applied Surface Science Study on effect of dimples on friction of parallel surfaces under different sliding conditions. *Appl. Surf. Sci.* **256,** 2863–2875 (2010).
9. Wakuda, M., Yamauchi, Y., Kanzaki, S. &Yasuda, Y. Effect of surface texturing on friction reduction between ceramic and steel materials under lubricated sliding contact. *Wear* **254,** 356–363 (2003).
10. Ling, T. D. *et al.* Surface texturing of drill bits for adhesion reduction and tool life

enhancement. *Tribol. Lett.* **52,** 113–122 (2013).

11. Kligerman, Y., Etsion, I. &Shinkarenko, A. Improving Tribological Performance of Piston Rings by Partial Surface Texturing. *J. Tribol.* **127,** 632 (2005).
12. Ou, J. &Rothstein, J. P. Direct velocity measurements of the flow past drag-reducing ultrahydrophobic surfaces Direct velocity measurements of the flow past drag-reducing ultrahydrophobic surfaces. **103606,** (2005).
13. Xu, L. &Siedlecki, C. A. Acta Biomaterialia Submicron-textured biomaterial surface reduces staphylococcal bacterial adhesion and biofilm formation. *Acta Biomater.* **8,** 72–81 (2012).
14. Cao, J. A Preliminary Study of the Effect of Surface Texture on Algae Cell Attachment for a Mechanical-Biological Energy Manufacturing System. *Algae* **131,** 129–132 (2009).
15. Ryk, G. &Etsion, I. Testing piston rings with partial laser surface texturing for friction reduction. *Wear* **261,** 792–796 (2006).
16. Thomson, E. Method of Electric Bending and Straightening. (1891).
17. Dewey, M. Method of Utilizing Electricity in the Formation of Sheet-Metal Articles. (1890).
18. Okazaki, K., Kagawa, M., Conrad, H. An Evaluation of the Contributions of Skin, Pinch and Heating Effects to the Electroplastic Effect in Titanium. *Mater. Sci. Eng.* **45,** 109–116 (1980).
19. Sprecher, A. F., Mannan, S. L. &Conrad, H. On the mechanisms for the electroplastic effect in metals. *Acta Metall.* **34,** 1145–1162 (1986).
20. Sprecher, A F., Mannan, S.L., Conrad, H. ON THE TEMPERATURE RISE ASSOCIATED WITH THE ELECTROPLASTIC A2d. *Scr. Mater.* **17,** 769–772 (1983).

21. Troitskii, O. A. Pressure Shaping by the Application of a High Energy. *Mater. Sci.* **75,** 37–50 (1985).

22. Troitskii, O. A. &Likhtman, V. I. The effect of the anisotropy of electron and g radiation on the deformation of zinc single crystals in teh brittle state. *Kokl. Akad. Nauk. SSSR* **148,** 332 (1963).

23. Troitskii, O. A. Radiation-induced changes in the strength and plasticity of zinc single crystals (in Russian). (1968).

24. Conrad, H. Electroplasticity in metals and ceramics. *Mater. Sci. Eng, A287* 276–287 (2000).

25. Perkins, T. a., Kronenberger, T. J. &Roth, J. T. Metallic Forging Using Electrical Flow as an Alternative to Warm/Hot Working. *J. Manuf. Sci. Eng.* **129,** 84 (2007).

26. Analysis and Observations of Current Density Sensitivity and Thermally Activated Mechanical Behavior in Electrically-Assisted Deformation.pdf.

27. Yang, D. &Conrad, H. Exploratory study into the effects of an electric field and of high current density electropulsing on the plastic deformation of TiAl. *Intermetallics* **9,** 943–947 (2001).

28. a. Y. I. K. Yu.I. Boyko and Ya.Ye. Geguzin. Experimental discovery of entrainment of dislocation by an electron wind in metals. *Zh. Eskp. Teor. Fiz.* **30,** 154 (1979).

29. Kinsey, B., Cullen, G., Jordan, A. &Mates, S. Investigation of electroplastic effect at high deformation rates for 304SS and Ti–6Al–4V. *CIRP Ann. - Manuf. Technol.* **62,** 279–282 (2013).

30. Dzialo, C. M., Siopis, M. S., Kinsey, B. L. &Weinmann, K. J. Effect of current density and zinc content during electrical-assisted forming of copper alloys. *CIRP Ann. - Manuf.*

Technol. **59,** 299–302 (2010).

31. Klimov, K. M., Burkhanov, Y. S. &Novikov, I. I. Effect of a High-Density Electric-Current on the Plastic-Deformation of Aluminum. *Strength Mater.* **17,** 782–786 (1985).
32. Salandro, W.A., Jones, J. J., McNeal, T. A., Roth, J. T., Hong, S. T., Smith, M. T. Effect of Electrical Pulsing on Various Heat Treatments of 5xxx Series Aluminum Alloys. in *Msec 2008: Proceedings of the Asme International Manufacturing Science and Engineering Conference 2008* 283–292 (2009).
33. Conrad, H., Guo, Z. &Sprecher, A. F. Effects of electropulse duration and frequency on grain growth in Cu. *Scr. Metall.* **24,** 359–362 (1990).
34. Li, X., Tang, G., Kuang, J., Li, X. &Zhu, J. Effect of current frequency on the mechanical properties, microstructure and texture evolution in AZ31 magnesium alloy strips during electroplastic rolling. *Mater. Sci. Eng. A* **612,** 406–413 (2014).
35. Conrad, H., White, J., Cao, W. D., Lu, X. P. &Sprecher, a. F. Effect of electric current pulses on fatigue characteristics of polycrystalline copper. *Mater. Sci. Eng. A* **145,** 1–12 (1991).
36. Conrad, H., Karam, N., Mannan, S. Effect of electric current pulses on the recrystallization of copper. *Scr. Metall.* **17,** 411–416 (1983).
37. Zhu, Y. H. *et al.* Effects of dynamic electropulsing on microstructure and elongation of a Zn–Al alloy. *Mater. Sci. Eng. A* **501,** 125–132 (2009).
38. Song, H. &Wang, Z. Effect of electropulsing on dislocation mobility of titanium sheet. *Trans. Nonferrous Met. Soc. China* **22,** 1599–1605 (2012).
39. Liao, H. *et al.* Effect of thermo-electropulsing rolling on mechanical properties and microstructure of AZ31 magnesium alloy. *Mater. Sci. Eng. A* **529,** 138–142 (2011).

40. Zhou, Y., Chen, G., Fu, X. &Zhou, W. Effect of electropulsing on deformation behavior of Ti–6Al–4V alloy during cold drawing. *Trans. Nonferrous Met. Soc. China* **24,** 1012–1021 (2014).

41. Tang, G., Zhang, J., Yan, Y., Zhou, H. &Fang, W. The engineering application of the electroplastic effect in the cold-drawing of stainless steel wire. *J. Mater. Process. Technol.* **137,** 96–99 (2003).

42. Li, Q., Li, R., Yue, X., Chang, G. &Zhai, Q. Effect of electropulsing on the formation of graphite during solid-state graphitization of spherical graphite iron. *Mater. Chem. Phys.* **112,** 402–406 (2008).

43. Zhu, R. F., Tang, G. Y., Shi, S. Q. &Fu, M. W. Microstructure evolution of copper strips with gradient temperature in electropulsing treatment. *J. Alloys Compd.* **581,** 160–165 (2013).

44. Zhu, R. F., Liu, J. N., Tang, G. Y., Shi, S. Q. &Fu, M. W. Properties, microstructure and texture evolution of cold rolled Cu strips under electropulsing treatment. *J. Alloys Compd.* **544,** 203–208 (2012).

45. Jiang, Y., Tang, G., Shek, C. &Liu, W. Microstructure and texture evolution of the cold-rolled AZ91 magnesium alloy strip under electropulsing treatment. *J. Alloys Compd.* **509,** 4308–4313 (2011).

46. Guan, L., Tang, G. &Chu, P. K. Recent advances and challenges in electroplastic manufacturing processing of metals. *J. Mater. Res.* **35,** 1215–1224 (2010).

47. Hu, G., Zhu, Y., Tang, G., Shek, C. &Liu, J. Effect of Electropulsing on Recrystallization and Mechanical Properties of Silicon Steel Strips. *J. Mater. Sci. Technol.* **27,** 1034–1038 (2011).

48. Liu, Y., Wang, L., Liu, H., Zhang, B. &Zhao, G. Effect of electropulsing treatment on corrosion behavior of nickel base corrosion-resistant alloy. *Trans. Nonferrous Met. Soc. China* **21,** 1970–1975 (2011).

49. Ye, X., Li, X., Song, G. &Tang, G. Effect of recovering damage and improving microstructure in the titanium alloy strip under high-energy electropulses. *J. Alloys Compd.* **616,** 173–183 (2014).

50. Jiang, Y., Guan, L., Tang, G., Shek, C. &Zhang, Z. Influence of electropulsing treatment on microstructure and mechanical properties of cold-rolled Mg – 9Al – 1Zn alloy strip. *Mater. Sci. Eng. A* **528,** 5627–5635 (2011).

51. Song, H. &Wang, Z. Improvement of mechanical properties of cold-rolled commercially pure Ti sheet by high density electropulsing. *Trans. Nonferrous Met. Soc. China* **22,** 1350–1355 (2012).

52. Jiang, Y. *et al.* Mechanism of electropulsing induced recrystallization in a cold-rolled Mg – 9Al – 1Zn alloy. *J. Alloys Compd.* **536,** 94–105 (2012).

53. Zhu, R. F., Tang, G. Y., Shi, S. Q. &Fu, M. W. Effect of electroplastic rolling on the ductility and superelasticity of TiNi shape memory alloy. *Mater. Des.* **44,** 606–611 (2013).

54. Li, G. *et al.* Effects of High Density Electropulsing Treatment on Aging Kinetics of GH4199 Alloy. *Rare Met. Mater. Eng.* **40,** 961–966 (2011).

55. Guan, L., Tang, G., Jiang, Y. &Chu, P. K. Texture evolution in cold-rolled AZ31 magnesium alloy during electropulsing treatment. *J. Alloys Compd.* **487,** 309–313 (2009).

56. Wang, Z. &Song, H. Effect of high-density electropulsing on microstructure and mechanical properties of cold-rolled TA15 titanium alloy sheet. *J. Alloys Compd.* **470,** 522–530 (2009).

57. Xu, X., Zhao, Y., Ma, B., Zhang, J. &Zhang, M. Rapid grain refinement of 2024 Al alloy through recrystallization induced by electropulsing. *Mater. Sci. Eng. A* **612,** 223–226 (2014).

58. Ma, B. *et al.* Gradient distribution of mechanical properties in the high carbon steel induced by the detour effect of the pulse current. *Mater. Des.* **49,** 168–172 (2013).

59. Zhou, Y., Xiao, S. &Guo, J. Recrystallized microstructure in cold worked brass produced by electropulsing treatment. *Mater. Lett.* **58,** 1948–1951 (2004).

60. Kim, M.-J. *et al.* Electric current-induced annealing during uniaxial tension of aluminum alloy. *Scr. Mater.* **75,** 58–61 (2014).

61. Xie, H. *et al.* Experimental investigation on electrically assisted cylindrical deep drawing of AZ31B magnesium alloy sheet. *Int. J. Adv. Manuf. Technol.* **86,** 1063–1069 (2016).

62. Song, H. &Wang, Z.-J. Microcrack healing and local recrystallization in pre-deformed sheet by high density electropulsing. *Mater. Sci. Eng. A* **490,** 1–6 (2008).

63. Zhou, Y., Guo, J., Gao, M. &He, G. Crack healing in a steel by using electropulsing technique. *Mater. Lett.* **58,** 1732–1736 (2004).

64. Stolyarov, V. V. Deformability and nanostructuring of TiNi shape-memory alloys during electroplastic rolling. *Mater. Sci. Eng. A* **503,** 18–20 (2009).

65. Ye, X., Wang, L., Tse, Z. T. H., Tang, G. &Song, G. Effects of high-energy electro-pulsing treatment on microstructure, mechanical properties and corrosion behavior of Ti–6Al–4V alloy. *Mater. Sci. Eng. C* **49,** 851–860 (2015).

66. Conrad, H. Thermally activated plastic flow of metals and ceramics with an electric field or current. *Mater. Sci. Eng. A* **322,** 100–107 (2002).

67. Magargee, J., Morestin, F. &Cao, J. Characterization of Flow Stress for Commercially

Pure Titanium Subjected to Electrically Assisted Deformation. *J. Eng. Mater. Technol.* **135,** 41003 (2013).

68. Xu, Z., Tang, G., Tian, S. &He, J. Research on the engineering application of multiple pulses treatment for recrystallization of fine copper wire. *Mater. Sci. Eng. A* **424,** 300–306 (2006).

69. Kang, W., Beniam, I. &Qidwai, S. M. In situ electron microscopy studies of electromechanical behavior in metals at the nanoscale using a novel microdevice-based system. *Rev. Sci. Instrum.* **87,** 1–10 (2016).

70. Ye, X., Tse, Z. T. H., Tang, G., Li, X. &Song, G. Effect of electropulsing treatment on microstructure and mechanical properties of cold-rolled pure titanium strips. *J. Mater. Process. Technol.* **222,** 27–32 (2015).

71. Lu, Z. *et al.* Effect of electropulsing treatment on microstructure and mechanical properties of intermetallic Al 3 Ti alloy. *J. Alloys Compd.* **708,** 834–843 (2017).

72. Jeong, H. J. *et al.* Effect of pulsed electric current on dissolution of Mg17Al12 phases in as-extruded AZ91 magnesium alloy. *Mater. Sci. Eng. A* **684,** 668–676 (2017).

73. Miyajima, Y., Abe, H., Fujii, T., Onaka, S. &Kato, M. Effects of Si on mechanical properties and microstructure evolution in ultrafine-grained Cu–Si alloys processed by accumulative roll bonding. *Acta Mater.* **61,** 1537–1544 (2013).

74. Li, C., Tan, H., Wu, W. M., Zhao, S. &Zhang, H. B. Effect of electropulsing treatment on microstructure and tensile fracture behavior of nanocrystalline Ni foil. *Mater. Sci. Eng. A* **657,** 347–352 (2016).

75. Sánchez Egea, A. J., González Rojas, H. a., Celentano, D. J., Travieso-Rodríguez, J. A. &Llumà i Fuentes, J. Electroplasticity-assisted bottom bending process. *J. Mater. Process.*

Technol. **214,** 2261–2267 (2014).

76. Zhu, Y. H. *et al.* Effects of dynamic electropulsing on microstructure and elongation of a Zn-Al alloy. *Mater. Sci. Eng. A* **501,** 125–132 (2009).

77. Fan, R., Magargee, J., Hu, P. &Cao, J. Influence of grain size and grain boundaries on the thermal and mechanical behavior of 70/30 brass under electrically-assisted deformation. *Mater. Sci. Eng. A* **574,** 218–225 (2013).

78. Li, A. P. *et al.* Direct measurement of grain boundary resistance in copper nanowires. *2011 IEEE Int. Interconnect Technol. Conf. 2011 Mater. Adv. Met. IITC/MAM 2011* 4–6 (2011). doi:10.1109/IITC.2011.5940291

79. Safa, H. *et al.* Specific Resistance Measurement of a Single Grain Boundary in Pure Niobium. 267–269 (1999).

80. Li, X., Ji, B., Zhou, Q., Chen, J. &Gao, P. Influence of Grain Size on Electrically Assisted Tensile Behavior of Ti-6Al-4V Alloy. *J. Mater. Eng. Perform.* **25,** 4514–4520 (2016).

81. Wang, X. *et al.* Size effects on flow stress behavior during electrically-assisted micro-tension in a magnesium alloy AZ31. *Mater. Sci. Eng. A* **659,** 215–224 (2016).

82. Yizhou, Z., You, Z., Guanhu, H. &Benlian, Z. The healing of quenched crack in 1045 steel under electropulsing. **1,** 17–19 (2001).

83. Yu, T., Deng, D., Wang, G. &Zhang, H. Crack healing in SUS304 stainless steel by electropulsing treatment. *J. Clean. Prod.* **113,** 989–994 (2016).

84. Lauwers, B. *et al.* Hybrid processes in manufacturing. *CIRP Ann. - Manuf. Technol.* (2014). doi:10.1016/j.cirp.2014.05.003

85. Ibrahim, M. R. *et al.* An Experimental Investigation of Cutting Temperature and Tool Wear in 2 Dimensional Ultrasonic Vibrations Assisted Micro-Milling. *MATEC Web Conf.*

95, 7005 (2017).

86. Shamoto, E. &Moriwaki, T. Study on Elliptical Vibration Cutting. *CIRP Ann. - Manuf. Technol.* **43,** 35–38 (1994).

87. Shen, X. H., Zhang, J., Xing, D. X. &Zhao, Y. A study of surface roughness variation in ultrasonic vibration-assisted milling. *Int. J. Adv. Manuf. Technol.* **58,** 553–561 (2012).

88. Zhang, X., Liu, K., Kumar, A. S. &Rahman, M. A study of the diamond tool wear suppression mechanism in vibration-assisted machining of steel. *J. Mater. Process. Technol.* **214,** 496–506 (2014).

89. Liu, Y., Suslov, S., Han, Q., Hua, L. &Xu, C. Comparison between ultrasonic vibration-assisted upsetting and conventional upsetting. *Metall. Mater. Trans. A Phys. Metall. Mater. Sci.* **44,** 3232–3244 (2013).

90. Hung, J. C. &Lin, C. C. Investigations on the material property changes of ultrasonic-vibration assisted aluminum alloy upsetting. *Mater. Des.* **45,** 412–420 (2013).

91. Shen, X. H., Zhang, J. H., Li, H., Wang, J. J. &Wang, X. C. Ultrasonic vibration-assisted milling of aluminum alloy. *Int. J. Adv. Manuf. Technol.* **63,** 41–49 (2012).

92. Ding, H., Ibrahim, R., Cheng, K. &Chen, S. J. Experimental study on machinability improvement of hardened tool steel using two dimensional vibration-assisted micro-end-milling. *Int. J. Mach. Tools Manuf.* **50,** 1115–1118 (2010).

93. Yin, S. &Shinmura, T. Vertical vibration-assisted magnetic abrasive finishing and deburring for magnesium alloy. *Int. J. Mach. Tools Manuf.* **44,** 1297–1303 (2004).

94. Park, S. S., Mostofa, M. G., Park, C. I., Mehrpouya, M. &Kim, S. Vibration assisted nano mechanical machining using AFM probe. *CIRP Ann. - Manuf. Technol.* **63,** 537–540 (2014).

95. Yao, Z. *et al.* Acoustic softening and hardening of aluminum in high-frequency vibration-assisted micro/meso forming. *Materials and Manufacturing Processes* **28,** (2013).

96. Nguyen-Tran, H. D. *et al.* A review of electrically-assisted manufacturing. *Int. J. Precis. Eng. Manuf. - Green Technol.* **2,** 365–376 (2015).

97. Yanagimoto, J. &Izumi, R. Continuous electric resistance heating — Hot forming system for high-alloy metals with poor workability. **9,** 3060–3068 (2008).

98. Electric heating type rolling device.pdf.

99. Xu, Z., Tang, G., Tian, S., Ding, F. &Tian, H. Research of electroplastic rolling of AZ31 Mg alloy strip. *J. Mater. Process. Technol.* **182,** 128–133 (2007).

100. Abou, J. D., Fatanat, T. &W, R. International Journal of Machine Tools & Manufacture Micro-texturing channel surfaces on glass with spark assisted chemical engraving. *Int. J.* **57,** 66–72 (2012).

101. Allen, D. M., Simpkins, M. &Almond, H. A novel photochemical machining process for magnesium aerospace and biomedical microengineering applications. *J. Micromechanics Microengineering* **20,** 105010 (2010).

102. Zhang, J. &Meng, Y. A study of surface texturing of carbon steel by photochemical machining. *J. Mater. Process. Technol.* **212,** 2133–2140 (2012).

103. Youn, S.-W., Okuyama, C., Takahashi, M. &Maeda, R. A study on fabrication of silicon mold for polymer hot-embossing using focused ion beam milling. *J. Mater. Process. Technol.* **201,** 548–553 (2008).

104. Luo, B. H., Shum, P. W., Zhou, Z. F. &Li, K. Y. Preparation of hydrophobic surface on steel by patterning using laser ablation process. *Surf. Coatings Technol.* **204,** 1180–1185 (2010).

105. Khan, A., Wang, Z., Sheikh, M. a., Whitehead, D. J. &Li, L. Laser micro/nano patterning of hydrophobic surface by contact particle lens array. *Appl. Surf. Sci.* **258,** 774–779 (2011).

106. Rukosuyev, M.V., Lee, J., Cho, S. J., Lim, G. &Jun, M. B. G. One-step fabrication of superhydrophobic hierarchical structures by femtosecond laser ablation. *Appl. Surf. Sci.* **313,** 411–417 (2014).

107. Kwon, M. H., Shin, H. S. &Chu, C. N. Fabrication of a super-hydrophobic surface on metal using laser ablation and electrodeposition. *Appl. Surf. Sci.* **288,** 222–228 (2014).

108. Hilgenberg, K. &Steinhoff, K. Texturing of skin-pass rolls by pulsed laser dispersing. *J. Mater. Process. Technol.* **225,** 84–92 (2015).

109. Park, D. Micro-grooving of glass using micro-abrasive jet machining. *J. Mater. Process. Technol.* **146,** 234–240 (2004).

110. Solignac, D., Sayah, a., Constantin, S., Freitag, R. &Gijs, M. a. M. Powder blasting for the realisation of microchips for bio-analytic applications. *Sensors Actuators A Phys.* **92,** 388–393 (2001).

111. Mai, J., Peng, L., Lai, X. &Lin, Z. Journal of Materials Processing Technology Electrical-assisted embossing process for fabrication of micro-channels on 316L stainless steel plate. **213,** 314–321 (2013).

112. Kuo, C. C. &Chiang, T. S. Development of a precision hot embossing tool with microstructures for microfabrication. *Int. J. Adv. Manuf. Technol.* 1–6 (2016). doi:10.1007/s00170-016-9859-7

113. Jucius, D. *et al.* Hot embossing of PTFE: Towards superhydrophobic surfaces. *Appl. Surf. Sci.* **257,** 2353–2360 (2011).

114. He, J. J. *et al.* The precision replication of a microchannel mould by hot-embossing a Zr-based bulk metallic glass. *Intermetallics* **21,** 50–55 (2012).

115. Aizawa, T., Tamaki, M. &Fukuda, T. Large area micro-texture imprinting onto metallic sheet via CNC stamping. *Procedia Eng.* **81,** 1427–1432 (2014).

116. Yamamoto, M. &Kuwabara, T. Micro form rolling : Imprinting ability of microgrooves. **1,** 232–236 (2007).

117. Inomata, Y., Fukui, K. &Shirasawa, K. Surface texturing of large area multicrystalline silicon solar cells using reactive ion etching method. *Sol. Energy Mater. Sol. Cells* **48,** 237–242 (1997).

118. Cho, C. *et al.* Surface texturing method for silicon solar cell using reactive ion etching with metal mesh. *Phys. Status Solidi* **211,** 1844–1849 (2014).

119. Yoo, J. *et al.* Random reactive ion etching texturing techniques for application of multicrystalline silicon solar cells. *Thin Solid Films* **546,** 275–278 (2013).

120. Guo, P., Lu, Y., Ehmann, K. F. &Cao, J. Generation of hierarchical micro-structures for anisotropic wetting by elliptical vibration cutting. *CIRP Ann. - Manuf. Technol.* **63,** 553–556 (2014).

121. Xu, S., Shimada, K., Mizutani, M. &Kuriyagawa, T. Fabrication of hybrid micro/nano-textured surfaces using rotary ultrasonic machining with one-point diamond tool. *International Journal of Machine Tools and Manufacture* **86,** 12–17 (2014).

122. Adithyavairavan, M. &Subbiah, S. A morphological study on direct polymer cast micro-textured hydrophobic surfaces. *Surf. Coatings Technol.* **205,** 4764–4770 (2011).

123. daSilva, E. J., Bottene, A. C., deOliveira, J. F. G., Atoatte, A. &Rodrigues, A. de S. Grinding process for profiled texturing. *CIRP Ann. - Manuf. Technol.* **65,** 337–340 (2016).

124. Sun, J. *et al.* Electrochemical fabrication of superhydrophobic Zn surfaces. *Appl. Surf. Sci.* **315,** 346–352 (2014).

125. Hao, X. *et al.* Applied Surface Science Surface micro-texturing of metallic cylindrical surface with proximity rolling-exposure lithography and electrochemical micromachining. *Appl. Surf. Sci.* **257,** 8906–8911 (2011).

126. Ike, H. &Plancak, M. Coining process as a means of controlling surface microgeometry. *J. Mater. Process. Technol.* **80–81,** 101–107 (1998).

127. Joo, B. Y., Oh, S. I. &Son, Y. K. Forming of Micro Channels with Ultra Thin Metal Foils. *CIRP Ann. - Manuf. Technol.* **53,** 243–246 (2004).

128. Sheng, L. Y., Yang, F., Xi, T. F., Lai, C. &Ye, H. Q. Influence of heat treatment on interface of Cu/Al bimetal composite fabricated by cold rolling. *Compos. Part B Eng.* **42,** 1468–1473 (2011).

129. Sawicki, S., Szota, P. &Dyja, H. Analysis of the bimetallic bars rolling during a skew rolling. *Arch. Matrerials Sci. Eng.* **32,** 53–56 (2008).

130. Xu, D. *et al.* Enhancement of Adhesion Strength by Micro-rolling Based Surface Texturing (In review). *Int. J. Adv. Manuf. Technol.*

131. Mori, K., Bay, N., Fratini, L., Micari, F. &Tekkaya, a. E. Joining by plastic deformation. *CIRP Ann. - Manuf. Technol.* **62,** 673–694 (2013).

132. Li, L., Nagai, K. &Yin, F. Progress in cold roll bonding of metals. **23001,**

133. Su, L., Lu, C., Tieu, A. K., Deng, G. &Sun, X. Ultrafine grained AA1050/AA6061 composite produced by accumulative roll bonding. *Mater. Sci. Eng. A* **559,** 345–351 (2013).

134. Ng, H. P. *et al.* Asymmetric accumulative roll bonding of aluminium–titanium composite

sheets. *Mater. Sci. Eng. A* **576,** 306–315 (2013).

135. Reihanian, M., Hadadian, F. K. &Paydar, M. H. Fabrication of Al–2vol% Al2O3/SiC hybrid composite via accumulative roll bonding (ARB): An investigation of the microstructure and mechanical properties. *Mater. Sci. Eng. A* **607,** 188–196 (2014).

136. Shabani, A., Toroghinejad, M. R. &Shafyei, A. Fabrication of Al/Ni/Cu composite by accumulative roll bonding and electroplating processes and investigation of its microstructure and mechanical properties. *Mater. Sci. Eng. A* **558,** 386–393 (2012).

137. Yu, H. L., Lu, C., Tieu, A. K. &Kong, C. Fabrication of Nanostructured Aluminum Sheets Using Four-Layer Accumulative Roll Bonding. *Mater. Manuf. Process.* **29,** 448–453 (2014).

138. Toroghinejad, M. R., Jamaati, R., Dutkiewicz, J. &Szpunar, J. a. Investigation of nanostructured aluminum/copper composite produced by accumulative roll bonding and folding process. *Mater. Des.* **51,** 274–279 (2013).

139. Wu, K. *et al.* Microstructure and mechanical properties of the Mg/Al laminated composite fabricated by accumulative roll bonding (ARB). *Mater. Sci. Eng. A* **527,** 3073–3078 (2010).

140. Hidalgo-Manrique, P., Cepeda-Jiménez, C. M., Orozco-Caballero, a., Ruano, O. a. &Carreño, F. Evolution of the microstructure, texture and creep properties of the 7075 aluminium alloy during hot accumulative roll bonding. *Mater. Sci. Eng. A* **606,** 434–442 (2014).

141. Knezevic, M. *et al.* Texture evolution in two-phase Zr/Nb lamellar composites during accumulative roll bonding. *Int. J. Plast.* **57,** 16–28 (2014).

142. Hong-zhi, Y. A. N. Key factors for warm rolled bond of 6111-aluminium strip. (2005).

143. Manesh, H. D. &Taheri, A. K. Bond strength and formability of an aluminum-clad steel sheet. *J. Alloys Compd.* **361,** 138–143 (2003).

144. Eizadjou, M., Danesh Manesh, H. &Janghorban, K. Mechanism of warm and cold roll bonding of aluminum alloy strips. *Mater. Des.* **30,** 4156–4161 (2009).

145. Bay, N., Clemensen, C., Juelstorp, O. Bond Strength in Cold Roll Bonding. *Ann. CIRP* **34,** 221–224 (1985).

146. Kadkhodaee, M., Babaiee, M., Manesh, H. D., Pakshir, M. &Hashemi, B. Evaluation of corrosion properties of Al/nanosilica nanocomposite sheets produced by accumulative roll bonding (ARB) process.pdf. *J. Alloys Compd.* **576,** 66–71 (2013).

147. Kümmel, F., Hausol, T., Hoppel, H. W. &Goken, M. Enhanced fatigue lives in AA1050A/AA5005 laminated metal composites produced by accumulative roll bonding.pdf. *Acta Mater.* **120,** 150–158 (2017).

148. Liu, C. Y. *et al.* Evaluation of mechanical properties of 1060-Al reinforced with WC particles via warm accumulative roll bonding process. *Mater. Des.* **43,** 367–372 (2013).

149. Hidalgo-Manrique, P., Cepeda-Jiménez, C. M., Ruano, O. a. &Carreño, F. Effect of warm accumulative roll bonding on the evolution of microstructure, texture and creep properties in the 7075 aluminium alloy. *Mater. Sci. Eng. A* **556,** 287–294 (2012).

150. Madaah-Hosseini, H. . &Kokabi, a. . Cold roll bonding of 5754-aluminum strips. *Mater. Sci. Eng. A* **335,** 186–190 (2002).

151. Ahmadi, A., Toroghinejad, M. R. &Najafizadeh, A. Evaluation of microstructure and mechanical properties of Al/Al2O3/SiC hybrid composite fabricated by accumulative roll bonding process. *Mater. Des.* **53,** 13–19 (2014).

152. Duan, J. Q., Quadir, M. Z. &Ferry, M. Engineering low intensity planar textures in

commercial purity nickel sheets by cross roll bonding. *Mater. Lett.* **188,** 138–141 (2017).

153. Wu, B., Li, L., Xia, C., Guo, X. &Zhou, D. Effect of surface nitridingtreatment in a steel plate on the interfacial bonding strength of the aluminum□steel clad sheets by the cold roll bonding process.pdf. *Mater. Sci. Eng. A* **682,** 270–278 (2017).

154. Hosseini, M., Pardis, N., Manesh, H. D., Abbasi, M. &Kim, D.-I. Structural characteristics of Cu/Ti bimetal composite produced by accumulative roll-bonding (ARB).pdf. *Mater. Des.* **113,** 128–136 (2017).

155. Boher, C., Roux, S.Le, Penazzi, L. &Dessain, C. Experimental investigation of the tribological behavior and wear mechanisms of tool steel grades in hot stamping of a high-strength boron steel. *Wear* **294–295,** 286–295 (2012).

156. Zeng, L. F. *et al.* High strength and thermal stability of bulk Cu/Ta nanolamellar multilayers fabricated by cross accumulative roll bonding.pdf. *Acta Mater.* **110,** 341–351 (2016).

157. Tolouei, E., Toroghinejad, M. R. &Ashrafizadeh, F. An Investigation on the Bond Strength of Aluminum Strips in the Presence of Brass Mesh after Cold Roll Bonding. **3,** 52–63 (2016).

158. Chunyang, W., Yanbin, J., Jianxin, X., Dejing, Z. &Xiaojun, Z. Effect of the steel sheet surface hardening state on interfacial bonding strength of embedded aluminum–steel composite sheet produced by cold roll bonding process.pdf. *Mater. Sci. Eng. A* **652,** 51–58 (2016).

159. Cave, J. A. &Williams, J. D. The mechanism of cold pressure welding by rolling. *J. Inst. Met.* **101,** 203–207 (1973).

160. Bay, N. Mechanisms Producing Metallic Bonds in Cold Welding. *Weld. Res. Suppl.* 137–

142 (1983).

161. Tabata, T., Masaki, S. &Azekura, K. Bond criterion in cold pressure welding of aluminium. *Mater. Sci. Technol.* **5,** 377–381 (1989).

162. Mitani, Y., Vargas, R., Z. Deformation and diffusion bonding of aluminidecoated steels. *Thin Solid Films* **111,** 37–42 (1984).

163. Hwang, Y.-M., Hsu, H.-H. &Hwang, Y.-L. Analytical and experimental study on bonding behavior at the roll gap during complex rolling of sandwich sheets. *Int. J. Mech. Sci.* **42,** 2417–2437 (2000).

164. Bambach, M., Pietryga, M., Mikloweit, a. &Hirt, G. A finite element framework for the evolution of bond strength in joining-by-forming processes. *J. Mater. Process. Technol.* **214,** 2156–2168 (2014).

165. Ng, M.-K., Fan, Z., Gao, R. X., Smith, E. F. &Cao, J. Characterization of electrically-assisted micro-rolling for surface texturing using embedded sensor. *CIRP Ann. - Manuf. Technol.* **63,** 269–272 (2014).

166. Danesh Manesh, H. &Karimi Taheri, a. The effect of annealing treatment on mechanical properties of aluminum clad steel sheet. *Mater. Des.* **24,** 617–622 (2003).

167. Quadir, M. Z., Wolz, A., Hoffman, M. &Ferry, M. Influence of processing parameters on the bond toughness of roll-bonded aluminium strip. *Scr. Mater.* **58,** 959–962 (2008).

168. Movahedi, M., Madaah-Hosseini, H. R. &Kokabi, a. H. The influence of roll bonding parameters on the bond strength of Al-3003/Zn soldering sheets. *Mater. Sci. Eng. A* **487,** 417–423 (2008).

169. Xu, Z., Peng, L. &Lai, X. Electrically assisted solid-state pressure welding process of SS 316 sheet metals. *J. Mater. Process. Technol.* **214,** 2212–2219 (2014).

170. Eaμr, M. *et al.* Micro surface-texturing by electrically-assisted micro-rolling (EAμR). (2012).

171. Ng, M.-K. *et al.* Joining sheet metals by electrically-assisted roll bonding. *CIRP Ann. - Manuf. Technol.* **64,** 273–276 (2015).

172. Fan, Z., Ng, M.-K., Gao, R. X., Cao, J. &Smith, E. F. Real-time monitoring of pressure distribution in microrolling through embedded capacitive sensing. *CIRP Ann. - Manuf. Technol.* **61,** 367–370 (2012).

173. Werschmoeller, D., Ehmann, K. &Li, X. Tool Embedded Thin Film Microsensors for Monitoring Thermal Phenomena at Tool-Workpiece Interface During Machining. **133,** 1–8 (2011).

174. Alizadeh, M. &Samiei, M. Fabrication of nanostructured Al/Cu/Mn metallic multilayer composites by accumulative roll bonding process and investigation of their mechanical properties. *Mater. Des.* **56,** 680–684 (2014).

175. Jamaati, R., Reza, M. &Amirkhanlou, S. Microstructural evolution of nanostructured steel-based composite fabricated by accumulative roll bonding. *Mater. Sci. Eng. A* **639,** 298–306 (2015).

176. Karimi, M. &Toroghinejad, M. R. An alternative method for manufacturing high-strength CP Ti–SiC composites by accumulative roll bonding process. *Mater. Des.* **59,** 494–501 (2014).

177. Hirt, G. &Thome, M. CIRP Annals - Manufacturing Technology Rolling of functional metallic surface structures. *CIRP Ann. - Manuf. Technol.* **57,** 317–320 (2008).

178. Zhou, R., Cao, J., Ehmann, K. &Xu, C. An Investigation On Surface Texturing. *J. Manuf. Sci. Eng.* **133,** 61017-1-61017–5 (2011).

179. Zhou, R., Xao, J., Xu, C. &Ehmann, K. An investigation on multi-pass deformation-based surface texturing. in *10th International Conference on Technology of Plasticity, ICTP 2011* (2011).

180. Oh, H. S., Cho, H. R., Park, H., Hong, S. T. &Chun, D. M. Study of electrically-assisted indentation for surface texturing. *Int. J. Precis. Eng. Manuf. - Green Technol.* **3,** 161–165 (2016).

181. Vanderhasten, M., Rabet, L. &Verlinden, B. Ti–6Al–4V: Deformation map and modelisation of tensile behaviour. *Mater. Des.* **29,** 1090–1098 (2008).

182. Luo, J., Li, M., Yu, W. &Li, H. The variation of strain rate sensitivity exponent and strain hardening exponent in isothermal compression of Ti–6Al–4V alloy. *Mater. Des.* **31,** 741–748 (2010).

183. Vaikuntanathan, V., Kannan, R. &Sivakumar, D. Impact of water drops onto the junction of a hydrophobic texture and a hydrophilic smooth surface. *Colloids Surfaces A Physicochem. Eng. Asp.* **369,** 65–74 (2010).

184. Malshe, A. *et al.* Bio-inspired functional surfaces for advanced applications. *CIRP Ann. - Manuf. Technol.* **62,** 607–628 (2013).

185. Hsieh, C.-C. &Yao, S.-C. Evaporative heat transfer characteristics of a water spray on micro-structured silicon surfaces. *Int. J. Heat Mass Transf.* **49,** 962–974 (2006).

186. Nosonovsky, M. &Bhushan, B. Hierarchical roughness optimization for biomimetic superhydrophobic surfaces. *Ultramicroscopy* **107,** 969–79 (2007).

187. Saxena, I., Agrawal, A. &Joshi, S. S. Fabrication of microfilters using excimer laser micromachining and testing of pressure drop. *J. Micromechanics Microengineering* **19,** 25025 (2009).

188. Horgnies, M. &Chen, J. J. Superhydrophobic concrete surfaces with integrated microtexture. *Cem. Concr. Compos.* **52,** 81–90 (2014).

189. Schmidt, J. A. &Recum, A. F.Von. Surface characterization of rnicrot ~~ t ~ d silicone. **13,** (1992).

190. Rezaei, S., Manoucheri, I., Moradian, R. &Pourabbas, B. One-step chemical vapor deposition and modification of silica nanoparticles at the lowest possible temperature and superhydrophobic surface fabrication. *Chem. Eng. J.* **252,** 11–16 (2014).

191. Gao, Y., Sun, Y. &Guo, D. Facile fabrication of superhydrophobic surfaces with low roughness on Ti–6Al–4V substrates via anodization. *Appl. Surf. Sci.* **314,** 754–759 (2014).

192. Feng, L. *et al.* Petal effect: A superhydrophobic state with high adhesive force. *Langmuir* **24,** 4114–4119 (2008).

193. Rukosuyev, M.V, Lee, J. &Jun, M. B. G. Hydrophobic Hierarchical Structure Manufacturing by Femtosecond Laser Ablation. (2013).

194. Fan, R., Ng, M., Xu, D., Hu, P. &Cao, J. Experimental and Numerical Study of Electrically-Assisted.

195. Malhotra, R., Saxena, I., Ehmann, K. &Cao, J. Laser-induced plasma micro-machining (LIPMM) for enhanced productivity and flexibility in laser-based micro-machining processes. *CIRP Ann. - Manuf. Technol.* **62,** 211–214 (2013).

196. Patankar, N. A. Mimicking the Lotus Effect : Influence of Double Roughness Structures and Slender Pillars. 8209–8213 (2004).

Appendix I: Desktop Microrolling Machine User Manual

This manual is an instruction of the operation of the desktop microrolling machine.

1. Make sure all the sensors and transducers are well connected to their corresponding amplifiers or modules.
    a. Each load cell is connected to a charge amplifier, then to a National Instrument Input Modulus;
    b. Each piezo actuator is connected to a high-voltage amplifier. Depending on the application needs, the high-voltage amplifier can be connected to National Instrument Output Modulus for the control of a piezo actuator.
    c. Each capacitive position sensor is connected to its modulus, and then to National Instrument Input Modulus;
    d. The National Instrument DQA Chassis is connected to a PC via a USB.
2. Switch on the PC.
3. Turn on the National Instrument DQA Chassis.
4. Turn on the power supplies of the capacitive position sensors.
5. Turn on the charge amplifiers connecting to the load cells, and switch them to a "Reset" Mode.
6. Turn on the high-voltage amplifier and adjust the channels, which connecting to a piezo actuator, to 200V to preload the actuator.
7. Open the LabView VI. application, "microrolling2.vi".
8. Adjust to motor speed and reset the rolls to their initial positions. The initial positions are decided and marked by the machine operator. Reset the roll position in every rolling test.

Due to there are variations in the roll diameter due to the imperfectness, it is important to reset the roll positions before roll gap adjustment.

9. To prepare the machine for the rolling test, run the VI for monitoring. Change the file name if needed.
10. Switch the charge amplifier to "Operation" mode. It is suggested to reset the amplifier before running other set of measurement.
11. Check if there are readings from the load cells and the position sensor. If not, check the connections.
12. Set the positions of the position sensors in order to have a value of zero in their reading in the VI. Hint: screw the screw fixing the sensor for fine adjustment.
13. Screw the screws on the top the machine, which are placed on top of the piezo actuators, until a load cell reading of 100-200N is achieved. This action serves two purposes: (1) to ensure the piezo-actuator touching the upper bearing house, and (2) preload the load cells. Please note that the extension limit of the piezo-actuator is 80 μm. Please check the readings of the position sensors.
14. For coarse roll gap adjustment, screw the wedge unit, locating at the bottom of the machine, to push the lower bearing house upward. To reset the wedge unit, unscrew the unit, insert a rod into the hole behind the unit, hammer the rod the push the block of the wedge unit back to its initial location.
15. For fine adjustment, screw the screws on the top of the piezo actuator until a target roll gap size is reached.
16. If an electrically-assisted rolling is preformed and sliprings are employed, forced air cooled the sliprings and the connections with compressed air by placing the valves toward them.

17. Stop the VI.
18. Steps 1 to 17 are the machine preparation for the rolling process. Repeat Steps 14 and 15 in case a roll gap size change. Please note that there may be some elastic deformation in the system, such as the screws of the piezo actuator, causing changes in the roll gap size in a few minutes after setting.
19. Prior to the rolling test, make sure the rolls are at their initial positions.
20. Turn on the forced air cooling if electrically-assisted rolling is going to be performed.
21. Before restarting the VI for the rolling test, change to file name for data export.
22. Insert the workpiece to roll gap.
23. Reset the charge amplifier and switch it to “Operation” mode.
24. Run the VI.
25. Turn on the motors; rolling starts. Push the workpiece toward the roll gap a bit if it is not being rolled.
26. Stop the VI after rolling.

Appendix II: Roll bonding experimental procedures

1. Set up the desktop microrolling system according to Appendix I.
2. Set up the power supply according to its manual.
3. Cut the ultra-thin sheet metal into a 5mm x 40mm strip.
4. Pour small amount of acetone into a small breaker. Because acetone is flammable, it is suggested to use small amount every time and refill.
5. Place the cut ultra-thin sheet metal strips in parallel as close as possible on a board, such as a wooden board, and fixed their ends with tapes.
6. Soak a cotton ball with acetone in the breaker.
7. Clean the fixed strip surfaces with the acetone soaked cotton ball.
8. Use a dry cotton ball to dry the cleaned strip surfaces.
9. Wire brush the strip surfaces. Moving the turning brush along the strips for about 30 seconds.
10. Remove the tapes fixing the strips and face the brushed sides facing each other.
11. Insert the strips into a folded stainless steel sheet, which acts as a “clip”.
12. Insert the “clipped” metal laminates into the roll gap of the microrolling machine.
13. Turn on the motor and rolling starts.
14. Immediately after Step 12, switch on the power supply.
15. After rolling, switch off the power supply, and then stop the motor.
16. Stop the microrolling VI.

APPENDIX III: Test Details for the EARB Wire Brushing Effect Investigation

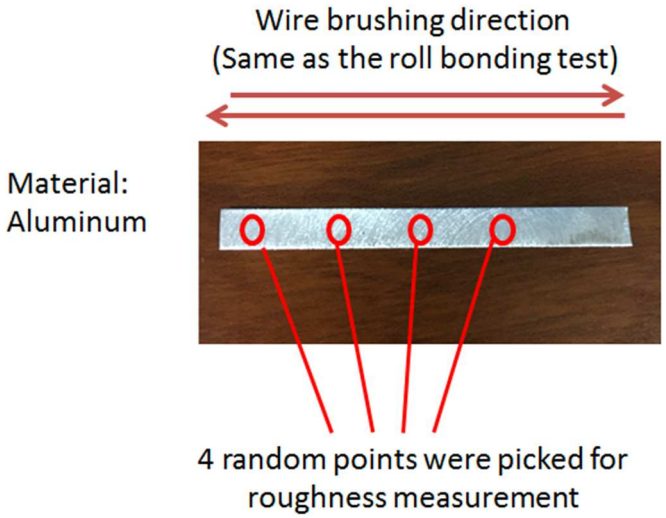

Test Details:

- Brushing time: 10s, 20s and 30s.
- At least 3 samples were brushed for each brushing time.
- First measurement completed in 3-4 mins immediately after brushing.
- Second measurement was conducted after 30 mins of brushing.
- Initial surface roughness (Ra): 0.3 µm

Results:

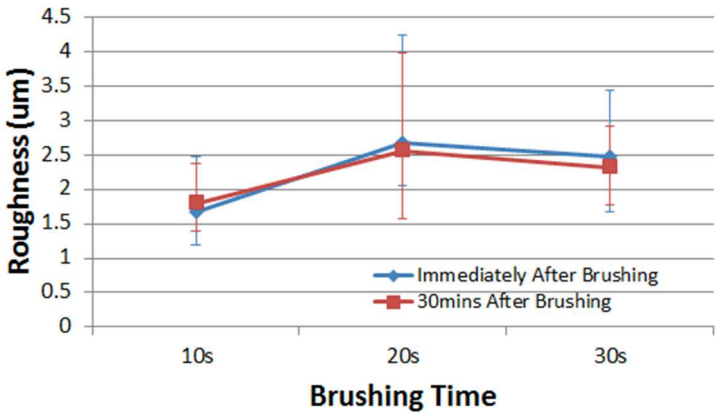

- Al sheet metal strips were brushed by 10s, 20s and 30s. The roughness of each brushed sheet was measured **immediately** after brushing.
- Roughness increases with brushing time before 20s. After 20s brushing, the roughness does not significant change in roughness.
    - ➔ In our roll bonding experiment, the brushing time for each test was between 20s and 30s. The results give us the confidence that the influences of brushing on bond formation and produced bonding strength is less significant than that of the Joule heating effect.

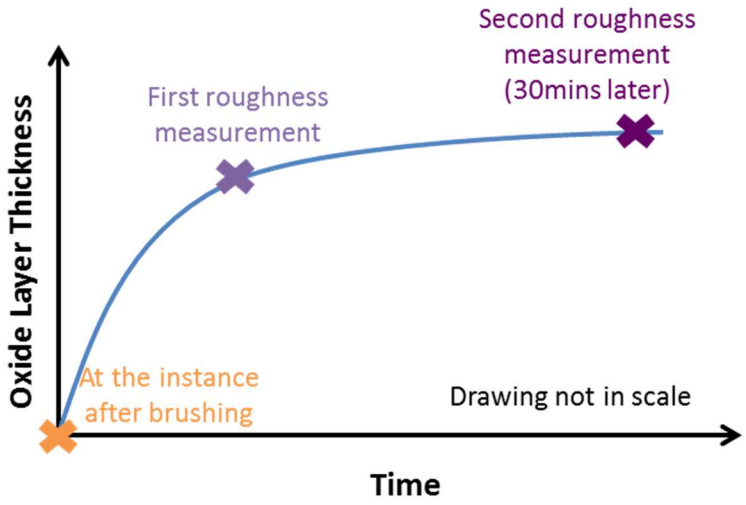

- The brushed samples were leaving in room temperature for oxide build-up for 30 mins. Their roughness were re-measured. The measurement points were random and were not necessarily the exact locations of the points measured in the first measurement, i.e. “immediately after brushing” cases.
- The roughness did change from the first measurement after 30 mins for oxide build-up. Because oxide formation on the brushed Al sheet is rapid, oxide layers were expected on the brushed sheet before roll bonding process. This shows that oxide layer were

completed form before first measurement, so that no further oxide form after the measurement.

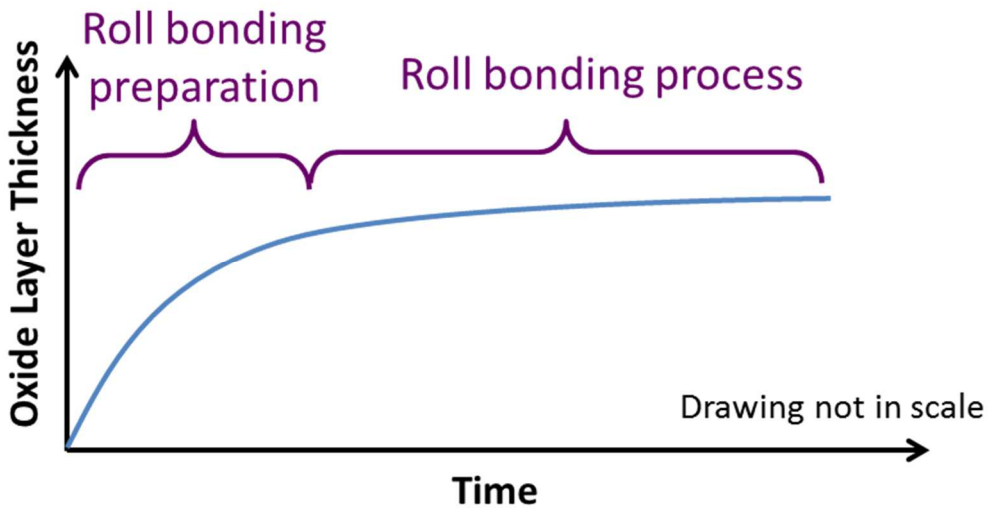

- Oxide layers were expected on the brushed Al sheet before roll bonding process because oxides are formed immediately when fresh Al exposure to air.
- After brushing and before roll bonding process, preparation was needed, such as brushed sheets alignment and clipping with stainless steel clip. The time consumed in the preparation was long enough for the oxide forms on the brushed sheets.
- The oxide layer is considered as the brittle cover layer. This cover layer can be broken if compression force is large enough and virgin metal can be extruded from it and forms metallic bonds.
- Although oxide layer still formed on the brushed sheets that it cannot be removed completely, brushing can reduce the thickness of oxide layer as well as generate brittle micro cracks for bonding.

APPENDIX IV: Roll Diameter Variation from the Designated Diameter

Rolls were installed to the desktop microrolling machine during the measurement.

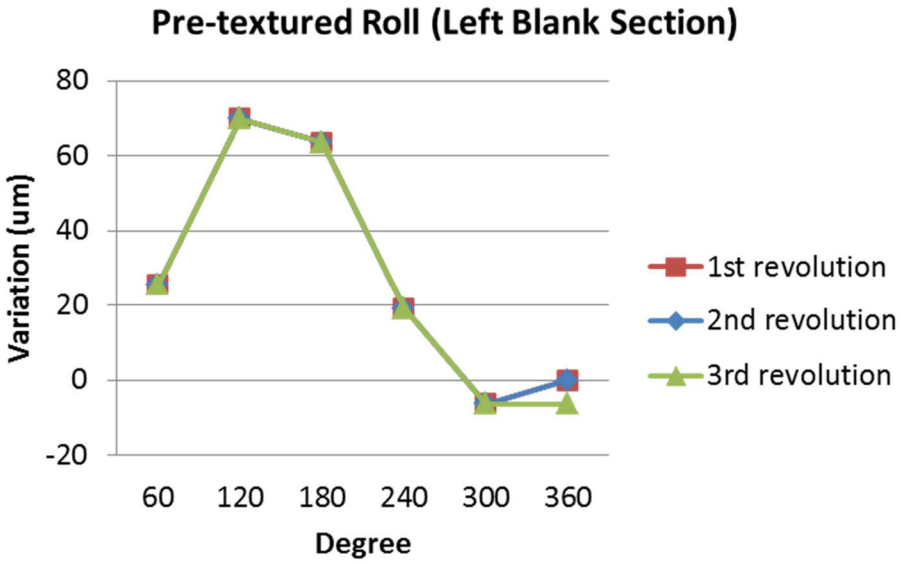

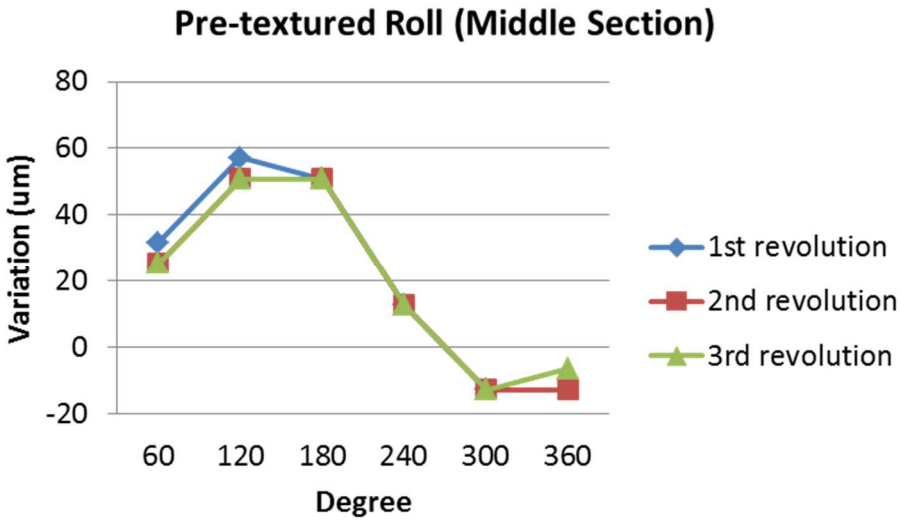

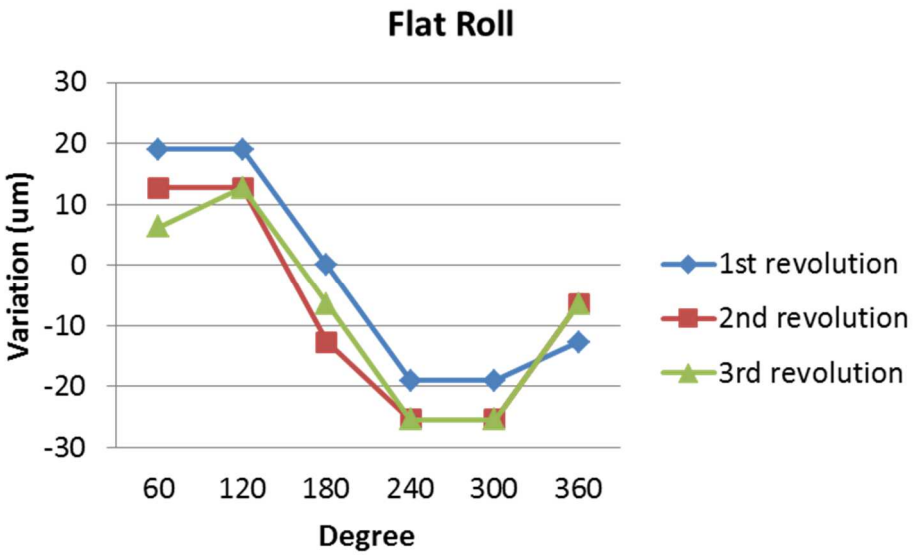
Flat Roll
30
20
10
0
-10
-20
-30
Variation (um)
60
120
180
240
300
360
Degree
1st revolution
2nd revolution
3rd revolution

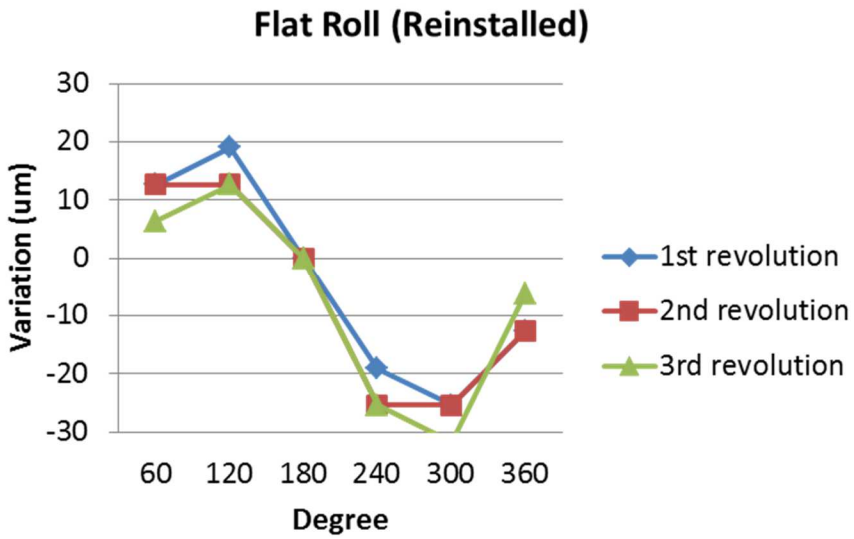
Flat Roll (Reinstalled)
30
20
10
0
-10
-20
-30
Variation (um)
60
120
180
240
300
360
Degree
1st revolution
2nd revolution
3rd revolution